The Dissertation Committee for Chih-Sung Chuu

certifies that this is the approved version of the following dissertation:

Direct Study of Quantum Statistics in a Degenerate Bose Gas

Committee:

Mark G. Raizen, Supervisor

Irene Gamba

Daniel J. Heinzen

Allan H. MacDonald

Qian Niu

Direct Study of Quantum Statistics in a Degenerate Bose Gas

by

Chih-Sung Chuu, B.S.

Dissertation

Presented to the Faculty of the Graduate School of

The University of Texas at Austin

in Partial Fulfillment

of the Requirements

for the Degree of

Doctor of Philosophy

The University of Texas at Austin

December 2006

To my parents, Der-San Chuu and Li-Chu Lee,
and my brothers, Chih-Pin and Chih-Piao,
for their endless love and support.

Acknowledgments

The first person I would like to acknowledge is my supervisor, Mark Raizen. He gave me the opportunity to join his research group and explore interesting physics by experimental means. Mark is always full of ideas and vitality.

For the past several years, I have worked with Windell Oskay, Jay Hanssen, Todd Meyrath, Florian Schreck, Gabriel Price, and Travis Bannerman. Windell gave me the first lab tour after I joined the group. Although he graduated few months later, what he taught me has been very useful over the years. I have learned many experimental skills from Jay and Todd, even after they left the group. It is always fun to discuss the tense relation of my own country and the neighboring nations with them. Florian joined the group as a postdoc for only two years; nevertheless, the impact he brought to the lab is impressive. I have also learned many useful experimental skills and physics insight from him. Gabriel and Travis joined the group in the fall of 2004 and 2006, successively. Both of them are smart guys. They are bringing the experiment to the next generation. In particular, I would like to thank Travis for proofreading this dissertation while he was busy working on the experiment and his homework.

There are many people who have provided useful helps on the experiments, too. They are my labmates, Braulio Guttierez, Kevin Henderson, Hrishikesh Kelkar, Tongcang Li, Ed Narevicius, Artem Dudarev, and Chuanwei Zhang, all members of the machine shop and cryo lab, and the administrative support staff of the CNLD,

Olga Vera, Elena Simmons, and Rosie Tovar, who left the center a few years ago. I would also like to thank other lab mates, Adam Libson, Max Riedel, Kirsten Viering, Christian Parthey, Isaac Chavez, and David Medellin, for making our lab to be a friendly environment.

In the past few years, I also met some people who have become my best friends and brought joys to my everyday life. Among them are Jung-Jung Su, Sunghwan Jung, and professor Ming-Che Chang.

Finally, I would definitely like to thank my parents, Der-San Chuu and Li-Chu Lee, and my brothers, Chih-Pin and Chih-Piao. They always share their experience with me and give me useful suggestions in my life. Without them I will never go this far.

Chih-Sung Chuu

The University of Texas at Austin

December 2006

Direct Study of Quantum Statistics in a Degenerate Bose Gas

Publication No. _____

Chih-Sung Chuu, Ph.D.
The University of Texas at Austin, 2006

Supervisor: Mark G. Raizen

This dissertation describes the experimental setup for obtaining low dimensional Bose-Einstein condensate in a single optical box trap. This novel optical trap type can provide strong confinement in two directions comparable to that which is possible in an optical lattice, but allows single-site control and addressibility. The trap consists of a crossed pair of elongated Hermite-Gaussian TEM_{01} mode beams supplemented by Gaussian beam end-caps producing a "particle-in-a-box" type geometry. Single atom detection with nearly unit quantum efficiency has been demonstrated and is fully integrated with the new trap.

Using this system, we have directly observed sub-Poissonian atom number

statistics for a degenerate Bose gas with numbers as small as 20 atoms. The observed reduction of number fluctuations is nearly a factor of two below the Poissonian (shot noise) limit. Current limit to Fock state creation for even smaller atom number is also discussed.

Contents

Acknowledgments **v**

Abstract **vii**

List of Tables **xii**

List of Figures **xiii**

Chapter 1 Introduction **1**

1.1 Quantum Degenerate Bose Gas 1

1.1.1 Non-Interacting Bose Gas 2

1.1.2 The Effect of Interaction 5

1.1.3 Gross-Pitaevskii Equation 6

1.1.4 Thomas-Fermi Approximation 7

1.2 Detection of Atoms 8

1.2.1 Absorption Imaging 9

1.2.2 Fluorescence Detection 11

1.3 Coherent Manipulation of Atoms 12

1.3.1 Magnetic Trapping 12

1.3.2 Optical Trapping 14

Chapter 2 Experimental Apparatus **17**

2.1 Vacuum Chamber 17

2.1.1 Upper Vacuum Chamber 19

2.1.2 Middle Vacuum Chamber 22

2.1.3 Lower Vacuum Chamber 24

2.2 Near Resonant Lasers 26

2.2.1 The Repump Laser 26

2.2.2 The MOT Master Laser 32

2.2.3 The Slave Lasers 35

2.3 The Magnetic Trap 35

2.4 The Optical Trap 39

2.5 Single Atom Detection 39

Chapter 3 Low-Dimensional Bose-Einstein Condensate **46**

3.1 Criterion for Low-Dimensional BEC 46

3.2 Why Low-Dimensional? 49

3.3 Experiment 50

3.3.1 Decompressed Quadrupole-Ioffe-Configuration Trap 50

3.3.2 BEC in a Gravito-Optical Trap 52

3.3.3 Resemble TEM_{01} Beam by Phase Mask 58

3.3.4 Observation of Two-Dimensional Bose-Einstein Condensate . 62

3.3.5 Observation of One-Dimensional Bose-Einstein Condensate . 64

Chapter 4 Sub-Poissonian Number Statistics in a Degenerate Bose Gas **70**

4.1 Number Squeezed State 70

4.2 The Idea of Creating a Number Squeezed State 72
4.3 A Simple Theoretical Model 75
4.3.1 Large Atom Number Limit 79
4.3.2 Small Atom Number Limit 80
4.3.3 Excitations 82
4.4 Number Fluctuation in a Degenerate Bose Gas 85
4.5 Experiment 86
4.5.1 BEC in an Ultra-stable Optical Box Trap 86
4.5.2 Atom Counting 95
4.5.3 Experimental Result 101
4.5.4 New Progress and Outlook 108

Bibliography **111**

Vita **121**

List of Tables

3.1 Maximum atom numbers in one and two-dimensional BECs. 49

4.1 Beam parameters of 3D optical box trap. 89

4.2 Measured noise and corresponding number fluctuation. 95

List of Figures

2.1 Vacuum chamber. 18

2.2 Upper vacuum chamber. 20

2.3 Middle vacuum chamber. 23

2.4 Lower vacuum chamber. 25

2.5 Different frequencies of near resonant lasers used in the experiment. 27

2.6 Littrow-configured grating-stabilized diode laser system. 28

2.7 Beam distribution and layout of saturated absorption spectroscopy for the repump laser. 30

2.8 Saturated absorption spectrum for the Rb^{87} D_2 line $F = 1 \rightarrow F'$ hyperfine manifold. 31

2.9 Beam distribution and layout of saturated absorption spectroscopy for the MOT master laser. 33

2.10 Saturated absorption spectrum for the ^{87}Rb D_2 line $F = 2 \rightarrow F'$ hyperfine manifold. 34

2.11 The slave laser. 36

2.12 Quadrupole-Ioffe-configuration (QUIC) trap. 38

2.13 Layout of the optics producing the optical traps. 40

2.14 Single atom detection system. 42

2.15 Single atom in the MOT. 44

3.1 Decompressed Quadrupole-Ioffe-Configuration trap. 53
3.2 Compressed optical trap. 55
3.3 Bose-Einstein condensate in the grvito-optical trap. 57
3.4 Bose-Einstein condensate in a square hard-wall trap. 59
3.5 Different methods of producing two-dimensional Bose-Einstein condensates. 61
3.6 Manufacture and property of TEM_{01} phase mask. 63
3.7 Observation of two-dimensional Bose-Einstein condensate in a TEM_{01} optical trap. 65
3.8 Observation of one-dimensional Bose-Einstein condensate in a crossed TEM_{01} optical trap. 67
3.9 Expansion of one-dimensional Bose-Einstein condensate in a TEM_{01} sheet. 69

4.1 Assuming the length of a wire is fixed, what would be the number of birds on this wire? 73
4.2 Illustration of controlling the volume of water in a bowl. 74
4.3 Experimental sequence of preparing sub-Poissonian number statistics in a degenerate Bose gas. 76
4.4 Variational parameters, κ_1 and κ_2, that minimize the total energy of three atoms in a well for different well depths V_0. 78
4.5 Bound states for 1, 2, and 3 atoms in a well found by diagonalizing the Hamiltonian in the limit of small atom number. 81
4.6 Different potential-parameter regimes that have bound states for 1, 2, 3, 4, and $N \geq 5$ atoms. 83

4.7 Pictorial of the optical trap. 87
4.8 Potential plots of the optical trap. 90
4.9 Intensity feedback loop for the ultra-stable optical box trap. 92
4.10 Temperature-stabilized voltage controlled oscillators. 93
4.11 Capture efficiency for different MOT intensities. 96
4.12 Calibration of atom number measured by fluorescence imaging. . . . 99
4.13 Step-wise signal of the avalanche photodiode (APD). 100
4.14 Calibration of atom number between two MOT settings. 102
4.15 Cleaning processes prior to the detection. 103
4.16 Dependence of atom number on the trap depth. 104
4.17 Observation of sub-Poissonian number statistics. 106
4.18 Number statistics for mean atom number $N = 60$. 107
4.19 Dependence of atom number fluctuations on the adiabaticity. 109
4.20 Dependence of atom number on the trap depth. 110
4.21 Number statistics for mean atom number $N = 21$ and $N = 28$. . . . 112

Chapter 1

Introduction

This chapter summarizes some basis concepts relevant to the experiments described in this dissertation.

1.1 Quantum Degenerate Bose Gas

All particles in nature belong to one of two types: boson or fermion. The total spin of a boson is a multiple integer of $\hbar$, while a fermion has spin of multiple odd integer of $\hbar/2$. For neutral atoms, since the number of electrons and protons is equal, atoms with an even number of neutrons are bosons while atoms with an odd number of neutrons are fermions. In our experiments, we use ^{87}Rb (rubidium), which has 37 protons and 50 neutrons and thus is a boson. Therefore, some properties of bosons will be discussed in this section.

1.1.1 Non-Interacting Bose Gas

For a non-interacting Bose gas, the mean occupation number of the single-particle state with energy E obeys the Bose distribution function [1],

$$f(E) = \frac{1}{e^{-(E-\mu)/k_B T} - 1}, \tag{1.1}$$

where μ is the chemical potential, k_B is the Boltzmann constant, and T is the temperature of the system. The chemical potential can be determined from the condition that the total atom number N is equal to the sum of all occupancies,

$$N = \frac{1}{\hbar^3} \int \mathrm{d}r^3 \mathrm{d}p^3 f(E), \tag{1.2}$$

where r and p refer to the position and momentum, respectively, and $\hbar$ is the Plank's constant. Moreover, as can be seen from Eq. (1.1), the mean occupation number is always smaller than $1/\exp[(E - E_{min})/k_B T] - 1$ with E_{min} being the energy of the ground state; otherwise, the mean occupation number of the ground state would be negative and therefore unphysical.

At high temperature, since the mean occupation number of each state is very small, the chemical potential is much less than the energy of the ground state E_{min}. The mean occupation number is approximated by the Boltzmann distribution function,

$$f(E) \sim e^{-E/k_B T}. \tag{1.3}$$

The statistics of an ideal Bose gas thus resembles that of an ideal Boltzmann gas [1], a non-physical system but a useful model.

For atoms trapped in a cylindrically symmetric potential, the energy can be

written as

$$E = \frac{p^2}{2m} + \frac{m\omega_{rad}^2}{2}(x^2 + y^2 + \epsilon^2 z^2), \tag{1.4}$$

with $\epsilon = \omega_{ax}/\omega_{rad}$ being the aspect ratio, ω_{rad} and ω_{ax} the trapping frequencies in the radial and axial directions, respectively, and m the atomic mass. Substituting Eq. (1.4) into Eq. (1.3) yields

$$f(E) = \frac{\hbar^3 N\lambda}{(2\pi\sigma_{rad}\sigma_p)^3} \exp\left(-\frac{p^2}{2\sigma_p^2}\right) \exp\left(-\frac{x^2}{2\sigma_{rad}^2} - \frac{y^2}{2\sigma_{rad}^2} - \frac{z^2}{2\sigma_{ax}^2}\right), \tag{1.5}$$

where $\sigma_i = (k_B T/m\omega_i^2)^{1/2}$ is the width of the spatial distribution of the atoms in the i direction, and $\sigma_p = (mk_B T)^{1/2}$ is the width of the momentum distribution of the atoms. Therefore, both of the distributions are Gaussian. Furthermore, the momentum distribution is isotropic but the spatial distribution is anisotropic as the result of the trap shape.

Bose-Einstein condensation appears when the occupation in the ground state becomes macroscopic. The highest temperature for this to be true is defined as the transition temperature T_c. It can be calculated by assigning all of the atoms to be in the excited states [2], $N = N_{ext}(\mu = 0)$, in the limit of large N. For a Bose gas in a three-dimensional harmonic-potential, the result is

$$T_c = \frac{\hbar\bar{\omega}N^{1/3}}{k_B\zeta(3)}, \tag{1.6}$$

where $\zeta(\alpha) = \sum_{n=1}^{\infty} n^{-\alpha}$ is the Riemann zeta function ($\zeta(3) = 1.202$) and

$$\bar{\omega} = (\omega_x\omega_y\omega_z)^{1/3} \tag{1.7}$$

is the geometric mean of the trapping frequencies, ω_x, ω_y, and ω_z. For a trapping

potential with cylindrical symmetry $\omega_{ax} = \epsilon\omega_{rad}$, T_c is proportional to $\epsilon^{1/3}$; therefore, with the same geometric trapping frequency $\bar{\omega}$, an anisotropic trap ($\epsilon \neq 1$) will have a higher transition temperature than an isotropic trap.

In the case of a three-dimensional box potential with volume V, we have

$$T_c = \frac{2\pi\hbar^2}{m}\left(\frac{n}{\zeta(3/2)}\right)^{2/3}. \tag{1.8}$$

where $n = N/V$ is the density and $\zeta(3/2) = 2.612$. Rearranging above equation, we obtain the criterion for Bose-Einstein condensation,

$$n\left(\frac{h^2}{2\pi m k_B T_c}\right)^{3/2} = 2.612, \tag{1.9}$$

which states that the distance between individual atoms $n^{-1/3}$ is comparable to their de Broglie wavelength $\lambda_{dB} = h/\sqrt{2\pi m k_B T}$ at the transition temperature T_c. The quantity $\rho = n\lambda_{dB}^3$ is also known to be the phase space density, which corresponds to the number of atoms in a volume equal to the cube of the de Broglie wavelength. Sometimes, the criterion for Bose-Einstein condensation is written as $n_0\lambda_{dB} = 2.612$, where n_0 is the peak atomic density at the center of the trap.

With the expression for T_c, the condensate fraction $N_0/N = 1 - N_{ex}(T_c,\, \mu = 0)/N$ can be calculated as a function of the temperature, which is

$$N_0/N = 1 - \left(\frac{T}{T_c}\right)^3. \tag{1.10}$$

For finite atom number, the correction reduces the condensate fraction [3] to

$$N_0/N \;=\; 1 - \left(\frac{T}{T_c}\right)^3 - \frac{3\omega_m\zeta(2)}{2\bar{\omega}\zeta(3)^{2/3}}\left(\frac{T}{T_c}\right)^2 N^{-1/3} \tag{1.11}$$

$$\cong \quad 1 - \left(\frac{T}{T_c}\right)^3 - 2.2\frac{\omega_m}{\bar{\omega}}\left(\frac{T}{T_c}\right)^2 N^{-1/3}, \tag{1.12}$$

where $\omega_m = (\omega_x + \omega_x + \omega_z)/3$ is the arithmetic average of the trapping frequencies.

The finite size effect also reduces the transition temperature by

$$\delta T_c/T_c = -0.73\frac{\omega_m}{\bar{\omega}}\left(\frac{T}{T_c}\right)^2 N^{-1/3}, \tag{1.13}$$

which can be seen by setting $N_0 = 0$ in Eq. (1.11) and taking the derivative of it.

1.1.2 The Effect of Interaction

In principle, the effect of interaction can be studied by solving exactly the full many-body Schrödinger equation. However, when the system is too large, the numerical calculation becomes impractical. Fortunately, the mean-field approach provides a way to simplify this problem. The basic idea of the approach is to decouple the condensate contribution from the bosonic field operator [3] by noticing that, in the thermodynamic limit ($N \to \infty$), the bosonic field operators can be treated like complex numbers.

The situation is further simplified when the system is consist of dilute and cold atoms, since at low temperature (energy) only the two-body collisions are relevant. Therefore, one can use an effective interaction

$$V(\mathbf{r}' - \mathbf{r}) = g\delta(\mathbf{r}' - \mathbf{r}), \tag{1.14}$$

where the coupling constant g is only related to the scattering length a_s via

$$g = \frac{4\pi\hbar^2 a_s}{m} \tag{1.15}$$

and independent of the exact shape of the two-body potential.

As a consequence of the mean-field interaction, the ground state in a harmonic potential no longer has the shape of a Gaussian. The atoms are pushed outwards and the central density is flattened. Moreover, interaction plays an important role in the ballistic expansion of a BEC initially trapped in an anisotropic potential. It can be shown that [4], as $\epsilon = \omega_{ax}/\omega_{rad} \ll 1$, the time evolution of the atomic cloud's size follows

$$R_{rad}(\tau) = R_{rad}(0)\sqrt{1+\tau^2}, \tag{1.16}$$

$$R_{ax}(\tau) = R_{ax}(0)[1+\epsilon^2(\tau\tan^{-1}\tau - \ln\sqrt{1+\tau^2}) + O(\epsilon^4)], \tag{1.17}$$

where R_{rad} and R_{ax} are the sizes of the atomic cloud in the radial and axial directions, respectively, and $\tau = \omega_{rad}t$. Since $\epsilon \ll 1$, R_{rad} expands much faster than R_{ax}. As the result, a horizontally elliptic BEC will eventually convert to a vertically elliptic shape, a signature of the existence of a BEC.

1.1.3 Gross-Pitaevskii Equation

Using the mean-field approach with the effective interaction given in Eq. (1.14), the Heisenberg equation then reads

$$i\hbar\frac{\partial}{\partial t}\Phi(\mathbf{r},\, t) = \left(-\frac{\hbar^2\nabla^2}{2m} + V_{ext}(\mathbf{r}) + g\,|\Phi(\mathbf{r},\, t)|^2\right)\,\Phi(\mathbf{r},\, t), \tag{1.18}$$

which is known as the Gross-Pitaevskii (GP) Equation. At thermal equilibrium, one can write $\Phi(\mathbf{r},\, t) = \phi(\mathbf{r})\exp^{-i\mu t/\hbar}$, and the GP equation becomes a nonlinear

Schrödinger equation,

$$\left(-\frac{\hbar^2\nabla^2}{2m} + V_{ext}(\mathbf{r}) + g\phi(\mathbf{r})^2\right)\phi(\mathbf{r}) = \mu\phi(\mathbf{r}), \tag{1.19}$$

where the nonlinearity comes from the effective interaction. Note that the GP equation is valid (1) in the limit of a dilute gas, i.e. the s-wave scattering length is much smaller than the interatomic separation, and (2) when the atom number is much greater than 1.

1.1.4 Thomas-Fermi Approximation

In a repulsively interacting gas, if the interaction energy E_{int} ($\propto gNn \propto N^2 a_s/a_{ho}$ with a_{ho} being the harmonic oscillator length of the ground state $(\hbar/m\omega_{ho})^{1/2}$) is much larger than the kinetic energy of each particle E_{kin} ($s \propto N\hbar\omega_{ho} \propto Na_{ho}^{-2}$),

$$\frac{E_{int}}{E_{kin}} \propto \frac{Na_s}{a_{ho}} \gg 1, \tag{1.20}$$

one can neglect the kinetic energy term in Eq. (1.19) and obtain the density profile of the atomic cloud,

$$n(\mathbf{r}) = |\phi(\mathbf{r})|^2 = g^{-1}(\mu - V_{ext}(\mathbf{r})), \quad \mu > V_{ext}(\mathbf{r}), \tag{1.21}$$

and $n(\mathbf{r}) = 0$ for $\mu < V_{ext}(\mathbf{r})$. Therefore, in a harmonic potential $V_{ext}(\mathbf{r}) = (m/2)(\omega_x^2 x^2 + \omega_y^2 y^2 + \omega_z^2 z^2)$, the density distribution is an inverted parabola,

$$n(\mathbf{r}) = \frac{\mu}{g}\left(1 - \frac{x^2}{R_{TF,x}^2} - \frac{y^2}{R_{TF,y}^2} - \frac{z^2}{R_{TF,z}^2}\right), \tag{1.22}$$

where

$$R_{TF,i} = \sqrt{\frac{2\mu}{m\omega_i^2}} \tag{1.23}$$

is the Thomas-Fermi radius in the i direction.

The chemical potential μ can be found from the normalization condition,

$$N = \int \mathrm{d}\mathbf{r}\, |\phi(\mathbf{r})|^2 . \tag{1.24}$$

For a harmonic potential, the result is

$$\mu = \frac{\hbar\bar{\omega}}{2}\left(\frac{15Na_s}{\bar{a}}\right)^{2/5}, \tag{1.25}$$

where $\bar{a} = (\hbar/m\bar{\omega})^{1/2}$ is the harmonic oscillator length defined by the geometric mean of the trapping frequencies.

1.2 Detection of Atoms

Two detection schemes have been used in our experiments: absorption imaging and fluorescence detection. Absorption imaging has the advantage of showing the spatial information but has a poor resolution when the atom number is small. To compensate for this, fluorescence detection is used for small atom number. However, since the fluorescence detection is accomplished inside a magnetic trap, the spatial information is lost. This section describes the basic idea behind the two detection schemes.

1.2.1 Absorption Imaging

When a laser beam travels through a sample of atoms, the light is scattered by the atoms and thus intensity loss results. The scattered intensity per length in the direction of beam propagation is given by $\mathrm{d}I/\mathrm{d}z = -\hbar\omega R_{sc} n(\mathbf{r})$, where ω is the laser frequency multiplied by 2π and $n(\mathbf{r})$ is the density distribution of the atoms. R_{sc} is the total scattering rate of light from the laser field [5]:

$$R_{sc} = \left(\frac{\Gamma}{2}\right) \frac{I/I_{sat}}{1 + 4(\Delta/\Gamma)^2 + I/I_{sat}}, \tag{1.26}$$

where Δ is the detuning of the laser field from the atomic resonance, Γ is the natural line width (or the decay rate of the excited state) of the atoms, and I_{sat} is the saturation intensity given by

$$I_{sat} = \frac{\hbar\omega^3\Gamma}{12\pi c^2}. \tag{1.27}$$

For low light intensity ($I/I_{sat} \ll 1$), the absorption rate is then given by

$$\frac{\mathrm{d}I}{\mathrm{d}z} = -\sigma n(\mathbf{r}) I, \tag{1.28}$$

where σ is the scattering cross section,

$$\sigma = \frac{\sigma_0}{1 + 4(\Delta/\Gamma)^2} \tag{1.29}$$

with $\sigma_0 = 3\lambda^2/2\pi$ being the on-resonance scattering cross section. Eq. (1.28) is also known as Beer's law. In practice, if the atoms are not in the state resonant with the laser, one should instead use $\sigma' = C^2\sigma$, with C being the Clebsch Gordon coefficient, to account for the fact that some atoms might be pumped to a non-detectable state.

By integrating Eq. (1.28), the beam intensity after passing through the cloud of atoms can be found to be

$$I = I_0 \exp\left(-\int \sigma n(\mathbf{r}) \mathrm{d}z\right), \tag{1.30}$$

where I_0 is the incident beam intensity. Therefore, measuring the beam intensities before (I_0) and after (I) passing through the cloud (or traveling through no atoms (I_0) and atoms (I)) yields the optical density,

$$D_{opt}(x, y) = -\ln\left(\frac{I}{I_0}\right) = \sigma \int n(\mathbf{r}) \mathrm{d}z, \tag{1.31}$$

which is proportional to the integrated atomic density. Furthermore, the atom number can be obtained by integrating the optical density,

$$N = \sigma^{-1} \int\int D_{opt}(x, y) \mathrm{d}x \mathrm{d}y. \tag{1.32}$$

By analyzing the density distribution, one can obtain information more than the spatial distribution of the atoms. Consider a weakly interacting cloud of atoms, at temperature $T \gg T_c$, trapped in a harmonic potential. The initial density distribution can be found by integrating the Boltzmann distribution function in the whole momentum space, which gives

$$n(\mathbf{r}) = \frac{N}{\sigma_r(0)^3 (2\pi)^{3/2}} \exp\left(-\frac{\mathbf{r}^2}{2\sigma_r(0)^2}\right), \tag{1.33}$$

where $\sigma_r(0)$ is the width of the density distribution at $t = 0$. Then, the atoms are suddenly released from the trap and expand ballistically - a process called time-of-flight (TOF). Since the time evolution of a Gaussian is a Gaussian with the

convolution between the spatial and momentum space, the density distribution at a later time t is given by

$$n(\mathbf{r}) = \frac{N}{\sigma_r(t)^3(2\pi)^{3/2}}\exp\left(-\frac{\mathbf{r}^2}{2\sigma_r(t)^2}\right), \tag{1.34}$$

with

$$\sigma_r(t)^2 = \sigma_r(0)^2 + \frac{\sigma_p(0)^2}{m^2}t^2, \tag{1.35}$$

where $\sigma_p(0) = (mk_BT)^{1/2}$ is the width of the momentum distribution at $t = 0$ similar to the case in Eq. (1.5). Therefore, one can measure the time evolution of $\sigma_r(t)$ and obtain the temperature of the atomic cloud by fitting it with Eq. (1.35).

For a long TOF in which the size of the atomic cloud is much larger than the size at $t = 0$, the density distribution (Eq. (1.34)) resembles the momentum distribution at $t = 0$, that is,

$$n(\mathbf{r},\, t \to \infty) = n(\mathbf{p},\, t = 0) \propto \exp\left(-\frac{\mathbf{p}^2}{2\sigma_p(0)^2}\right), \tag{1.36}$$

where $\mathbf{p} = m\mathbf{r}/t$. Therefore, by measuring the width of the density distribution $\tilde{\sigma_r}$ of the atoms in a long TOF, the temperature of the atomic cloud can be obtained via

$$T = \frac{m\tilde{\sigma_r}^2}{k_Bt^2}. \tag{1.37}$$

1.2.2 Fluorescence Detection

Fluorescence detection is essentially equivalent to absorption imaging. In absorption imaging, one detects the photons being absorbed; in fluorescence detection, one detects the photons being re-emitted - or scattered. Therefore, in both methods, the same photons are being measured. However, the direction of the scattering

is random in nature, therefore the signal of the fluorescence detection is usually a factor of 100 smaller [6]. Nevertheless, since fluorescence detection is not strongly dependent on the intensity profile of the beam, it is less influenced by the fluctuation of the beam intensity.

1.3 Coherent Manipulation of Atoms

Atoms can be manipulated in a manner analogous to light. In order to preserve the coherence of the atoms during the manipulation, one can use either magnetic fields or far-detuned laser light. In this section, the principles of magnetic and optical trapping are introduced.

1.3.1 Magnetic Trapping

The magnetic force felt by an atom in a magnetic field arises from the interaction of its magnetic dipole moment with the external magnetic field strength, known as the Zeeman effect in which the energy of the atoms is dependent on the spatial variation of the magnetic field. At low magnetic field, the potential is given by

$$U_B = m_F g_F \mu_B B(\mathbf{r}), \tag{1.38}$$

where $m_F = -F \cdots F$ is the quantum number of the Zeeman sublevels, F refers to the quantum number of the hyperfine energy levels, g_F is the Landé factor, $\mu_B = h \cdot 1.4$ MHz/G is the Bohr magneton with h being the Planck's constant, and $B(\mathbf{r})$ is the magnetic field. Therefore, in order to create a trap for atoms U_B needs to have a minimum, which means $m_F g_F > 0$. For the ground states of a ^{87}Rb atom, this condition is only fulfilled for the states $(F, m_F) = (1, -1), (2, 1), (2, 2)$.

Among these states, the (2, 2) state feels the strongest confinement for the same magnetic field.

The magnetic trap used in our experiments is the quadrupole Ioffe configuration (QUIC) trap [7], which has three coils arranged in a shape of "U" with two quadrupole coils on the sides and Ioffe coil at the middle. When only the two quadrupole coils are used, it produces a magnetic field with a zero at the center,

$$\mathbf{B}(x,\, y,\, z) = \frac{B^{'}}{2}(x\mathbf{x} + y\mathbf{y} + 2z\mathbf{z}), \tag{1.39}$$

where $B^{'}$ is the gradient of the magnetic field in the axial direction of the pair, with the potential given by

$$U_B(\mathbf{r}) = \frac{1}{2} m_F g_F \mu_B B^{'} \sqrt{x^2 + y^2 + 4z^2}. \tag{1.40}$$

The direction of the magnetic field therefore changes rapidly near the center where $\mathbf{B}(0) = 0$. As a result, atoms moving across zero magnetic field might not be able to follow the change of $\mathbf{B}(\mathbf{r})$ adiabatically and become untrapped because of the change of the sign of U_B. This is known as Majorana spin flips.

The purpose of the Ioffe coil is to add an offset to the magnetic field. The magnetic field with the addition of the Ioffe coil is given by

$$\begin{aligned} \mathbf{B}(x,y,z) &= (B^{'}x - C_{ax}xz)\mathbf{x} && (1.41)\\ &- (B^{'}y + C_{ax}yz)\mathbf{y} && (1.42)\\ &+ \left[B_0 + \frac{1}{2}C_{ax}\left(z^2 - \frac{x^2+y^2}{2}\right)\right]\mathbf{z}, && (1.43) \end{aligned}$$

where B_0 is the magnetic field offset and C_{ax} is the curvature of the magnetic field

along the axis of the two quadrupole coils. The magnitude of the field near the center is

$$B(\mathbf{r}) \cong B_0 + \frac{1}{2}C_{rad}(x^2 + y^2) + \frac{1}{2}C_{ax}z^2, \tag{1.44}$$

where C_{rad} is the curvature of the magnetic field in the radial direction, given by

$$C_{rad} = \frac{B'^2}{B_0} - \frac{C_{ax}}{2}. \tag{1.45}$$

In typical operation, $C_{rad} \cong B'^2/B_0$ and the potential experienced by the atoms is then

$$U_B(\mathbf{r}) = m_F g_F \mu_B B_0 + \frac{m}{2}(\omega_z^2 z^2 + \omega_\rho^2 \rho^2), \tag{1.46}$$

where m is the atomic mass, $\rho^2 = x^2 + y^2$, and ω_i is the trapping frequency in the i direction given by

$$\omega_z = \left(\frac{m_F g_F \mu_B C_{ax}}{m}\right)^{1/2}, \tag{1.47}$$

$$\omega_\rho = \left(\frac{m_F g_F \mu_B B'^2}{m B_0}\right)^{1/2}. \tag{1.48}$$

1.3.2 Optical Trapping

Atoms do not have permanent electric dipole moments; however, atoms can interact with a light field through the induced dipole moment. A common case is an atom sitting in a laser field which has an oscillating electric field.

Consider a linearly polarized, focused laser beam with a Gaussian intensity profile,

$$I(\mathbf{r}) = I_0 \frac{\exp\left[-2r^2/w(z)^2\right]}{1 + (z/z_R)^2}, \tag{1.49}$$

where $I_0 = 2P/\pi w_0^2$ is the peak intensity with P being the laser power and w_0 the

$1/e^2$ radius of the beam at the focus, and $w(z) = w_0\sqrt{1+(z/z_R)^2}$ is the $1/e^2$ radius of the beam along the direction of the beam propagation with $z_R = w_0^2\pi/\lambda$ being the beam's Rayleigh length and λ the wavelength of the laser. For alkali atoms, the trapping potential resulting from this laser beam is then given by [8]

$$U(\mathbf{r}) = \frac{\pi c^2 \Gamma}{2\omega_0^3}\left(\frac{2}{\Delta_{2,F}} + \frac{1}{\Delta_{1,F}}\right) I(\mathbf{r}) \tag{1.50}$$

$$= U_0 \frac{\exp\left[-2r^2/w(z)^2\right]}{1+(z/z_R)^2}, \tag{1.51}$$

where c is the speed of sound, Γ is the natural line width, ω_0 is the atomic transition frequency, and U_0 is the trap depth. $\Delta_{1,F}$ and $\Delta_{2,F}$ are the laser detunings corresponding to the D_1 and D_2 lines, respectively. For a blue-detuned laser ($\Delta_{1,F}$, $\Delta_{2,F} > 0$), the resulting potential is thus repulsive and pushes the atoms away from the focus (intensity maximum). On the other hand, a red-detuned laser ($\Delta_{1,F}$, $\Delta_{2,F} < 0$) produces an attractive potential which traps the atoms at the focus.

When the atoms are localized around the trap center, the potential can be approximated by a harmonic potential,

$$U(\mathbf{r}) = U_0\left(1 - \frac{2r^2}{w_0^2} - \frac{z^2}{z_R^2}\right). \tag{1.52}$$

The trapping frequencies are thus given by

$$\omega_{rad} = \sqrt{\frac{4U_0}{mw_0^2}}, \tag{1.53}$$

$$\omega_{ax} = \sqrt{\frac{2U_0}{mz_R^2}}, \tag{1.54}$$

where $\omega_{ax} = (\lambda/\sqrt{2}\pi w_0)\omega_{rad}$ is usually much smaller than ω_{rad} because $\lambda \ll w_0$.

It is also important to consider the rate at which the atoms absorb the light or being heated up. For detuning much larger than the hyperfine splitting as in most optical traps, the scattering rate is given by [8]

$$\Gamma_{sc}(\mathbf{r}) = \frac{\pi c^2 \Gamma^2}{2\hbar\omega_0^3}\left(\frac{2}{\Delta_{2,F}^2} + \frac{1}{\Delta_{1,F}^2}\right) I(\mathbf{r}). \tag{1.55}$$

Based on the observation that the trapping potential scales as I/Δ whereas the scattering rate scales as I/Δ^2, one can therefore use a laser of large detuning to reduce the scattering rate.

Chapter 2

Experimental Apparatus

The experiments described in this dissertation are all carried out in optical traps. Although the configurations of the traps might be different, the experimental apparatus used to create these traps is very similar. This chapter describes the experimental apparatus we use to perform these experiments.

2.1 Vacuum Chamber

The environment at room temperature can easily heat up the cooled atoms in our experiment which typically have a temperature of a few hundred nK (about nine orders of magnitude smaller than the room temperature). Therefore, one needs a ultra-high vacuum (UHV) chamber to prevent the cooled atoms from colliding with the atoms at room temperature. On the other hand, one needs a high atomic density (and thus *bad* vacuum) in order to collect a reasonable amount of atoms in a short time.

To meet these two requirements, we have a high vacuum (HV) chamber (upper chamber) at the vapor pressure of rubidium ($\sim 10^{-8}$ torr), which allows for

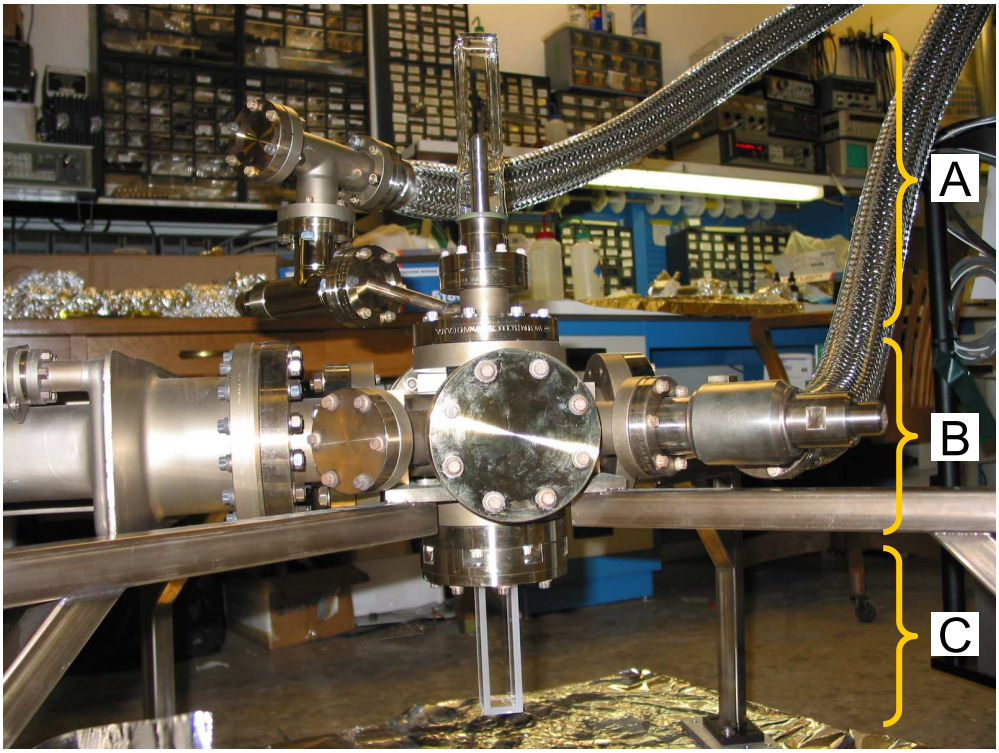

Figure 2.1: In order to have a fast loading rate of atoms and avoid collisions between cooled atoms and thermal atoms at room temperature, the vacuum chamber consists of a high vacuum chamber (A) at the vapor pressure of rubidium and a ultra-high vacuum chamber (C) with a middle chamber (B) connecting the two and serving as a pumping regime.

fast loading of atoms, and an UHV chamber (lower chamber) where we perform all the experiments. A middle chamber is connected between the upper and lower chambers to serve as a pumping region and thus maintains the pressure difference between the two chambers. Fig. 2.1 shows the main parts of our vacuum chamber.

2.1.1 Upper Vacuum Chamber

The upper chamber, as shown in Fig. 2.2, basically comprises three parts: a glass cell, a differential pumping tube, and a rubidium reservoir.

The glass cell is made by sealing a rectangular cell to a tubular adapter (shown as A in Fig. 2.2(a) and (b)). The rectangular cell has a outer dimension of 4" $\times$ 1.25" $\times$ 1.25" with a thickness of 1/4" and is made of Pyrex without anti-reflection coating. Pyrex is a brand name of borosilicate glass, which consists of about 70% silica, 10% boric oxide, 8% sodium oxide, and 1% calcium oxide, and has a thermal expansion coefficient about one-third that of ordinary glass. The tubular adaptor is a 304 stainless steel-to-quartz adapter with a Pyrex-to-quartz graded seal (Larson Electronic Glass, SQ-150-F2) and has a 2.75" CF type flange on one end. The sealing and the rectangular cell are all made by Technical Glass Inc.

The differential pumping tube is a 6.75" long 304 stainless steel tube with an outer diameter of 0.6" (shown as B in Fig. 2.2). The inner diameter increases in five steps from 1/8" at the top to 3/8" at the bottom (diameter-length: 0.125"-1", 0.188"-1.25", 0.25"-1.5", 0.313"-1.5", 0.375"-1.443"), which forms a maximum capture angle of $\sim 2^\circ$ defined by the sizes of the upper and lower MOTs and thus allows for an optimal loading rate of atoms. The successive steps also reduce the conductance between the upper and lower chamber (compared to a single diameter tube), and therefore maintains a pressure difference between the upper and lower

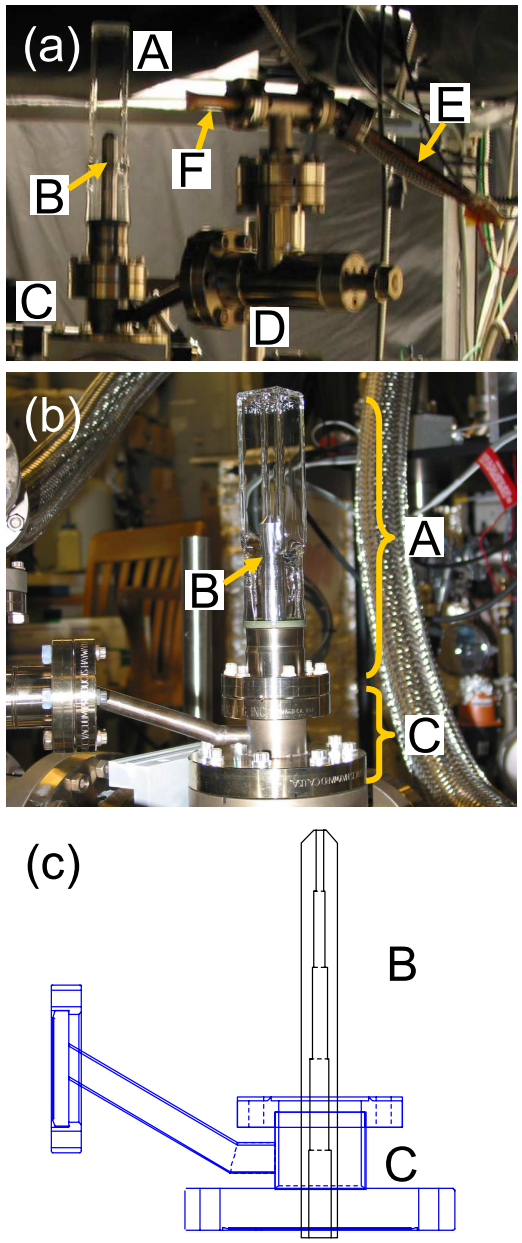

Figure 2.2: Upper vacuum chamber. (a) Different parts are labeled as glass cell (A), differential pumping tube (B), connection part (C) between the glass cell and the all-metal valve (D), rubidium reservoir (E), and pinch-off tube (F) to the roughing-turbo pump station. (b) A closer view of upper vacuum chamber. (c) Cross section of the welded parts around the differential pumping tube.

chamber by about three orders of magnitude.

The conductance is calculated to be C=52.7 mL/s under our experimental conditions (HV, rubidium, 20°) by using the conductance formula for a tube with a circular cross section in the molecular flow region [9]

$$C = 2.6 \times 10^{-4} \bar{v} \frac{D^3}{L} \ \mathrm{L\,s^{-1}}, \tag{2.1}$$

where D and L are the diameter and length measured in cm, respectively, $\bar{v} = \sqrt{8k_BT/\pi m}$ is the average molecular velocity in cm s^{-1}, k_B is Boltzmann's constant, T is the temperature in K, and m is the atomic mass in kg. Therefore, the differential pumping tube leads to a pressure difference of three orders of magnitude between the upper and lower chambers, $P_{\mathrm{upper}}/P_{\mathrm{lower}}$=$1+S_{\mathrm{P}}/C \sim 10^3$ [9], where S_{P}=75 L/s is the pumping speed of the vacuum pump in the lower chamber.

At the top of the differential pumping tube, a small 45° wedge has been lopped off to allow the laser beams used in the magneto-optical trap (MOT) to pass without being clipped. The bottom part of the tube is welded to a 4.5" rotatable blank flange (MDC, 100018) which is then welded to a rotatable 2.75" half nipple (MDC, 401028). A tortuous 1/2" tubing (MDC, 480002) is welded to the side of the nipple reducer, whose other end is welded with a 2.75" rotatable flange (MDC, 100008) to which a 2.5" all-metal valve (Nor-Cal Products Inc, AMV-1502-CF) is attached. A 1-1/3" tee is connected to the other end of the all-metal valve by a zero length 2.75"-to-1-1/3" reducer. A cross section of the parts welded around the differential pumping tube is shown schematically in Fig. 2.2 (c).

Two 1/2" copper pinch-off tubes (Huntington, CPT-133-050) with a flange size of 1-1/3" are attached on both sides of the tee. One pinch-off tube is used to connect to the roughing-turbo pump station during the vacuum chamber's bake-out

and is pinched when the chamber is disconnected from the pump station. The other pinch-off tube, being pinched in advance, acts as a rubidium reservoir in which a one-gram ampoule (Technical Glass Inc) of 99.9% rubidium metal (ESPI, purity 3N5) is stored. The ampoule can be broken by pliers from outside, which should be done before the pump station is removed from the vacuum system. The all-metal valve thus can be used to (1) regulate the pressure of rubidium atoms inside the vacuum chamber, which is continuously pumped away, and (2) seal the vacuum system from the atmosphere pressure when the rubidium ampoule needs to be replaced.

2.1.2 Middle Vacuum Chamber

The middle chamber, a ten-way cross modified from a six-way cross with 4.5" Con-Flat (CF) flanges (Fig. 2.3), acts as a pumping region to keep the ultra-high vacuum in the lower chamber. Four additional 1.5" tubes with 2.75" CF flanges are welded between the 4.5" ports in one plane around the chamber with the other two 4.5" ports used to connect with the upper and lower chambers.

A 75 L/s ion pump (Varian, 919-0103, refurbished by Duniway Stockroom) is attached to one 4.5" port, while a titanium sublimation pump (Duniway Stockroom, TSP-275-003), specified to have a pumping speed of 300 L/s, is attached to the other port. The ion pump and the titanium sublimation pump are labeled as A and B in Fig. 2.3, respectively. Extra attention has to be paid to operate the titanium sublimation pump in order not to burn out the filaments while using the pump. According to our experience, the power (not the current) should be increased to maximum in five minutes at a constant rate. After waiting for on minute, the power should then be ramped off at a constant rate in another five minutes.

In addition to the two vacuum pumps, there is a Bayard-Alpert type ion

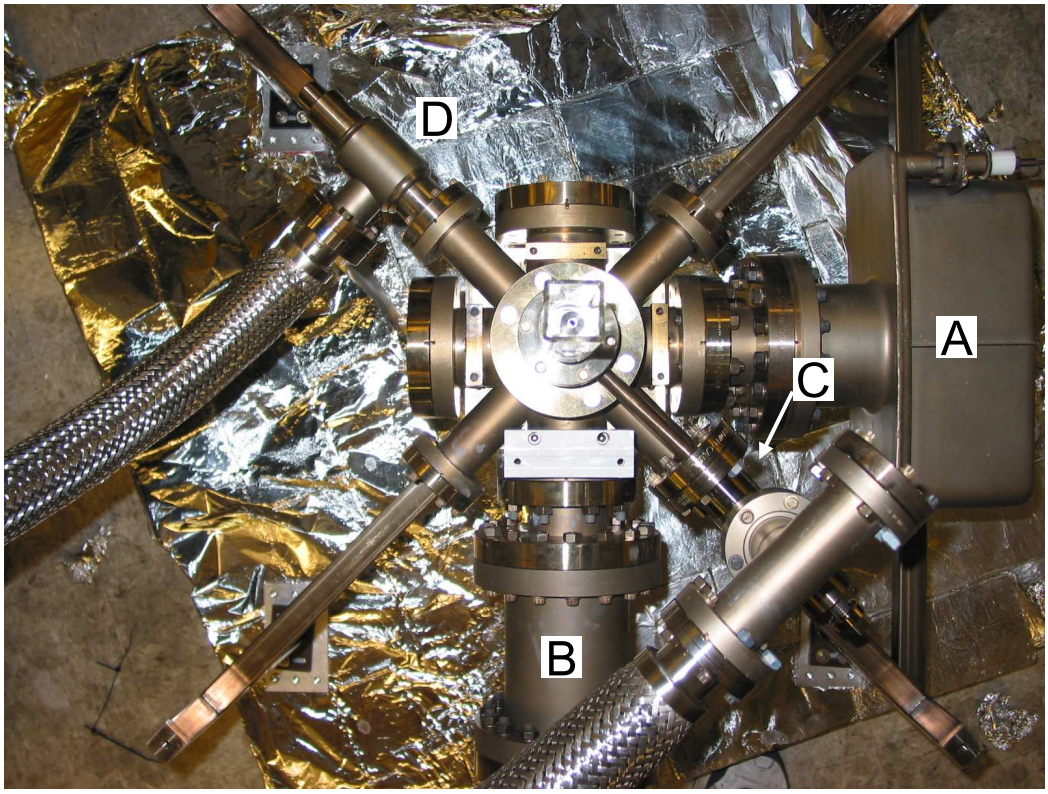

Figure 2.3: Middle vacuum chamber. A top view of the whole vacuum chamber shows the basic structure and elements attached to it, where A is the ion pump, B is the titanium sublimation pump, C is the ion gauge, and D is the all-metal valve used for connecting to a roughing-turbo pump station during the bake-out.

gauge (HPS, NTube) attached to one of the 2.75" ports. The ion gauge can only be used as a reference, not an accurate measurement of the pressure, since the pressure in the lower chamber is about 10^{-11} torr which is lower than the minimum pressure the ion gauge can measure (10^{-10} torr).

2.1.3 Lower Vacuum Chamber

The lower chamber, like the upper chamber, is also a glass cell (Hellma Cells). The glass cell is composed of a rectangular cell and a circular plate, labeled as A and B in Fig. 2.4(a), respectively. The rectangular cell has an outer dimension of 30 mm×30 mm×115 mm, a wall thickness of 5 mm, and is made of Spectrosil, which is a synthetic quartz of high purity and very good homogeneity. The circular plate is also made of Spectrosil and has a diameter of 75 mm, thickness of 17 mm, and a 20 mm hole in the center. The glass cell is assembled by the means of "optical contacting," in which each individual piece is joined together by molecular attraction between two surfaces but not by glue. In order for this to work, each surface has to be polished very smoothly and be free of dust. After they are brought together, the glass cell is then heated up under the melting point of the glass to reinforce the bond between the joined surfaces.

The glass cell is attached to the middle chamber via a Helicoflex seal (Garlock Helicoflex, H-307330 REV NC), a type of glass-to-metal seal. The Helicoflex seal (Fig. 2.4(b)) has two delta shape ridges (labeled as D in Fig. 2.4(b)) on the top and bottom of the "metal jacket," (labeled as E in Fig. 2.4(b)) which envelops a helical spring. As the "metal jacket" is under compression, the ridges cut into the glass and form a seal by face-to-face contact. During the compression, the helical spring provides an elastic force, pushing the ridges into the glass. A flange

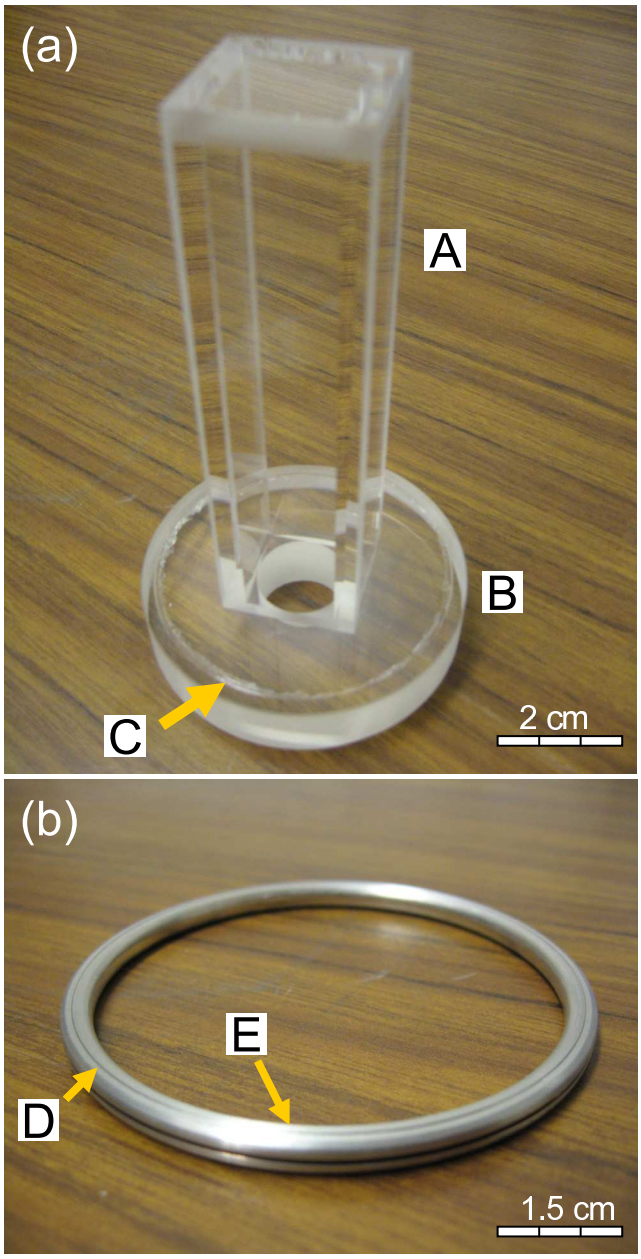

Figure 2.4: Lower vacuum chamber. (a) The lower chamber is basically a glass cell, consisting of a rectangular cell (A) and a circular plate (B). C shows the vestige caused by the Helicoflex seal. (b) Helicoflex seal is composed of a "metal jacket" (E), enveloping a helical spring, with two delta shape ridges (D) on the top and bottom.

between the middle and lower chambers is therefore specially designed to create such a compression. A vestige caused by the seal can be seen in Fig. 2.4(a), labeled as C.

2.2 Near Resonant Lasers

Lasers with frequencies near the transition frequencies of the rubidium (^{87}Rb) atom's D_2 line ($\sim$ 780 nm) are used in our experiment for many purposes. These include the MOT and repump beams for the magneto-optical trap (MOT), the probe beam for imaging, the push beam for moving the atoms from one place to another, and the optical pumping beam for manipulating the internal states of the atoms. The frequencies of these beams relative to the level spacings of the ^{87}Rb D_2 transition hyperfine structure are shown in Fig. 2.5.

In order to produce enough power in each beam, two Littrow-configured grating-stabilized diode laser systems [10, 11, 12] are used in the experiments. One, locked to the $F = 1 \rightarrow 1/2$ crossover transition, is used to create the repump beam; and the second, red-shifted by 147 MHz in frequency and locked to the $F = 2 \rightarrow 2/3$ crossover transition, is used to injection-lock three free-running diode lasers which distribute into the rest of the beams.

2.2.1 The Repump Laser

The repump laser used in our experiment is a grating-stabilized diode laser system constructed in the Littrow configuration (Fig. 2.6), in which a grating sits in front of the diode laser and the first order diffraction is directly reflected back along the incident beam while the zeroth order is used as the output beam. The diode laser (Intelite Inc, MLD780-100S5P) has a single-mode output at a typical lasing

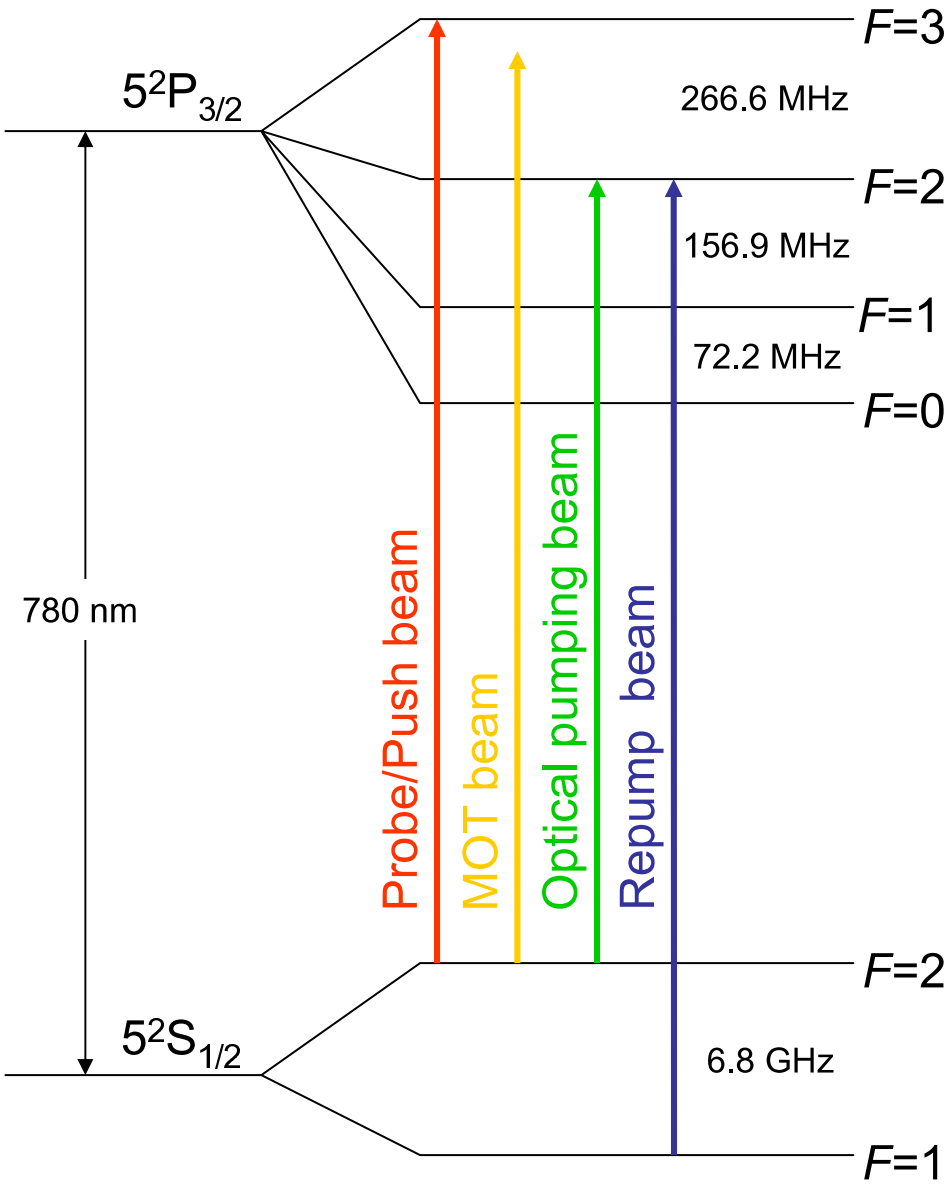

Figure 2.5: Different frequencies of near resonant lasers used in the experiment. Also shown are the level spacings of Rb^{87} D_2 transition hyperfine structure.

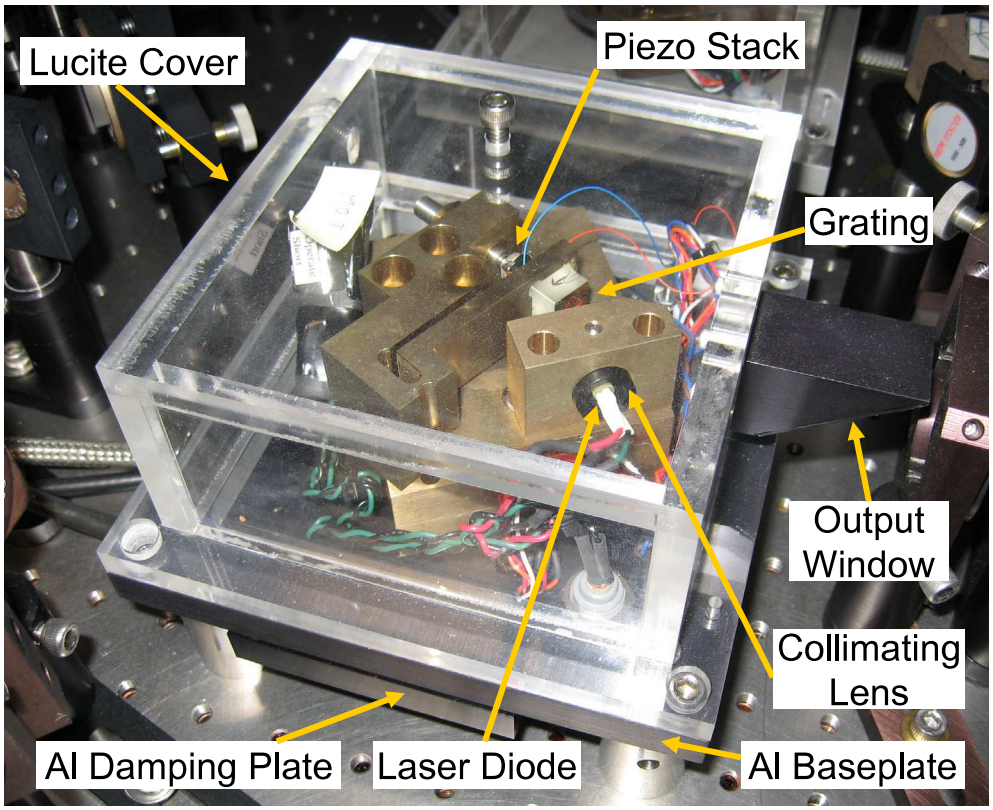

Figure 2.6: Two Littrow-configured grating-stabilized diode laser systems are used in the experiment to produce the repump beam and to injection-lock three free-running diode lasers which distribute into rest of the beams.

wavelength of 780 nm with a maximum power of 100 mW and an operating current of 140 mA. The linewidth is measured to have a upper bound of 1.5 MHz.

The diode is housed in a f=4.5 mm collimation tube (Thorlabs, LT230P-B) with a numerical aperture of 0.55. The tube is then mounted in a housing made of bronze which is non-fatigable and has a high thermal conductivity. The bronze housing sits on another bronze baseplate, where a 50 kΩ glass-bead thermistor (Fenwal Electronics) is inserted to monitor the temperature and sends the feedback to a thermoelectric cooler (Melcor, CP1.0-127-05L) attached to the bottom of the baseplate. An aluminum plate is in contact with the thermoelectric cooler on the other side with a damping material attached below, serving as a heat reservoir. The laser system is isolated from the outside by a Lucite cover.

The current sent to the diode is controlled by a homebuilt PID circuit [13]. In order to protect the diode from electric shocks, several forward and reverse bias diodes are connected near to the diode as suggested in [11]. In addition, a ferrite bead and a low pass filter are added as a noise filter. The temperature of the diode, on the other hand, is controlled by a unit designed and produced by Leo Hollberg's group at NIST-Boulder.

A grating is mounted at an angle with respect to the diode. The grating (Edmund Scientific), with a 500 A gold coating [14, 15], has a size of 12.5 mm$\times$12.5 mm, a ruling of R=1200 grooves/mm, and a blazed angle of 17°. The angle can be determined from the Littrow configuration,

$$\lambda = 2d\sin\alpha, \tag{2.2}$$

where $d = 1/R$ is the spacing of the grooves and $\lambda = 780$ nm is the wavelength of the laser beam. In order to operate the diode on one of the ^{87}Rb absorption lines with

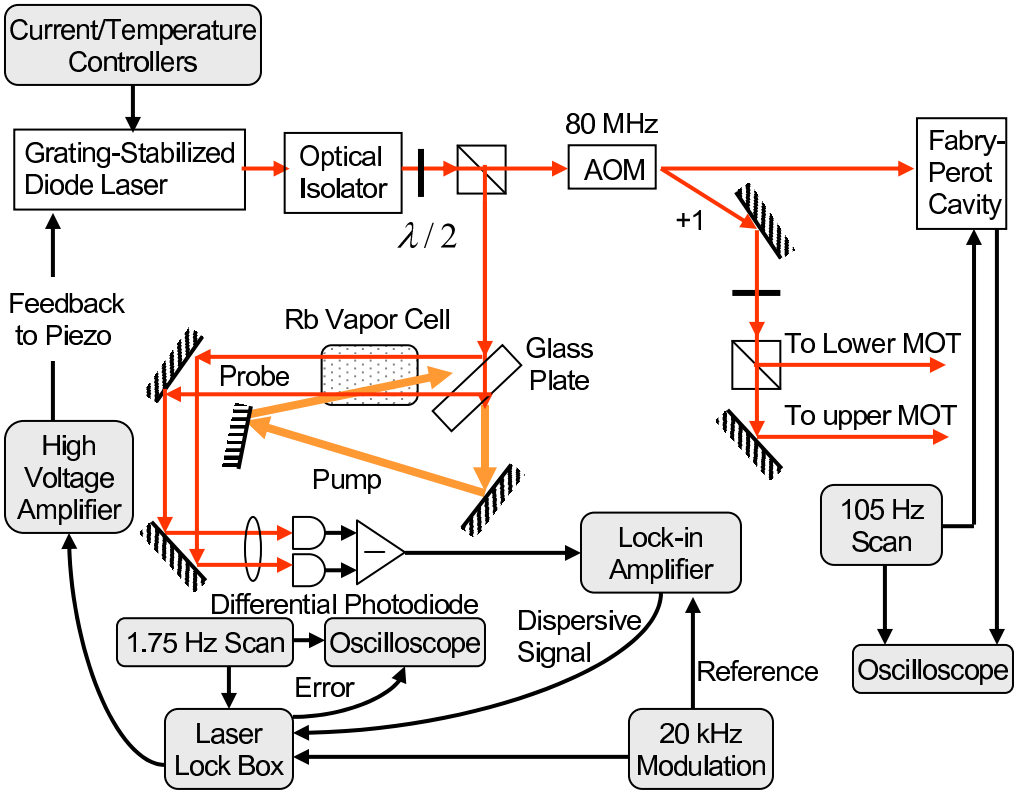

Figure 2.7: Beam distribution and layout of saturated absorption spectroscopy for the repump laser. The optical isolator is a model 713 by ConOptics and the lock-in amplifier is a model SR510 by SRS.

single mode, a proper alignment of the angle of the grating with respect to the diode is needed (a description of the alignment procedure can be found in [16]). The angle of the grating can be mechanically adjusted by two fine-adjustment screws (Newport, 9300-series). In addition, a stack of three piezo discs (American Piezo Ceramics, 8 mm×2.54 mm, 1.35 μm/kV) is placed between one of the fine-adjustment screws and the grating for the modulation purpose in the saturated absorption spectroscopy. The piezo stack is driven by a high-voltage amplifier (Trek, 601B).

The frequency of the repump laser is locked to the $F = 1 \rightarrow 1/2$ crossover

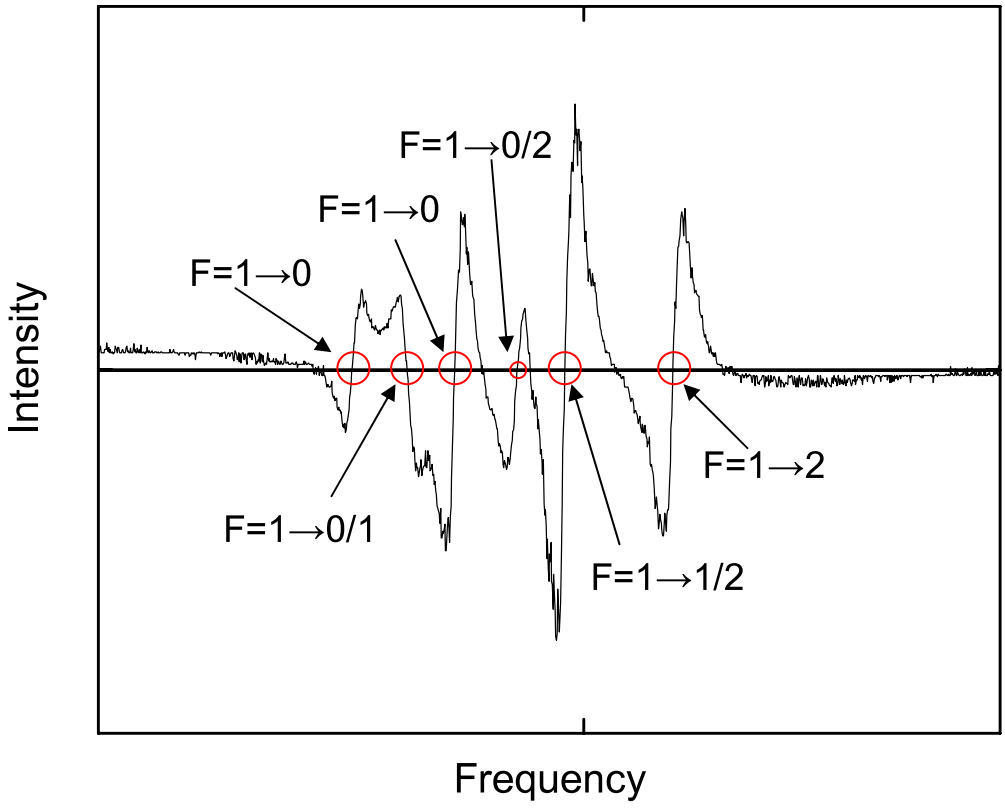

Figure 2.8: Saturated absorption spectrum for the ^{87}Rb D_2 line $F = 1 \rightarrow F'$ hyperfine manifold. The repump laser is locked to the $F = 1 \rightarrow 1/2$ crossover transition.

transition of the ^{87}Rb D_2 line through the use of the saturated absorption spectroscopy, which is the strongest dispersive line of the $F = 1 \rightarrow F'$ transitions. Fig. 2.7 shows schematically the setup of the optics and the electronics for the spectroscopy. The dispersive error signal is obtained by dithering the laser frequency via a small 20 kHz modulation of the piezo stack. The measured spectrum for our setup is shown in Fig. 2.8 as well as the corresponding transitions. Fig. 2.7 also shows the beam distribution to the upper and lower MOT, where a 80 MHz AOM is used to shift the frequency of the laser to 1.5 MHz red of the desired $F = 1 \rightarrow 2$ transition.

2.2.2 The MOT Master Laser

The MOT master laser has exactly the same mechanical design as the repump laser except the frequency, red-shifted by 147 MHz, is locked to the $F = 2 \rightarrow 2/3$ crossover transition which is the strongest dispersive signal of the $F = 2 \rightarrow F'$ transitions for the ^{87}Rb D_2 line. The locking scheme is slightly different from the repump laser in a way such that one of the laser beams involved in the saturated absorption spectroscopy is frequency-modulated between $\pm$ 1 MHz at 10 kHz. The advantage of this locking scheme is that it does not modulate the beam that is actually going to the experiment.

A schematic of the optic and electronic setup is shown in Fig. 2.9. The 80 MHz double-passed AOM allows the laser frequency to be detuned 80 MHz to 160 MHz red of the $F = 2 \rightarrow 3$ transition, a cycling transition necessary for the magneto-optic trap (MOT) to work. With the use of another single-pass 80 MHz AOM (also acting as a fast shutter), the MOT master will have a detuning between 0 and 80 MHz red of resonance, which covers all frequencies required by the experiment. Fig. 2.10 shows the measured spectrum along with the corresponding transitions.

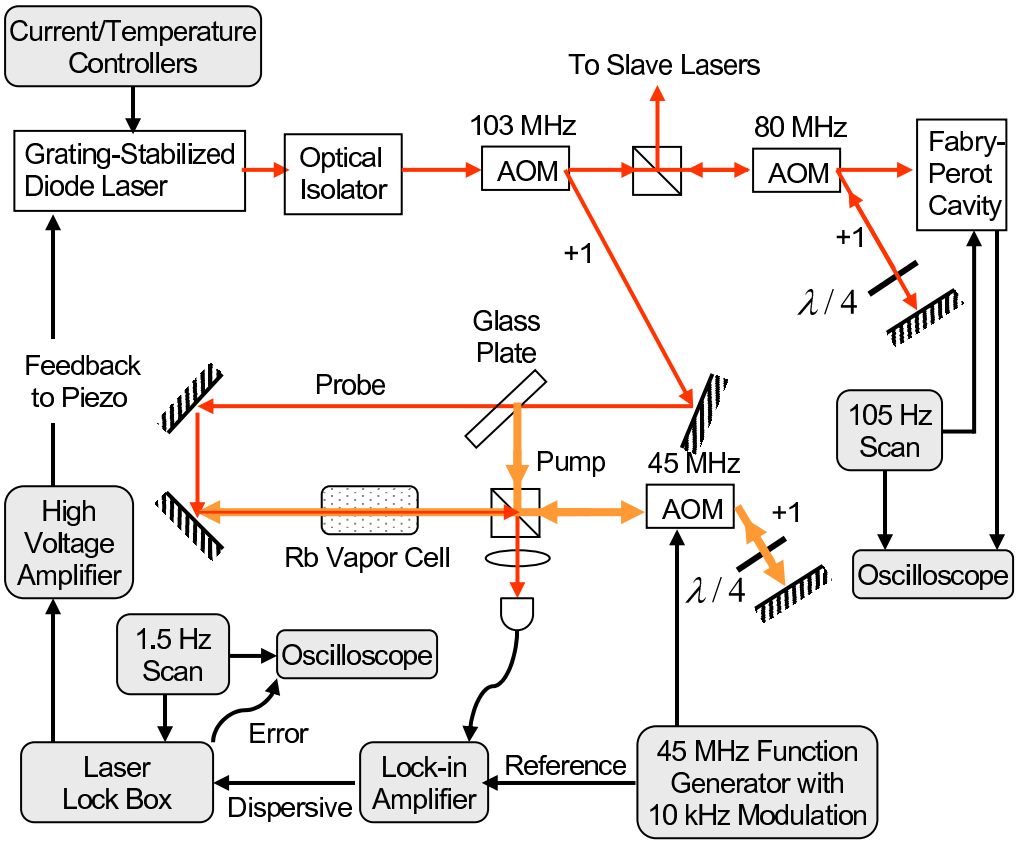

Figure 2.9: Beam distribution and layout of saturated absorption spectroscopy for the MOT master laser. The optical isolator is a model 713 by ConOptics and the lock-in amplifier is a model SR510 by SRS.

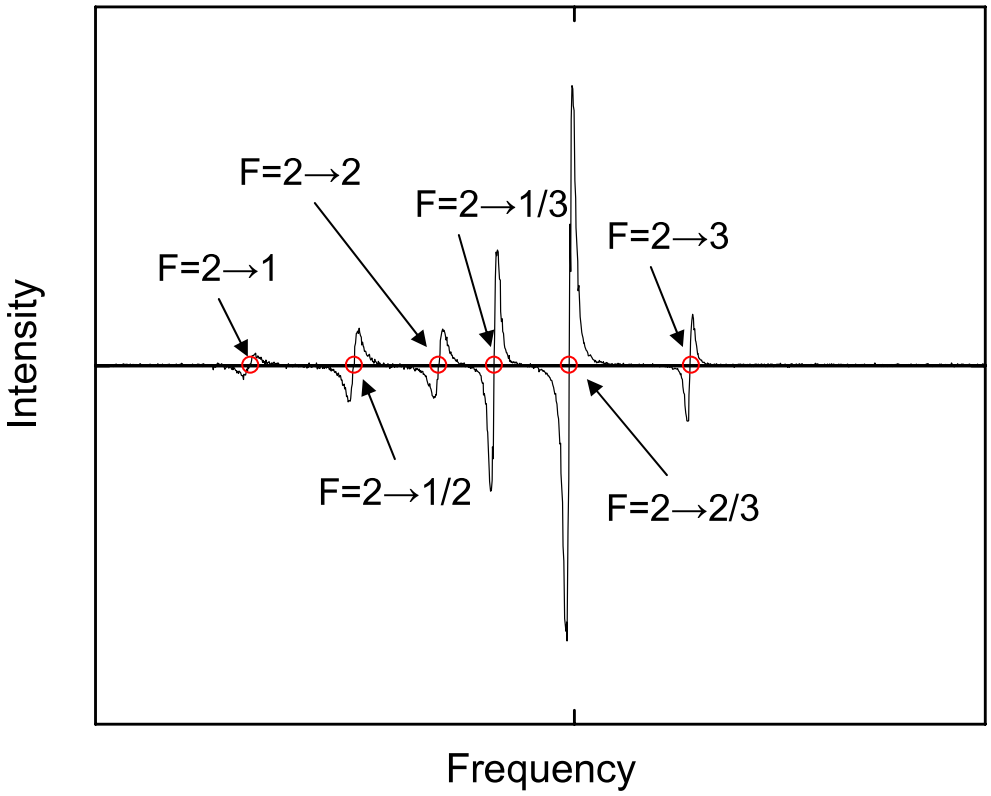

Figure 2.10: Saturated absorption spectrum for the Rb^{87} D_2 line $F = 2 \rightarrow F'$ hyperfine manifold. The MOT master laser is locked to the $F = 2 \rightarrow 2/3$ crossover transition.

2.2.3 The Slave Lasers

Slave lasers are the free running diodes with output frequency injection-locked by the MOT master laser. Therefore, the mechanical design of these systems is almost identical to the repump or MOT master laser except there is no grating (thus they do not need the setup for saturated absorption spectroscopy) and the Lucite cover is replaced by an aluminum cover (Fig. 2.11(a)-(b)). A small amount of light from the MOT master laser must be delivered into the rejection port of each slave laser's optical isolator (ConOptics, 712B), thus following the diode's output beam path to injection-lock the frequency of each slave laser.

The diode (Digi-Key, GH0781JA2C) has a single-mode output at a typical lasing wavelength of 784 nm with a maximum power of 120 mW and an operating current of 167 mA. The current sent to the diode, like the repump and MOT master lasers, is also controlled by a homebuilt PID circuit [13]. The temperature is regulated by another homebuilt circuit based on an ultra-stable temperature controller from Wavelength Electronics (model WTC3243). A description of the alignment procedure for the injection lock can be found in [16]. Fig. 2.11(c) shows the beam distributions of three slave lasers, which produce the upper MOT horizontal beam, the push beam, the vertical probe beam, the upper MOT diagonal beam, the horizontal probe beam, the optical pumping beam, the lower MOT beam, and the single atom detection (SAD) MOT beam.

2.3 The Magnetic Trap

Our magnetic trap, located around the lower vacuum chamber, has two purposes: providing the magnetic field needed for (1) the magneto-optic trap (MOT) and (2) the laser-free magnetic trapping for the evaporative cooling, which is a crucial part

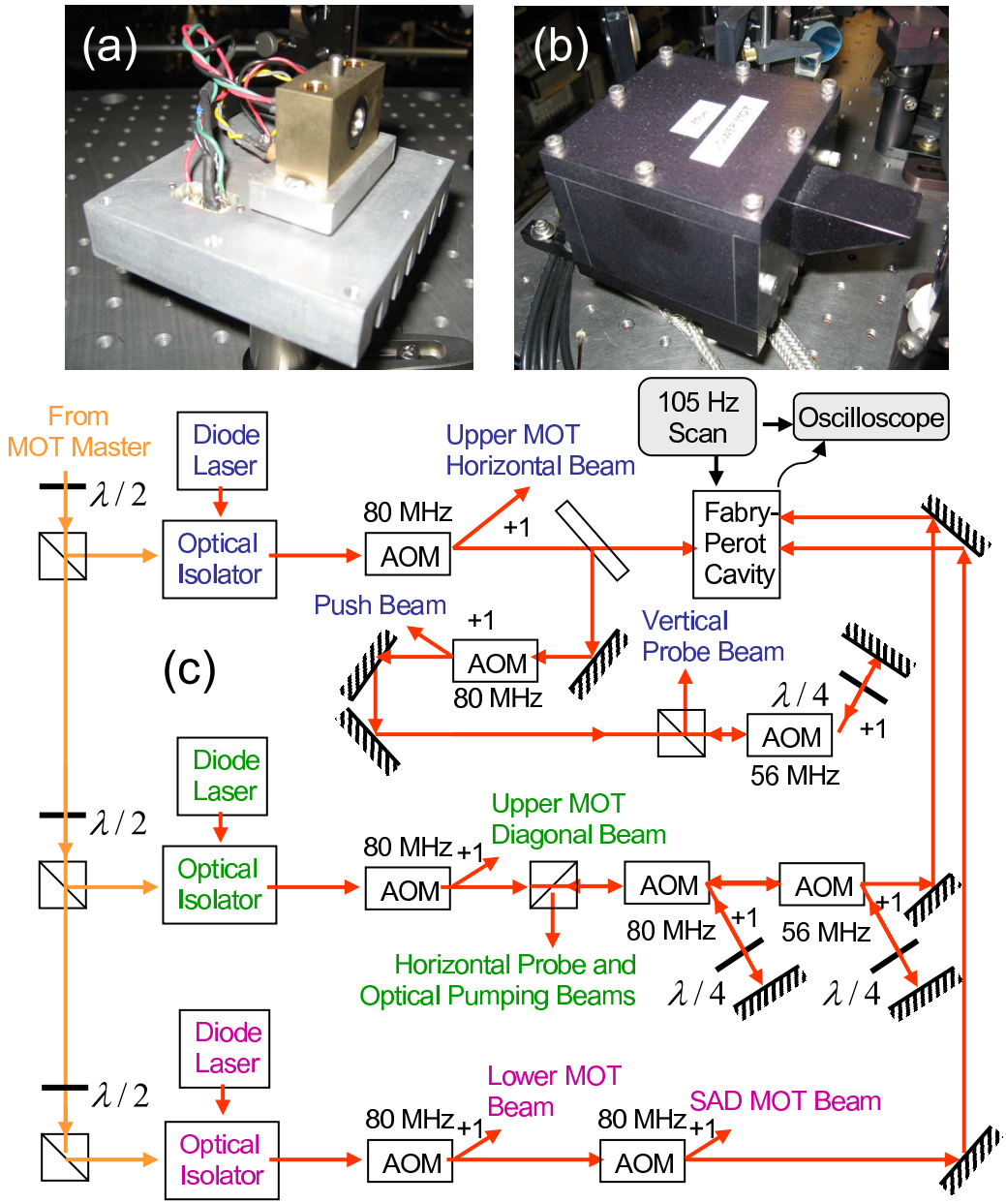

Figure 2.11: The slave laser shown (a) without the cover and (b) with the cover. (c) Beam distributions of three slave lasers.

of obtaining Bose-Einstein condensation.

The configuration of our magnetic trap has the same design as the quadrupole Ioffe configuration (QUIC) trap [7], which combines the quadrupole and Ioffe configurations, and thus has a pair of quadrupole coils and one Ioffe coil as shown in Fig. 2.12. All coils are in series with a 60 V, 30 A power supply (Lambda EMI, TCR 605-30-1-D) which operates at constant voltage mode. The total voltage across the coils is regulated by a PID circuit using several operational amplifiers (TI, OPA549) in parallel. To regulate the current in the quadrupole and Ioffe coils, a series of MOSFETs (International Rectifier, IRF1405) is connected to each coil in parallel, acting as a shunt. During typical operation, a constant current of 28 A flows through every coil. The measured trapping frequencies at this condition are $\omega_{ax} = 2\pi \times 20$ Hz along the direction of Ioffe coil's axis and $\omega_{rad} = 2\pi \times 200$ Hz in the radial direction orthogonal to the axis. The offset of the magnetic field is about 1.4 G.

Fig. 2.12(a) shows a coil (quadrupole coil, in particular) before being assembled. A view of the completed magnetic trap is shown in Fig. 2.12(b) as well as the water cooling tubes and the auxiliary coils (wrapping around the coil holder) used for adding magnetic field offsets and optical pumping. Details about the construction of the coils as well as their cooling assembly and the control electronics can be found in [13, 16].

The advantages of this configuration are the low power dissipation and a small number of coils (only three). However, one disadvantage is that the trap center is shifted to the side. Therefore, it requires some means to move the center back. One way is to reduce the current in the two quadrupole coils while keeping the current unchanged in the Ioffe coil. This results in a decrease of the trapping

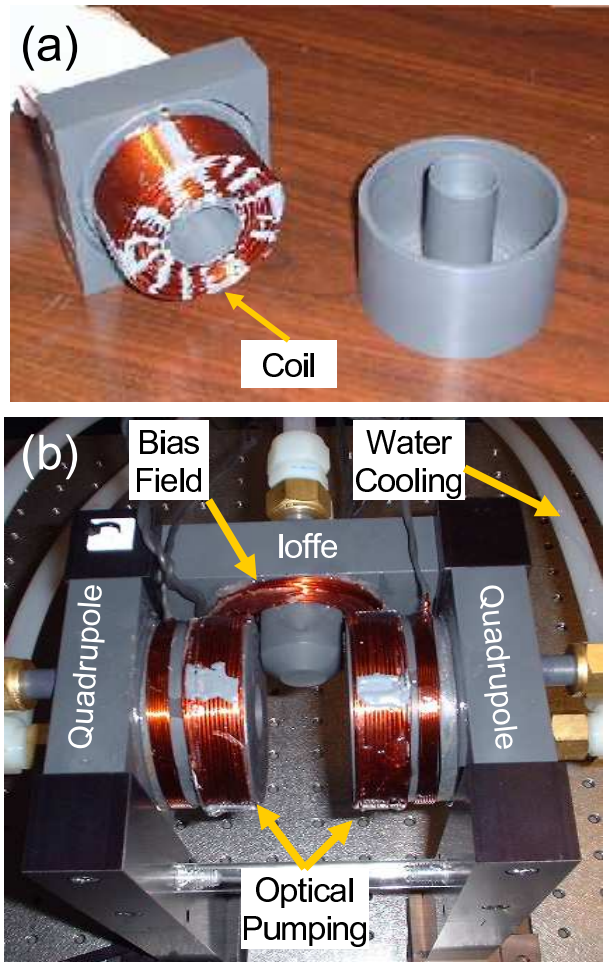

Figure 2.12: Quadrupole-Ioffe-configuration (QUIC) trap combines the quadrupole and Ioffe configuration. (a) Coil before being assembled. (b) A completed look at the QUIC trap with the water cooling tubes and the auxiliary coils, wrapping around the coil holder, used for adding magnetic field offset and optical pumping.

frequency (from $\sim$ 200 Hz to $\sim$ 20 Hz) but can be compensated for by loading the atoms into an optical trap.

2.4 The Optical Trap

Optical traps are used in our experiments to create a variety of trapping potentials in order to manipulate the properties of the atoms. Roughly speaking, they can be divided into two categories: blue-far-detuned (repulsive) and red-far-detuned (attractive) traps.

The blue-detuned optical traps are formed by beams derived from a 10 W, 532 nm Nd:Vanadate laser (Coherent, Verdi V-10). This includes a pair of horizontal TEM_{01} optical sheets, a pair of vertical TEM_{01} optical sheets, and several optical tweezers. The red-detuned optical trap contains a circular trap and an optical sheet. Both of them are derived from a 10 W, 1064 nm Ytterbium doped fiber laser (IPG-Photonics, YLC-10-1064). All beams are shaped and spatially filtered before being focused into the lower chamber where the atoms are prepared. A layout of the optics producing these beams is shown in Fig. 2.13.

2.5 Single Atom Detection

Single atom detection is at the heart of directly studying quantum statistics in quantum degenerate gases. For example, to study the superfluid-to-Mott insulator transition in an optical lattice [17], one would like to measure the number statistics on each site, which might contain one or two atoms if the system is in the deep Mott insulator regime. Another example is the study of the Tonks-Girardeau gas in one-dimensional bosonic gas with repulsive interaction [18, 19, 20]. Atoms in this

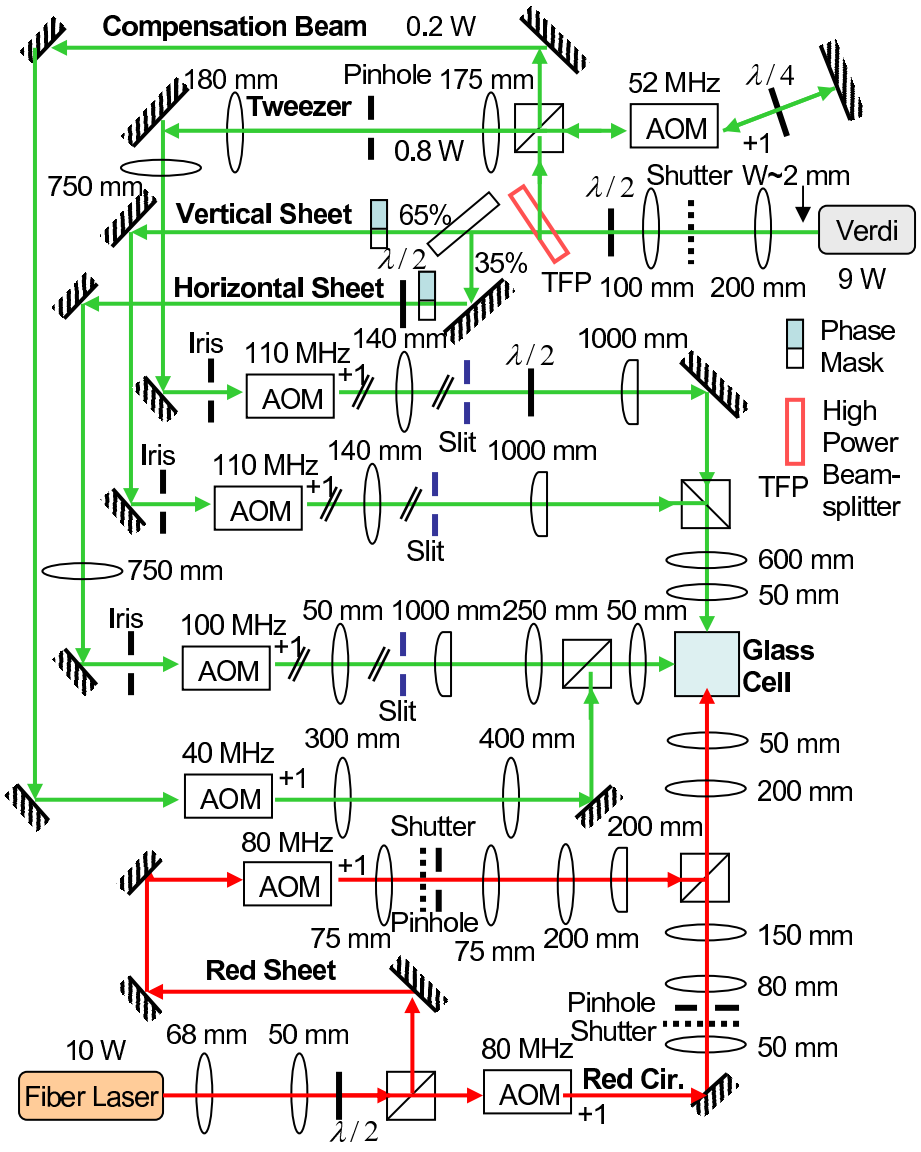

Figure 2.13: Layout of optics producing the optical traps.

regime become localized in space (due to the strong interaction) with a density on the order of one atom per few micrometers. Therefore, it would be nice to be able to detect single atoms and reveal the number statistics as a function of position. One can probably use absorption imaging to study these problems, since it has the property of spatial resolution. However, for atom number smaller than one thousand, absorption imaging has a poor resolution.

Our single atom detection system uses the same design as in [21]. It is basically a fluorescence detection using a specially designed lens combo. The lens combo is composed of four BK7 spherical lenses with the aberration of one surface corrected by other surfaces, resulting in a minimized squared sum of the spherical aberrations up to 7th order and third order coma and astigmatism. The main features of this lens combo are: (1) large working distance of 36 mm, (2) near diffraction-limited spot size of $\sim 2\mu$m on axis, (3) large field of view of 1 mm^2, and (4) a numerical aperture of 0.29. The lens combo also takes into account the aberration from the wall of the glass cell (lower vacuum chamber). Although the lens combo is originally designed for 832 nm light, it retains the diffraction-limited performance from 400 nm to 1064 nm.

The fluorescence required for the detection is provided by an on-resonant magneto-optic trap (MOT) with a strong magnetic gradient, which excites the atoms and gives a strong confinement (Fig. 2.14(a)). The MOT has a beam diameter of $\sim$ 1 mm, a beam intensity of 65 mW/cm^2, a detuning of about 5 MHz, and a magnetic gradient of 260 G/cm. About 2 % of the spontaneously emitted photons are collected and collimated by the lens combo. After that, the photons travel approximately for 8 mm before encountering a spatial filter which consists of a pinhole sandwiched by two lenses. The purpose of the spatial filter is to filter out the unwanted background

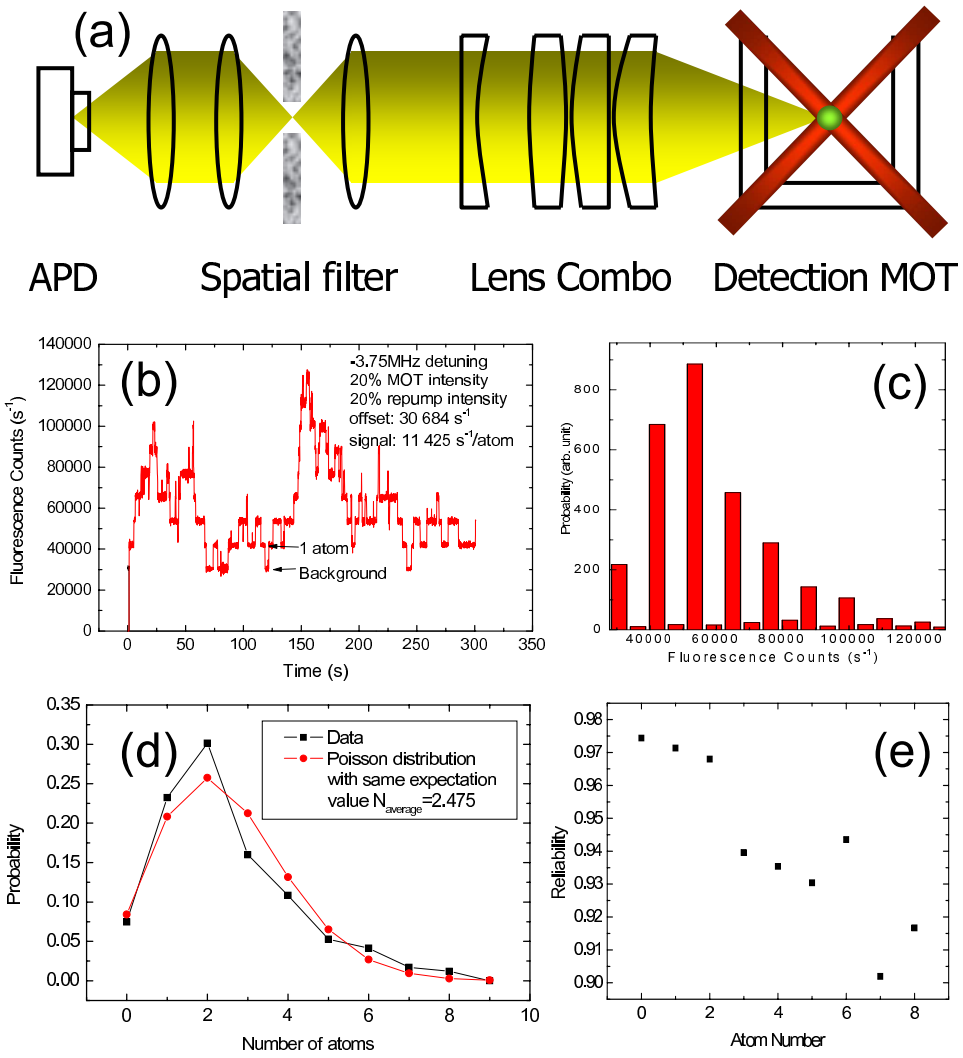

Figure 2.14: Single atom detection system. (a) Schematic of optics setup for the single atom detection. (b) Continuous detection of the random capture from the background vapor. The discretized step shows the fluorescence rate emitted by one atom. (c) Histogram of the data obtained in (b). (d) Number statistics in the MOT has a Poissonian characteristic. (e) Reliability of 97 % has been measured for the atom counting of one and two atoms.

scattering. In order to eliminate any fluctuation which might result from the motion of the atoms in the MOT, the size of the pinhole (300 μm) is chosen to be large enough to cover the size of the MOT. The collected fluorescence is then focused by a final 50 mm lens into an avanlanche photodiode (Perkin Elmer, SPCM-AQR-14) which operates at the single-phonton-counting mode.

The avanlanche photodiode (APD) has an active area of 175 μm, a quantum efficiency of $\sim$ 60 % at 780 nm, a maximum dark count of 100 counts/s, and a saturated count rate at 5 million counts/s. In order to block out any unwanted light into the APD, a mechanical shutter (Uniblitz, VS25S2Z0) and an interference filter with a 10 nm bandwidth centered at 780 nm are place in front of the APD. Although the filter reduces the intensity at 780 nm by a factor of about 2, it suppresses the intensity outside the bandwidth by about four orders of magnitude. During the detection, the APD is activated for 2 seconds, and the measured fluorescence counts are averaged for every 10 ms.

Fig. 2.14(b) shows test data of this system. In this case, atoms are randomly captured from the background vapor and also have the chance to escape from the MOT. The discretized step corresponds to the fluorescence emitted by a single atom per second. This can also be seen in the histogram plot in Fig. 2.14(c). Since the process is a random event, the captured atom numbers in the MOT shows the behavior of Posissonian statistics (Fig. 2.14(d)). When there are one or two atoms in the MOT, the probability of measuring the same atom in the following 100 ms is nearly 97%, indicating a high reliability of the atom counting (Fig. 2.14(e)).

To further explore our ability to detect a single atom, we also use a charged couple device (CCD) camera (Apogee, Alta Series, U47+) to image the atoms in the MOT. The APD measurement is correlated to the CCD measurement in such a

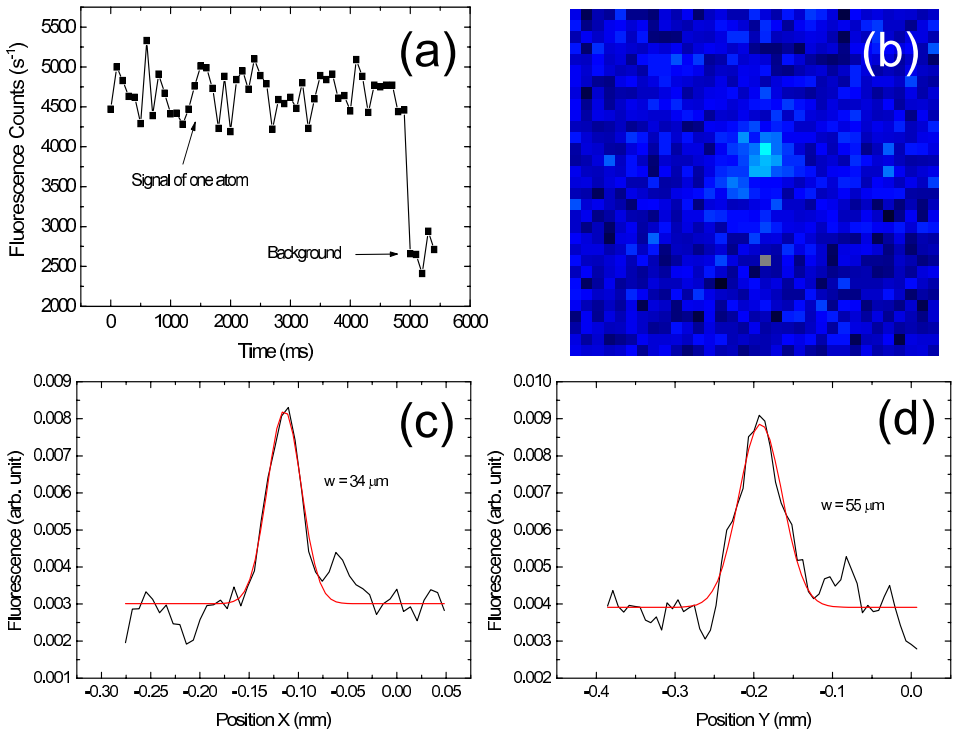

Figure 2.15: Single atom in the MOT. (a) Step-wise signal obtained by APD. (b) CCD image of one atom. (c) Spatial profile of detected single atom in X direction. (d) Spatial profile of detected single atom in Y direction.

way that we know exactly how many atoms are detected by the CCD camera. Two such measurements are shown in Fig. 2.15(a) and (b), where a single atom can be seen on the CCD camera. Spatial profiles of the detected single atom are shown in Fig. 2.15(c) and (d).

Chapter 3

Low-Dimensional Bose-Einstein Condensate

Single-site control and addressability are the keys for directly studying and manipulating the properties of low-dimensional Bose-Einstein condensates (BECs). To achieve this, one would need a BEC in a single trap. This chapter describes our experimental means for obtaining low-dimensional BECs in a single optical trap with trapping frequencies comparable to what one can achieve in an optical lattice.

3.1 Criterion for Low-Dimensional BEC

A weakly interacting, trapped Bose-Einstein condensate (BEC) is low-dimensional, or "quasi"-low-dimensional, when the motion of the atoms in the BEC is restricted only to one or two dimensions. The "freezing" of the motion in the other directions means that the atoms will always stay in the ground state; therefore, the interaction energy E_{int} and the thermal energy k_BT (k_B is the Boltzmann constant and T is the temperature of the atoms) of the atoms have to be much smaller than the

energy level spacing of the trap in the restricted directions. Thus, for a trap that is harmonic in the tightly confining direction(s), the low-dimensional regime is reached when

$$E_{int},\ k_B T \ll \hbar\omega_t, \tag{3.1}$$

where E_{int} is the peak interaction energy which is equal to the chemical potential μ_{3D} in three-dimensions (3D), and ω_t is the trapping frequency in the tightly confining direction(s): that is, the radial ($\perp$) direction in the one-dimension (1D) or the axial (z) direction in two-dimensions (2D).

An equivalent criterion can be obtained by rewriting Eq. (3.1) with $E_{int} = g_{3D} n_0$, where $g_{3D} = 4\pi\hbar^2 a_s/m$ is the coupling constant, with a_s being the s-wave scattering length, n_0 the peak density, and m the mass. Then we get

$$\frac{1}{\sqrt{4\pi n_0 a_s}} \ll \sqrt{\frac{\hbar}{m\omega_t}}, \tag{3.2}$$

where the term on the left-hand side is the healing length $\xi = 1/\sqrt{4\pi n_0 a_s}$ as defined in [22, 23] (a different definition of $\xi' = 1/\sqrt{8\pi n_0 a_s}$ is being used in [2]), and the term on the right-hand side is the harmonic oscillator length in the tightly confining direction(s) $a_t = \sqrt{\hbar/m\omega_t}$. Therefore, when the low-dimensional regime is reached, it is also true that the healing length is much smaller than the harmonic oscillator length in the tightly confining direction(s), that is,

$$\xi \ll a_t. \tag{3.3}$$

The criterion for low dimensions actually puts a restriction on the maximum atom number allowed in the system. This can be seen from Eq. (3.1): in order to fulfill the condition of low dimensions, one would need a strong confinement to

increase the energy level spacing, or a low atomic density to reduce the interaction energy. Unfortunately, with restricted laser power, the confinement cannot be increased unlimitedly. Moreover, the resolution of the camera always sets a lower bound for the atomic density. These restrictions thus result in a maximum atom number which can be achieved in a low-dimensional BEC.

The maximum atom number can be calculated from the crossover of Eq. (3.1),

$$\mu_{3D}(N_{max}) = \hbar\omega_t, \tag{3.4}$$

if the chemical potential is known as a function of atom number, $\mu_{3D} = \mu_{3D}(N)$. To calculate $\mu_{3D}(N)$, let's consider a BEC trapped in a potential $V(x_i)$ with harmonic form(s) $m\omega_i^2 x_i^2/2$ in the tightly confining direction(s), where ω_i is the trapping frequency in the i direction.

For the large-N limit (or, more strictly, $Na_s/\bar{a} \gg 1$ where $\bar{a}$ is the harmonic oscillator length corresponding to the geometric mean trapping frequency $\bar{\omega} = (\omega_x\omega_y\omega_z)^{1/3}$), the density distribution $n(x_i)$ of the atoms is related to $\mu_{3D}(N)$ through $n(r) = (\mu_{3D} - V(r))/g_{3D}$ given by the Thomas-Fermi (TF) approximation (Eq. (1.21)). Thus $\mu_{3D}(N)$ can be computed by integrating the density $n(x_i)$ over the space to obtain the total atom number $N(\mu_{3D}) = \int n(x_i)d^3x_i$. The calculation is somewhat tricky but can be made easier if one rescales x_i as $\bar{x_i} \equiv \omega_i x_i$.

The maximum atom numbers N_{max} allowed in different dimensions and trap configurations are summarized in Table. 3.1. They only depends on the trapping frequencies and the size of the atomic cloud. For trap parameters achievable in the current BEC experiments, $N_{max} \cong 10^3 - 10^4$ for the 1D case and $N_{max} \cong 10^4 - 10^5$ for the 2D case.

Table 3.1: Maximum atom numbers in one and two-dimensional BECs.

Dimension	Potential $V(x_i)$ at $n(x_i) > 0$	Maximum atom number N_{max}
2D	$m(\omega_x^2 x^2 + \omega_y^2 y^2 + \omega_z^2 z^2)/2$	$\sqrt{32\hbar\omega_z^3/225ma_s^2\omega_\perp^4}$
2D (box)	$m\omega_z^2 z^2/2$	$\sqrt{2\hbar m L_x^2 L_y^2 \omega_z/6\pi a_s}$ †
1D	$m(\omega_x^2 x^2 + \omega_y^2 y^2 + \omega_z^2 z^2)/2$	$\sqrt{32\hbar\omega_\perp/225ma_s^2\omega_z^2}$
1D (box)	$m(\omega_x^2 x^2 + \omega_y^2 y^2)/2$	$L_z/4a_s$ ‡

† L_x and L_y are the extents of the cloud in the x and y directions respectively.
‡ L_z is the extent of the cloud in the z direction.

3.2 Why Low-Dimensional?

As a consequence of increased phase fluctuations, low-dimensional systems have many interesting physics which do not exist in three-dimensions. For example, below the critical temperature T_c, a trapped two-dimensional atomic gas does not immediately become a BEC but first undergoes Berezinski-Kosterlitz-Thouless transition [24, 25] and forms a "quasi-condensate," [23] which associates the formation of vortex pairs with opposite circulations.

Unique phase transition also exists in one-dimension. For instance, as the atomic density decreases, a trapped one-dimensional gas with contact potential becomes more and more correlated and enters the Tonks-Girardeau regime [18, 19, 20]. Atoms in this regime strongly interact with each other and behave like fermions ("fermionization).

In addition to these specisl phase transitions, topological excitation like solitons is also more stable in low-dimensional than in three-dimensional system, where solitons might break up into vortices or phonons. Moreover, the increased phase fluctuation is expected to change the nature of collective excitation in low dimensions [26, 27].

In recent years, great efforts have been made to realize BEC in one dimension

[28, 29] and two dimension [30, 31] in optical lattices. Low-dimensional BECs were also achieved in a single optical or magnetic trap [32]. Followed by these successes, the Berezinski-Kosterlitz-Thouless transition and Tonks-Girardeau gases were observed in 2D BECs [33] and 1D BECs [34, 35], respectively. Collective excitations were also measured in one-dimensional BECs [36]. Among these trap configurations, the experiments with optical lattices have stronger signals due to arrays of BECs. The experiments in a single trap, on the other hand, has the property of addressability.

3.3 Experiment

This section describes the construction of a single optical trap which has trapping frequencies comparable to what one can achieve in an optical lattice. Using this novel technique, we have obtained low-dimensional Bose-Einstein condensate in a single trap. This configuration allows single-site control and addressibility.

3.3.1 Decompressed Quadrupole-Ioffe-Configuration Trap

Since our Quadrupole-Ioffe-Configuration (QUIC) trap does not have a high enough trapping frequency to produce a low-dimensional Bose-Einstein condensate (BEC), an optical trap with a starting point inside the magnetic trap is needed. However, the center of the QUIC trap, about 8 mm from the center and 4.5 mm from the wall of the glass cell, does not have good optical access. Thus, the first task is to move the atoms (not necessarily a BEC) back to the center of our science chamber- the glass cell.

The atoms which are being transfered do not have to be BEC atoms. Actually, it might be even better to transfer non-BEC atoms because they are less

sensitive to any sort of heating during the transfer. Therefore, a large cloud of cold atoms is first prepared in the QUIC trap by using a smaller bias magnetic field B_0 (compared to the value used for obtaining BEC) during the evaporative cooling while keeping the end RF frequency the same.

The transfer is then accomplished by ramping down the current in the quadrupole coils. In order to adiabatically transfer the atoms back to the center of the science chamber, the kink due to the change of the current at the beginning of the transfer is carefully minimized. Furthermore, the quadrupole current is ramped down in a way such that the atoms always feel a continuous change of force or acceleration. Nearly no excitation is created during the process. This is verified by transferring a BEC back and forth from the QUIC trap to the final location and observe no heating. Since the bias magnetic field is also ramped off at the end, extra care is made to switch the RF completely off before the transfer. Several auxiliary coils are also used to balance the transfer motion of the atoms.

In typical operations, the quadrupole current I_{QP} is ramped down from 28 A to 9 A in $T = 3$ seconds, resulting in a position shift of about 7 mm. The position of the atoms x_{atom} is calibrated with the quadrupole current $I_{QP} = (1+0.16124x_{atom} + 0.0161x_{atom}^2 + 0.0011x_{atom}^3 + 4.7198 \times 10^{-5}x_{atom}^4 + 9.1415 \times 10^{-7}x_{atom}^5)I_{Ioffe}$, where $I_{Ioffe} = 28$ A is the Ioffe current during the transfer (Fig 3.1 (a)), and is shifted in the form of a sinusoidal function with respect to the time, $x_{atom}(t) = \sin(\pi t/T)$. However, since the trap is more stable at a higher bias field B_0, the position shift is actually speeded up at the beginning by $s = 2$ times faster than the end in order to increase the bias field quickly to 10 G in the first 100 ms ($B_0 \sim 50$ G at the final

position). This is accomplished by "stretching" the time in the form of

$$t' = T\left[\frac{\left(\frac{t}{2T}+1\right)^{1+\frac{\ln 1/s}{\ln 3/2}}-1}{\frac{3}{2}^{1+\frac{\ln 1/s}{\ln 3/2}}-1}\right], \tag{3.5}$$

which is derived by solving the following simultaneous equations.

$$t' = C_1(t+C_2)^p - C_3, \tag{3.6}$$

$$t'(0) = 0, \tag{3.7}$$

$$t'(T) = T, \tag{3.8}$$

$$\left.\frac{dt'}{dt}\right|_{t=0} = s\left.\frac{dt'}{dt}\right|_{t=T}. \tag{3.9}$$

After the transfer, the atoms are left in the trap for another 300 ms to be stabilized. The horizontal position of the atoms is aligned to the center of the quadrupole trap by adjusting the horizontal auxiliary coils. The vertical position of the atoms, on the other hand, is aligned to a position about half the cloud size above the center of the quadrupole trap. This is done by using the earth field compensation coil in the vertical direction to lift the atoms up. About 10^6 cold atoms near BEC are prepared in such a symmetric magnetic trap with a trapping frequency of 20 Hz (Fig. 3.1(b)-(d)).

3.3.2 BEC in a Gravito-Optical Trap

After the atoms are transfered back to the center of the quadrupole trap, they are ready to be loaded into the optical trap. A 532 nm blue-detuned optical sheet propagating horizontally is ramped on just below the atoms in 300 ms while a 1064 nm red-detuned circular optical trap propagating vertically is ramped on around

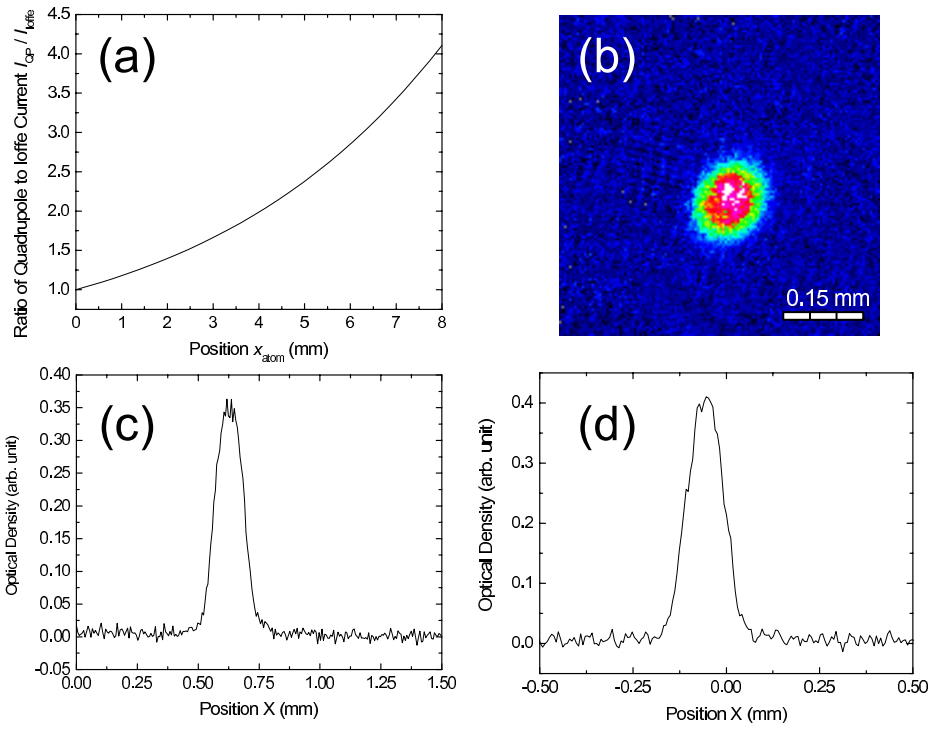

Figure 3.1: Decompressed Quadrupole-Ioffe-Configuration (QUIC) trap. (a) Calibration of the quadrupole current I_{QP} with respect to the position of the atoms x_{atom}. (b) Absorption image of atoms in the decompressed QUIC trap after 3.5 ms TOF. (c) Density profile of the atoms in the X direction. (d) Density profile of the atoms in the Y direction.

the atoms (Fig. 3.2(a)). Both ramps use an exponential form.

The optical sheet, with a final power of 165 mW, is actually a TEM01 mode beam with a dark line at the center. The beam is derived from a 10 W Nd:Vanadate laser (Coherent, Verdi V-10) and focused to a $1/e^2$ radius of 2.4 μm $\times$ 125 μm, at a distance about half cloud size below the atoms. Its focus is aligned with respect to the location of the atoms by minimizing the atom leakage through the sheet while reducing the intensity of the sheet. The circular optical trap, with a final power of 3.3 mW, is a circular Gaussian beam. It is derived from a Ytterbium doped fiber laser (IPG-Photonics, YLC-10-1064) and focused to a $1/e^2$ radius of 50 μm, with the focus slightly above the atoms.

The atomic cloud is further compressed. This is because (1) the atomic density, which is an important factor for the following evaporative cooling, decreases as the trapping potential is relaxed during the transfer, and (2) in order to load more atoms into a 2D trap it is necessarily to "squeeze" the atomic cloud in one direction to obtain a quasi-two-dimensional shape. Therefore, the intensity of the circular optical trap is ramped up exponentially to 30 mW in 500 ms while the earth field compensation field, which is used to lift the atoms above the horizontal sheet, is ramped down linearly. This allows the gravity to press the atoms against the sheet and increase their density but not too strong to pull the atoms through the sheet (Fig. 3.2(b)-(d)). During this compression, the auxiliary coils and the quadrupole current are used again to balance the motion of the atoms.

The high atomic density after the compression gives a good starting point for the evaporative cooling in the optical trap. The evaporative cooling is carried out by reducing the intensity of the circular optical trap and letting highly energetic atoms escape radially through the trap. The intensity of the circular optical trap

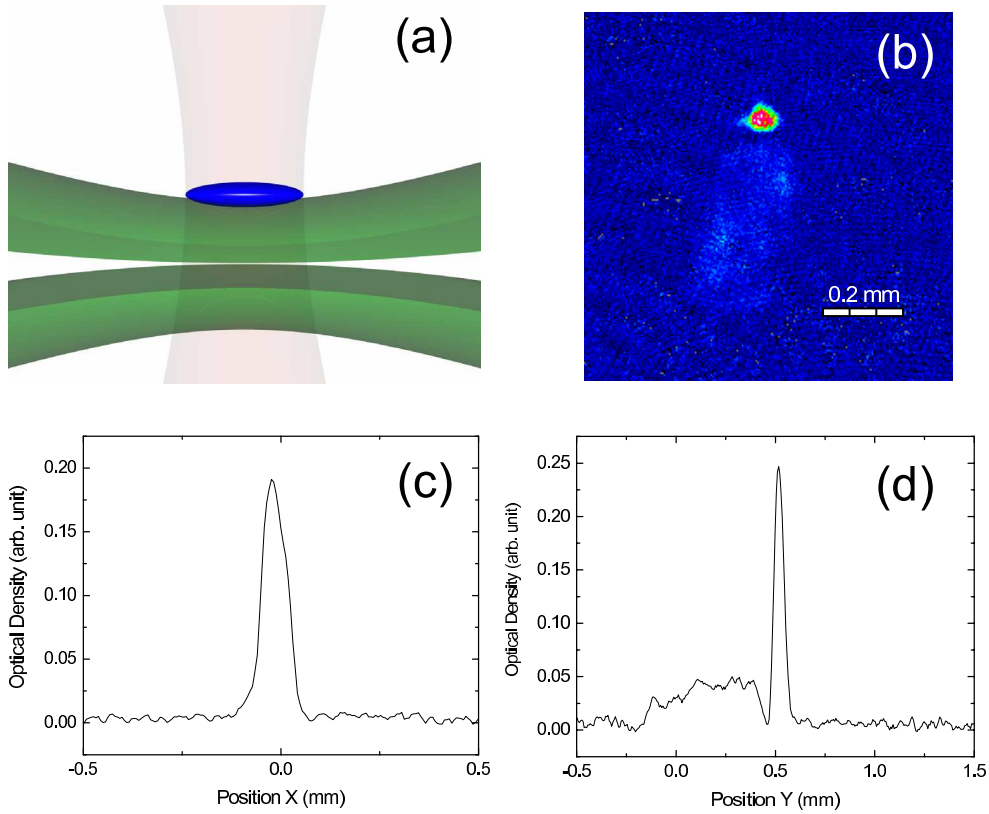

Figure 3.2: Compressed optical trap. (a) Pictorial view of atoms (in blue color) in the compressed optical trap. The horizontal sheet (in green color) holds the atoms against the gravity and the circular optical trap (in red color) surrounds the atoms. (b) Absorption image of atoms in the compressed optical trap after 3.5 ms TOF, where atoms leaking through the horizontal sheet can also be seen. (c) Density profile of the atoms in the X direction. (d) Density profile of the atoms in the Y direction.

is gradually ramped down to 21 mW in five steps which take a total time of one second (Fig. 3.3(a)). In each step, the total current in the magnetic trap is also ramped off linearly as well as the quadrupole current, the bias magnetic field B_0, and the auxiliary coils. The earth compensation fields are not ramped completely off but kept at the values used in the MOT.

At the end of the evaporative cooling, a BEC of 2.4×10^5 atoms is obtained in the gravito-optical trap (Fig. 3.3(b)-(d)), which has a calculated trapping frequencies of $\omega_{rad} = 60$ Hz radially and $\omega_{ax} = 850$ Hz axially. A series of the time-of-flight (TOF) measurements at different expansion time is shown in Fig. 3.3(e). The lifetime in this trap is measured to be about 5 seconds, with a fast exponential decay in the first 500 ms which has a time constant of 180 ms. The fast decay at the beginning is probably due to the three-body collisions or some residual evaporative cooling (Fig. 3.3(f)).

Since the BEC in the gravito-optical trap is surrounded by a circular optical trap which gives a harmonic potential, it has a circular shape in the radial direction. Fig. 3.4(a)-(c) show the top view and the density distributions of the atoms.

It is also interesting, for the research purpose, to confine the atoms by hard walls which produce a flat potential. In order to create such a potential, we use another two pairs of blue-detuned optical sheets propagating vertically to confine the atoms in two orthogonal directions perpendicular to the plane of the horizontal sheet. Both sheet pairs are derived from the same 532 nm laser (10 W) as the horizontal sheet and focused to $1/e^2$ radii of 1.8 μm $\times$ 125 μm and 2.5 μm $\times$ 125 μm at the position of the atoms with power of 3.7 W and 1 W. The trap depth of each sheet pair greatly exceeds the chemical potential of the BEC and therefore forms a two-dimensional hard-wall potential for atoms. A typical image of the BEC

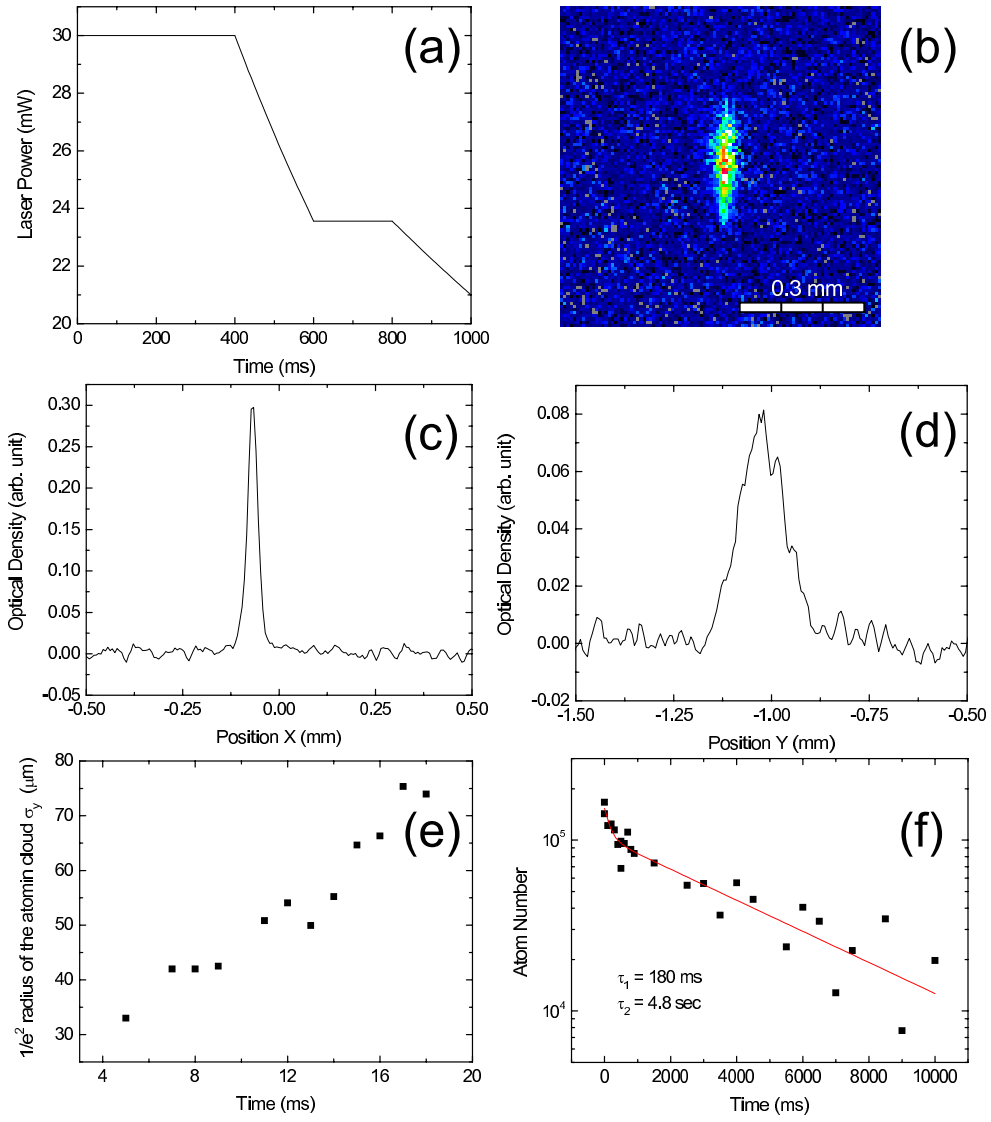

Figure 3.3: Bose-Einstein condensate (BEC) in the grvito-optical trap. (a) Intensity of circular optical trap as a function of time during the evaporative cooling. (b) Absorption image of BEC after 18 ms TOF. (c) Density profile of the atoms in the X direction. (d) Density profile of the atoms in the Y direction. (e) Series of TOF images at different expansion time. (f) Lifetime measurement gives $\tau = 4.8$ seconds with a fast decay of $\tau = 180$ ms at the beginning.

in this trap is shown in Fig. 3.4(d)-(f).

Unfortunately, the trapping frequencies obtained in the gravito-optical trap are still not high enough to fulfill the condition of a two-dimensional BEC (Eq. (3.1)) if we want to have a reasonable amount of atoms.

There are many different ways to create a high trapping frequency trap. For example, one can use (1) an one-dimensional optical lattice, (2) two adjacent blue-detuned (repulsive) optical sheets, or (3) a red-detuned (attractive) red sheet. However, these methods have their own disadvantages: (1) the optical lattice can easily produce very high trapping frequency but also an array of BECs which does not have single site addresability (Fig. 3.5(a)); (2) the configuration of two adjacent optical sheets gives a potential offset which raises as the beam intensity increases and thus limits the trapping frequency if one has limited laser power (Fig. 3.5(b)-(c)); (3) the red sheet is probably the simplest method but the high trap depth makes it inconvenient for evaporative cooling or verifying the existence of a condensate by lowering the trap depth and the scattering rate ($\sim$ heating rate) might also be too high at the trap center (Fig. 3.5(d)). Therefore, the approach we use to produce a two-dimensional BEC is neither of the above.

3.3.3 Resemble TEM_{01} Beam by Phase Mask

We use blue-detuned TEM_{01} beams to produce a high trapping frequency optical trap. A TEM_{01} beam has a completely dark region at the center of the beam. Trapping atoms in the dark region thus reduces the scattering rate and does not have the problem of potential offset, too. To create a TEM_{01} beam, we first pass a Gaussian beam through a homemade phase mask, which imprints a π phase shift between the two halves of the incident beam. The beam is then focused to the

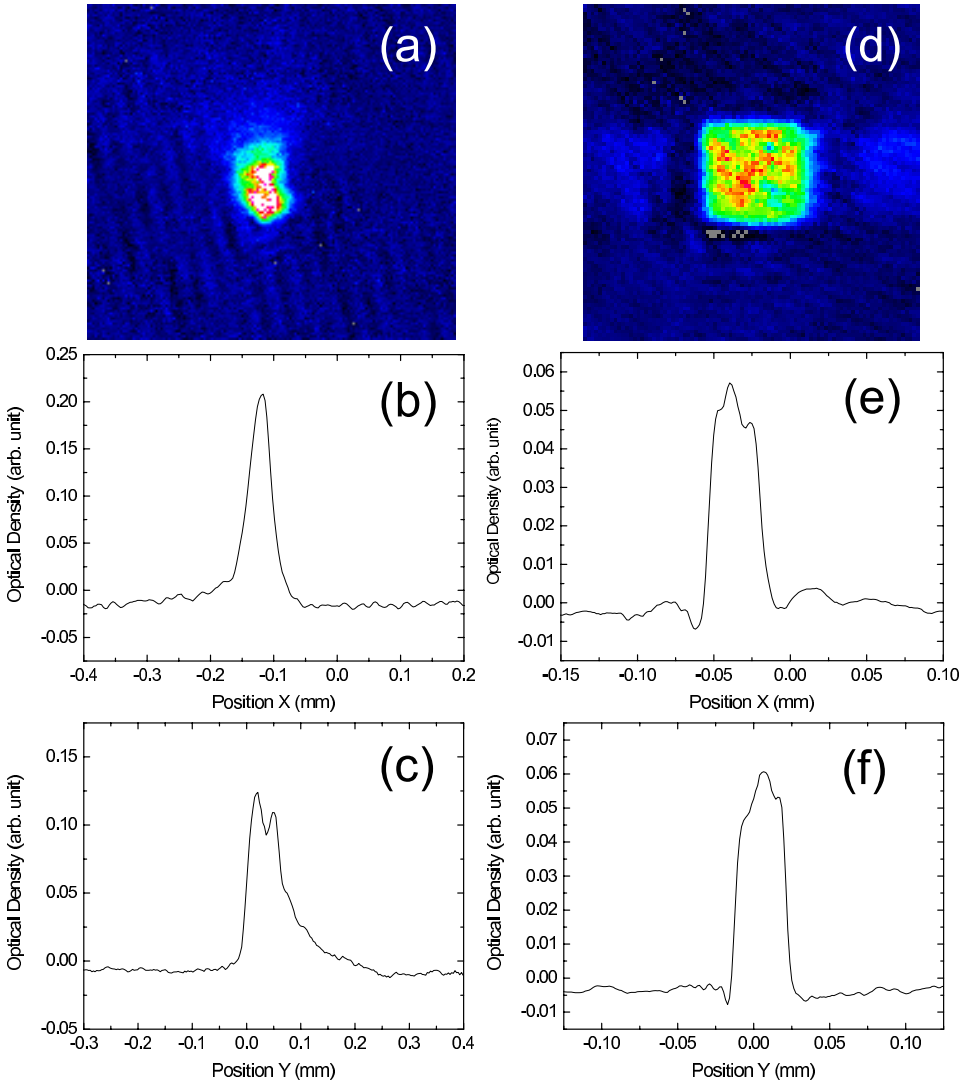

Figure 3.4: Bose-Einstein condensate (BEC) in a square hard-wall trap. (a) BEC in a gravito-optical trap surrounded by a red-detuned circular beam has a circular shape in the radial direction. (b) Density profile of the BEC, shown in (a), in the X direction. (c) Density profile of the BEC, shown in (a), in the Y direction. (d) BEC in a square hard-wall trap shows a square shape. (e) Density profile of the BEC, shown in (d), in the X direction. (f) Density profile of the BEC, shown in (d), in the Y direction.

position of the atoms, which resembles a TEM_{01} beam.

It might not seem to be trivial how the resulting beam becomes TEM_{01} mode. One can understand this by taking the amplitude of the incident beam and calculating its Fourier transform, which is equivalent to the focusing of the lens. The amplitude of the incident beam has the form of a Gaussian, which is given by

$$E_{int} = \begin{cases} \sqrt{\frac{2P}{\pi w_x w_y}} e^{-\frac{x^2}{w_x^2}} e^{-\frac{y^2}{w_y^2}}, & y > 0 \quad \text{(one half)} \\ e^{-i\pi} \sqrt{\frac{2P}{\pi w_x w_y}} e^{-\frac{x^2}{w_x^2}} e^{-\frac{y^2}{w_y^2}}, & y < 0 \quad \text{(the other half)} \end{cases}, \tag{3.10}$$

where P is the beam power and w_i is the $1/e^2$ radius in the i direction. By Fourier transforming E_{int} to $\tilde{E}$, the intensity distribution $\tilde{I} = \left|\tilde{E}\right|^2$ near the focus can be found to be (neglecting z^3 and higher terms)

$$\tilde{I} = \frac{I_{TEM_{01}}}{\pi} = \frac{8P}{\pi^2 w_x w_y^3} y^2 e^{-\frac{2x^2}{w_x^2}} e^{-\frac{2y^2}{w_y^2}}, \tag{3.11}$$

which resembles that of the true TEM_{01} beam with a factor of π smaller.

The phase mask or phase plate is manufactured as follows: first, we cover half of a poor-quality BK7 optical glass (Esco Products, P910250) with Teflon tape (Fig. 3.6(a)). The optical glass, as well as a sensor sitting next to it, is placed in a chamber with a background pressure of 3.0×10^{-6} torr (Fig. 3.6(b)). About ten inches below them, there is magnesium fluoride (Johnson Matthey Catalog Company, 99.9% MgF_2) placed on a plate which has high current ($\sim$ 150 A) passing through it. Once the plate is heated to high enough temperature by the high current, the magnesium fluoride starts to evaporate and deposit on the optical glass and the sensor. The sensor detects the current flowing through the deposited material and stops the process when the thickness of the deposition is the right amount. The

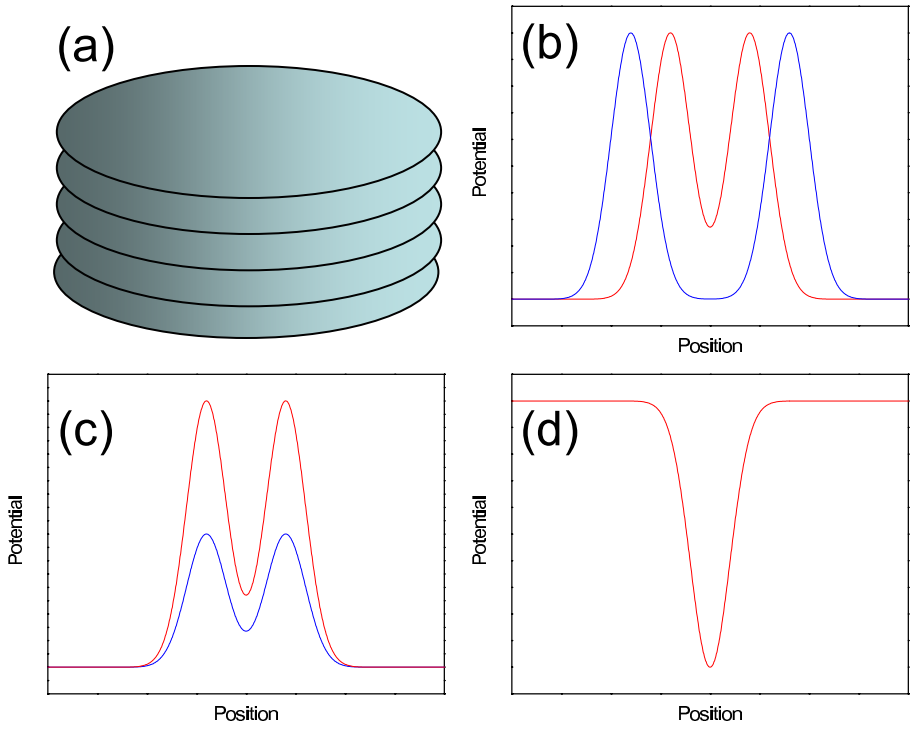

Figure 3.5: Different methods of producing two-dimensional Bose-Einstein condensates (BEC). (a) In a one-dimensional (2D) optical lattice, an array of 2D BECs does not have single site addressability. (b) When two adjacent optical sheets approach each other, a potential offset exists. The potential in red color has a smaller separation between two sheets than the potential in blue color. (c) Increase the beam intensity also raise the potential offset. The potential in red color has higher beam intensity than the potential in blue color. (d) Density profile of the atoms in the Y direction.

thickness is chosen such that the laser beam passing through will be imprinted with a π phase shift, that is, when the following condition is fulfilled:

$$\frac{(n-1)t}{\lambda} = \pi, \tag{3.12}$$

where n is the index of refraction of magnesium fluoride, t is the thickness, and λ is the wavelength of the beam. A finished phase mask is shown in (Fig. 3.6(c)).

Although the glass plate we use does not have a high optical quality and the deposition process is not very precisely controlled, the result of the phase mask turns out to be surprisingly good. Fig. 3.6(d) shows a photo of the TEM_{01}-like beam produced by our phase mask. The intensity distribution is fit to a true TEM_{01} profile very well (Fig. 3.6(e)).

3.3.4 Observation of Two-Dimensional Bose-Einstein Condensate

After having a BEC of 2.4×10^5 atoms on a horizontal sheet surrounded by a circular optical trap, we load the BEC into a two-dimensional (2D) TEM_{01} optical trap. This is accomplished in two steps. A horizontal TEM_{01} optical sheet is first ramped on at a position 4 μm above the first sheet where the atoms are located. The ramp takes 100 ms and uses an exponential form with a final beam power of 165 mW. Both of the sheets are produced from the same acousto-optic modulator (AOM) with different input RF frequencies, and thus have the same beam properties. The position of the second sheet is optimized for maximum loading rate.

After the ramp, the beam power of the second TEM_{01} sheet is further increased to 1 W in another 100 ms while the first horizontal sheet, which does not hold the atoms anymore, is ramped off. The atoms originally in the gravito-optical trap are thus transfered into the 2D TEM_{01} trap. The transfer efficiency is measured

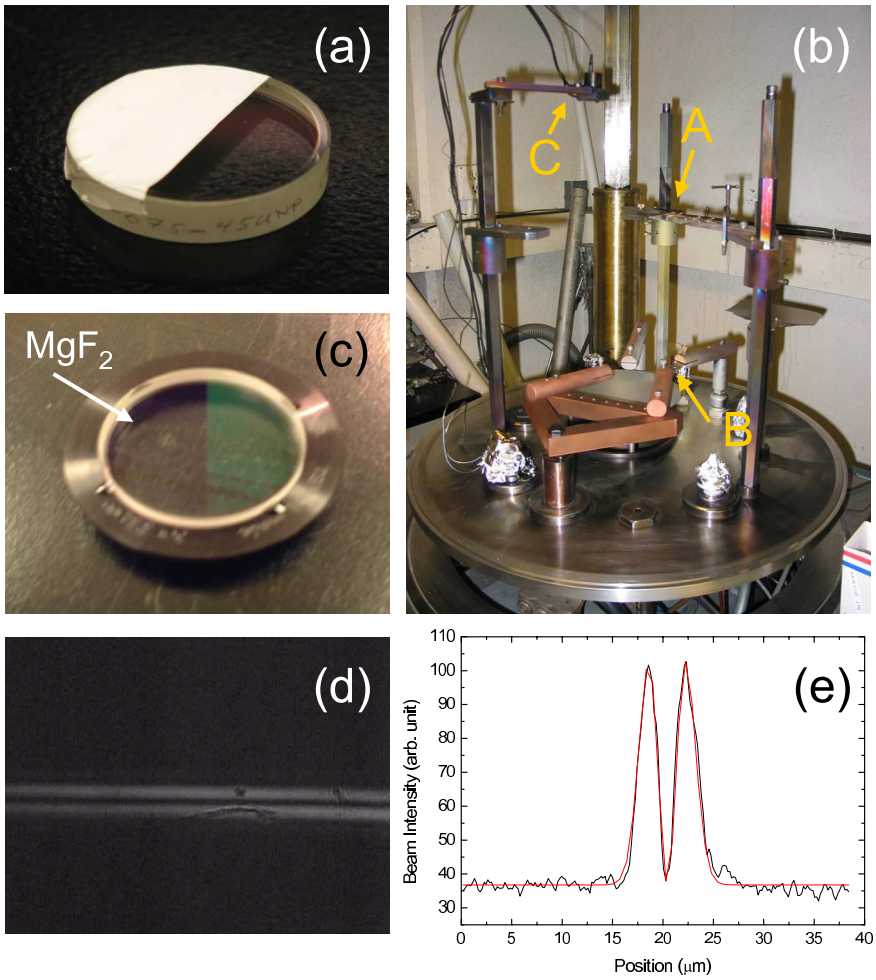

Figure 3.6: Manufacture and property of TEM_{01} phase mask. (a) An optical glass is covered by Teflon tape on one half in order to be deposited on the other half. (b) The optical glass (A) is placed inside a chamber for deposition. Magnesium fluoride (MgF_2) is stored on a plate (B) where high current passes through. A sensor (C) detects the current passing through the deposited material to determine the correct deposition thickness. (c) A finished TEM_{01} phase mask with half of the plate coated with MgF_2. (d) Intensity profile of the TEM_{01} beam produced by the phase mask (black). A fit of true TEM_{01} profile is also shown (red).

to be nearly 100%. A pictorial view of the atoms in the 2D TEM_{01} trap is shown in Fig. 3.7(a). Fig. 3.7(c) shows an absorption image of the two-dimensional BEC after 18 ms time-of-flight (TOF) with the density profiles shown in Fig. 3.7(d)-(e). A series of TOF measurements is shown in Fig. 3.7(f). The trapping frequency in the tight confining direction is calculated to be $\omega_t = 27$ kHz.

The trapping frequency of the 2D TEM_{01} trap is strongly dependent on the alignment of the beam. This is likely due to any misalignment or the inhomogeneity of the phase mask. However, a careful adjustment of the position or the orientation of the phase mask and the relative position of the beam to the atoms always allow one to achieve high trapping frequency in this trap. In order to have a full control of the angle and position of the phase mask, we mount the phase mask on both a rotational stage and a translational stage (Fig. 3.7(b)). Moreover, a mirror, which is placed after the phase mask and about 3 m away from the atoms, is installed with micrometer screws (New Focus, 9351) for fine adjustment of the beam position.

3.3.5 Observation of One-Dimensional Bose-Einstein Condensate

In order to obtain a one-dimensional Bose-Einstein condensate (BEC), we need to transform the trap geometry into a cigar shape. This can be accomplished by loading the atoms into another TEM_{01} beam which then forms a crossed TEM_{01} trap with the first (horizontal) TEM_{01} beam. A pictorial view of this configuration is shown in Fig. 3.8(a). However, in order to load the atoms into the crossed trap, we need to use another beam to compress the atoms in one of the directions perpendicular to gravity. This is because, in the two-dimensional trap, gravity helps to press the atoms onto the horizontal sheet so that the atoms can be easily loaded into the dark region of the TEM_{01} beam, but this is not the case in the other directions.

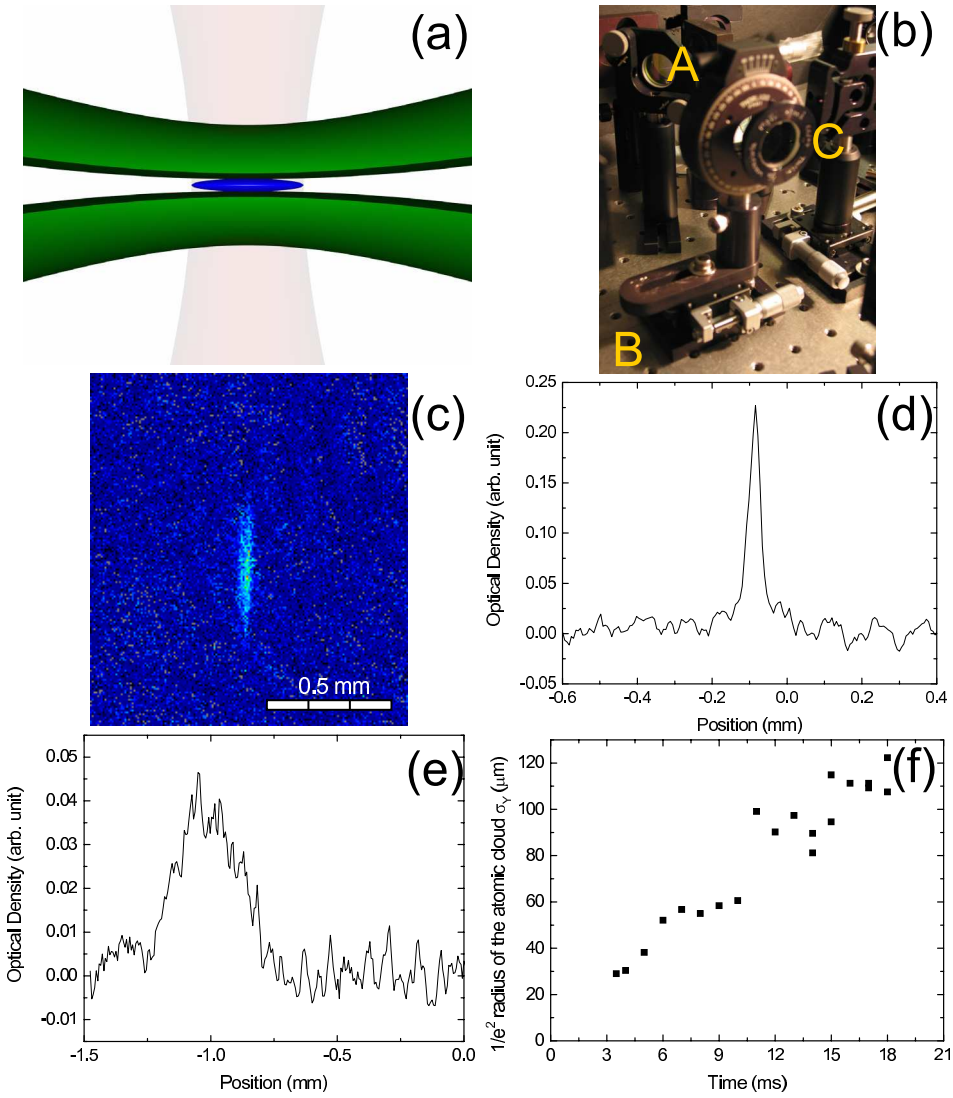

Figure 3.7: Observation of two-dimensional Bose-Einstein condensate in a TEM_{01} optical trap. (a) Pictorial shows the atoms in the TEM_{01} trap. (b) The phase mask (C) is mounted on a rotational (A) and a translational stage to have a full control of the angle and position. (c) Absorption image of two-dimensional BEC after 18 ms TOF. (d) Density profile of the atoms in the X direction. (e) Density profile of the atoms in the Y direction. (f) Series of TOF images at different expansion time.

The compression is carried out by ramping on a red-detuned elliptic optical trap to 85 mW, which is orthogonal to the horizontal sheet. The ramp takes 100 ms and has an exponential shape. The elliptic optical trap is derived from the same 1064 nm laser (10 W) as the circular optical trap and focused to a $1/e^2$ radius of 10 μm $\times$ 125 μm at the position of the atoms. Due to the anisotropic nature of the elliptic beam, the atoms in the combined optical trap have a cigar shape (Fig. 3.8(b)).

After ramping on the elliptic beam, a pair of blue-detuned optical sheets, which is orthogonal to both of the horizontal TEM_{01} and elliptic sheets, is ramped on in 100 ms with a separation similar to the size of the atoms in the elongated direction (80 μm). This sheet pair thus forms an "end cap" for the atoms. The intensity ramp of the beam also takes an exponential form. Like the other blue-detuned beams, the "end cap" pair is derived from the same 532 nm laser but focused to a $1/e^2$ radius of 2.5 μm $\times$ 6 μm at the location of the atoms. The purpose of these "end cap" beams is to provide confinement in the third direction not covered by the TEM_{01} beams.

Once the "end cap" beams are ramped on, the circular optical trap is no longer required. Therefore, the circular optical trap is ramped off exponentially in 100 ms while the second TEM_{01} beam, propagating along the direction of the gravity, is ramped on to 740 mW. This vertical TEM_{01} beam is also derived from the same 532 nm laser as the other blue-detuned beams and focused to a $1/e^2$ radius of 1.8 μm $\times$ 125 μm. The vertical TEM_{01} beam has a tighter focus than the horizontal TEM_{01} beam. This is because the last lens (Newport, GAC040) in the vertical TEM_{01} beam path has a better optical quality ($f/\# = 2.0$) than the lens (Melles Griot, 01LAO459) in the horizontal TEM_{01} beam path ($f/\# = 3.1$). The calculated trapping frequency of the vertical TEM_{01} beam in the tightly confining

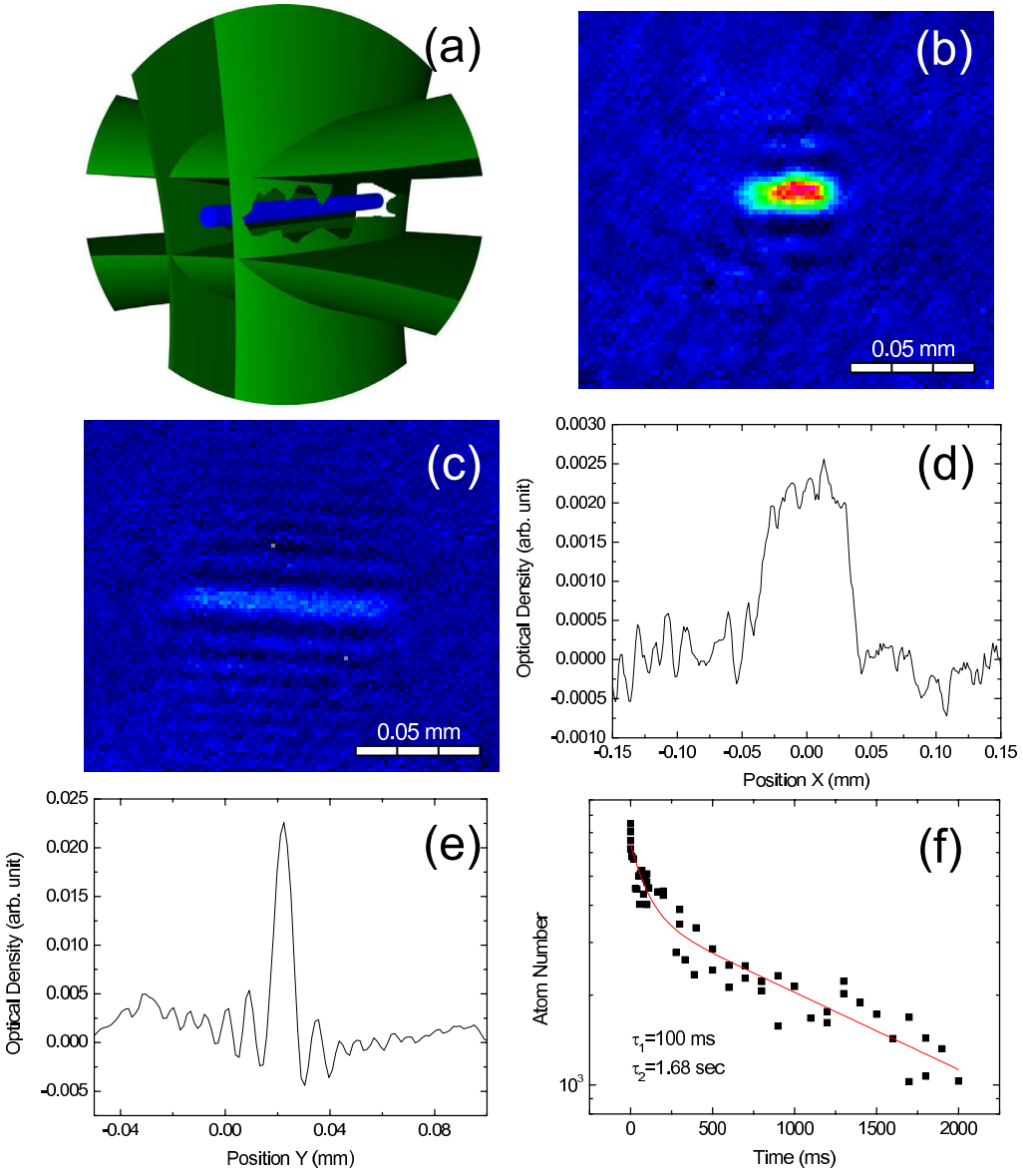

Figure 3.8: Observation of one-dimensional Bose-Einstein condensate in a crossed TEM_{01} trap. (a) Pictorial shows the atoms in the crossed TEM_{01} trap. (b) Absorption image of the atoms confined by the elliptic optical trap. (c) Absorption image of one-dimensional BEC. (d) Density profile of the atoms in the X direction. (e) Density profile of the atoms in the Y direction. (f) Lifetime measurement shows two different time scales.

direction is thus also higher: $\omega_t = 2\pi$ 60 kHz.

Since the atoms are already successfully loaded into the vertical TEM_{01} beam, the elliptic beam is ramped off exponentially in the next 100 ms. The process of obtaining a one-dimensional BEC is then completed by ramping the vertical TEM_{01} beam exponentially to the full power in 100 ms, which is 3.7 W. An absorption image of an one-dimensional BEC of 3100 atoms produced in the crossed TEM_{01} optical trap is shown in Fig. 3.8(c) with the density profiles given in Fig. 3.8(d)-(e). The lifetime measurement of the one-dimensional BEC in the crossed TEM_{01} trap gives about 2 seconds as shown in Fig. 3.8(f), where a fast exponential decay with a time constant of 100 ms exists in the first 250 ms.

A TOF image in the crossed TEM_{01} optical trap does not give a resolvable signal because of the low atom number ($\sim$ 3000) and fast expansion due to the strong confinements. Therefore, for TOF images in the crossed TEM_{01} trap, we always leave the horizontal TEM_{01} sheet on while release the atoms from the vertical TEM_{01}. This allows the atoms freely expand in a two-dimensional plane confined by the horizontal TEM_{01} sheet. Fig. 3.9(c) shows a series of TOF measurements for different expansion time in the crossed trap. A typical TOF image is shown in Fig. 3.9(b).

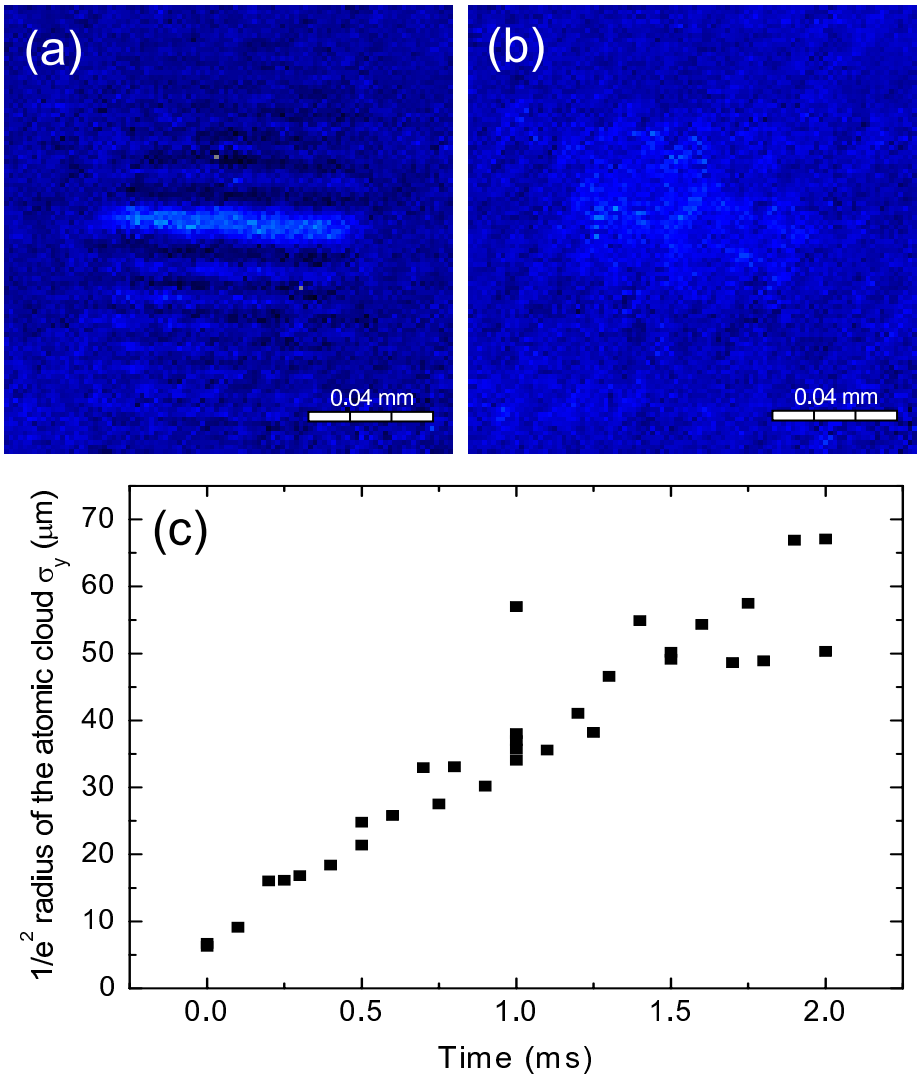

Figure 3.9: Expansion of one-dimensional Bose-Einstein condensate (BEC) in a TEM_{01} sheet. (a) Absorption image of one-dimensional BEC in a crossed TEM_{01} optical trap. (b) Absorption image of the BEC after 1 ms time-of-flight (TOF) in a TEM_{01} sheet.

Chapter 4

Sub-Poissonian Number Statistics in a Degenerate Bose Gas

This chapter describes the optical box trap we use to study atom number statistics in a degenerate Bose gas, the experimental result of sub-Poissonian number statistics, and a simple theoretical model for a degenerate Bose gas in a finite-height potential well.

4.1 Number Squeezed State

A Bose-Einstein condensate (BEC) can be described by a macroscopic wave function, $\psi(r) = \sqrt{n(r)}\, e^{i\phi}$, where density $n(r)$ and phase ϕ are connected by a Heinsenberg uncertainty relation in the same way as position and momentum. In terms of atom number N and phase ϕ, the fluctuations in these two quadratures then obey the

relation $\Delta N \Delta\phi \cong 1$, where ΔN in most experiments is on the order of $\sqrt{N}$, a "standard quantum limit" for the number fluctuation. Therefore, a non-classical state in a BEC is a configuration of atoms whose fluctuation in one quadrature is reduced while the fluctuation in the other quadrature increases. For example, a number squeezed state has a ΔN smaller than $\sqrt{N}$ with a complementary increase in ϕ.

Number squeezed states have importance in many aspects of physics. For example, the creation of many-body atomic number states would be a building block for controlled manipulation of entangled states of N-particle systems [37, 38], which are fundamental to the study of quantum mechanics and can provide the basis of quantum information processing or quantum computation [39].

Moreover, number squeezed states could lead to a pronounced improvement in the sensitivity of precision measurements. Atom interferometry [40] is one example. The accuracy of atom-interferometer-based gyroscopes, gravimeters, and gravity gradiometers are mainly limited by the atom shot noise. The sensitivity thus scales with $1/\sqrt{N}$, where N is the number of atoms used in the measurement. However, by taking advantage of the property of number squeezed states, one could potentially reach the sensitivity of Heinsenberg limit which is $1/N$ [41].

With the aid of nonlinear atom-atom interaction, several groups have claimed to obtain non-classical states with reduced number fluctuations in a degenerate Bose gas trapped in an optical trap [42] or on an atom chip [43, 44]. In both experiments, phase fluctuations were measured to be larger compared to that of a coherent state and thus reduction of the number fluctuation (number squeezing) were inferred. However, in order to further claim the observation of a number squeezed state in these experiments, one would also need to measure the corresponding fluctuation in

the conjugate variable (i.e. the phase) or perform phase coherence measurements [45, 46, 47]. Nevertheless, these results are already a big step toward the manipulation of squeezed states in atomic physics.

4.2 The Idea of Creating a Number Squeezed State

As most people would notice when they walk by a utility pole with some birds on it, the most amazing thing is not just that the birds can handle the high voltage passing through the wire but also that there seems to a minimum distance between any adjoining bird (Fig. 4.1 (a)). This minimum distance is known as the "individual distance" - an intolerance for members of their own species to be within a certain distance. The similar phenomena could also be observed when people are standing inside a elevator - everyone keeps a minimum "comfortable distance" from each other.

Now, consider the following question: assuming the length of the wire is fixed and there are infinite amount of birds, what would be the maximum number of birds that can stay on this wire? The answer apparently is the length of the wire divided by the "individual distance" plus 1. Moreover, if we perform such an "experiment," this maximum number probably will not change much from "shot to shot." Our idea of creating a number squeezed state is actually very similar to this natural phenomenon.

To demonstrate the idea, let's imagine someone is repeatedly pouring some billiard balls into an one-dimensional box (Fig. 4.1 (b)). He or she will probably find out very soon that the number of billiard balls in this box every time is completely random. This is just because the "pouring" is an uncontrolled process. However, if he or she always over-fills up the box with billiard balls, the number of billiard

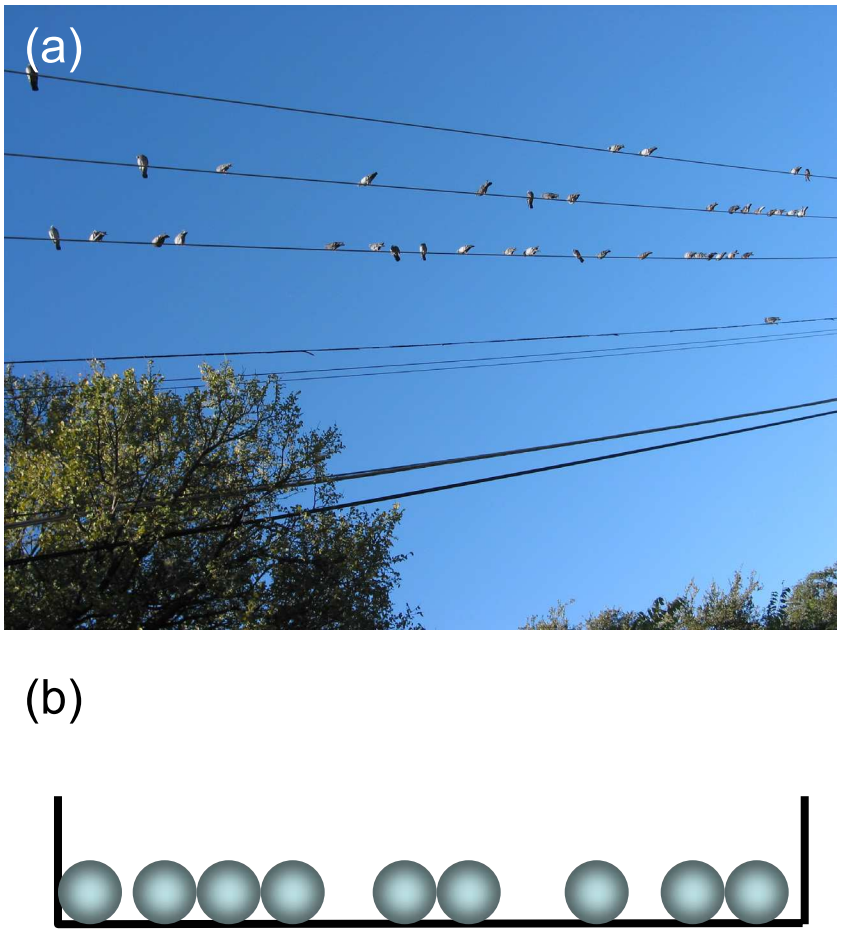

Figure 4.1: Assuming the length of a wire is fixed, what would be the number of birds on this wire? (a) Each bird on the wire stands a minimum distance, known as "individual distance," from the adjoining bird. (b) The same idea could be applied to precisely control the atom number in an one-dimensional box.

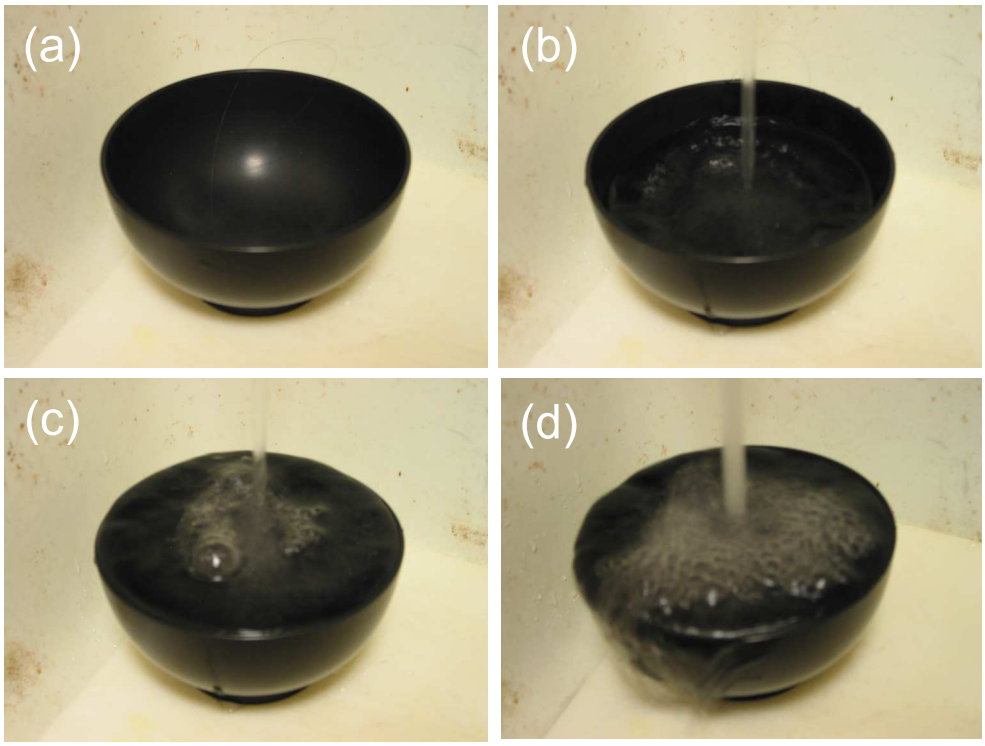

Figure 4.2: Illustration of controlling the volume of water in a bowl. (a) Start with an empty bowl under a water faucet, (b) it is difficult to control the amount of water to be the same every time, even though you try to stop the water flow at the same level every time. (c) However, once the bowl is filled up, (d) the amount of water left inside the bowl will always stay the same.

balls in the box is very likely to be the same every time - because the maximum number of billiard balls allowed in this box is the same, which is determined by the size of the billiard ball. In our experiment, the billiard balls are interacting atoms. Therefore, the interaction determines how many atoms can be "poured" into the "box."

This atomic analog of "birds on a wire" can be best illustrated by the example shown in Fig. 4.2. Suppose you try to pour the same amount of water in a bowl, which is placed under a flowing water faucet, every time (Fig. 4.2 (a)). Since the

bowl can be filled to an arbitrary level while the volume of water does not exceed that of the bowl (Fig. 4.2 (b)), it is really difficult to control the amount of water in the bowl even though you are careful to stop the water flow at the same level every time. However, once the bowl is filled up with water (Fig. 4.2 (c)), the water inside will always be the same whenever you switch off the faucet (Fig. 4.2 (d)).

In our experiment, we are able to control the volume of the bowl or the "optical box." Therefore, at the beginning of the experiment, we always load a random number of atoms into an huge "optical box" which can hold all the atoms. Then, we gradually reduce the height of the "optical box" until we see some atoms leaking out. Once the atoms start leaking out, a one-to-one correspondence will exist between the atom number in the "optical box" and the height of the "optical box." We can then vary the height of the box to obtain the desired atom number. To measure the atom number inside the "optical box," the height is always raised up again to protect the atoms from escaping during the measurement. The experimental sequence is illustrated in Fig. 4.3 where the "optical box" is shown as a finite-height potential well.

4.3 A Simple Theoretical Model

A simple theoretical model has been developed by Dudarev *et al.* [48] to verify the idea of reducing atom number fluctuation described in the previous section. Using this model, the dependence of the maximum atom number on the potential parameters and interaction strength is obtained. Although the model considers only one dimensional bosons with contact interaction in a square well, it shows the essential features of the idea. In that paper, the authors also calculate the strong interacting case (impenetrable bosons). However, since the experimental condition

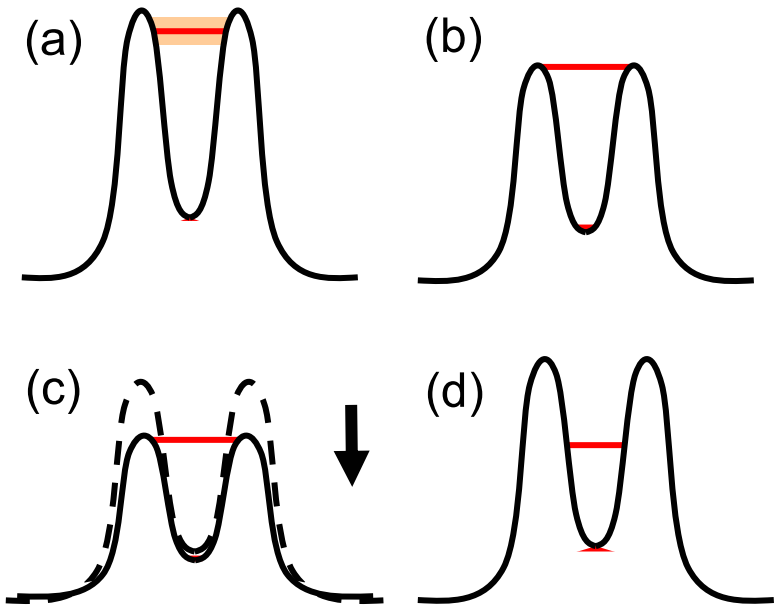

Figure 4.3: Experimental sequence of preparing sub-Poissonian number statistics in a degenerate Bose gas. (a) A random number of atoms is first loaded into a finite-height potential well. The red line represents the level of the chemical potential which is related to the atom number. The orange region shows the initial fluctuation. (b) The height of the potential well is then lowered to a level where atoms start to leak out. From this point on, a one-to-one correspondence between the atom number and the well depth is established. (c) The well depth can be varied to obtain the desire atom number. (d) Before the imaging, the well is raised again for protection purpose.

is far from that regime, we will only discuss the case when the average interaction energy of each particle is smaller than the average kinetic energy - that is, the weak interaction limit. Nevertheless, it will still be interesting to perform similar experiments in the regime of impenetrable bosons.

In the limit of weak interaction, the problem of N deeply bound bosons in a potential well is always solved by Gross-Pitaevskii (GP) equation, which assumes all N particles are in the same single particle state. The wavefunction of each particle can then be determined by the variational method. However, this method will not work very well in our case because of the fact that one particle (which is about to leak out) always becomes weakly bound while all the others remain tightly bound. As pointed out in Ref. [48], this situation is better described by a Hartree-Fock wavefunction [49, 50] with $N-1$ particles in a state ϕ_1 and one particle (which will leak out) in another state ϕ_2. In order to minimize the total energy and maintain the symmetric and nodeless properties of N-body wave function, both of ϕ_1 and ϕ_2 should be symmetric and nodeless although they do not have to be orthogonal to each other.

Fig. 4.4 shows a comparison between the two methods. The solid lines show the values of the variational parameters κ_i, which minimize the total energy for three atoms in a potential well, as a function of the well depth V_0 using variational functions of the form

$$\phi_i = \sqrt{\kappa_i}\, e^{-\kappa_i |x|} \ (i = 1, 2) \ . \tag{4.1}$$

The dotted line is the result when only one variational wave function is used and thus eqivalent to solving the GP equation. The interaction strength used in this particular calculation is $g_{1D} = 2\hbar^2 a_s / m a_\perp^2 = \hbar^2 / mL$, where $\hbar$ is the Planck constant h divided

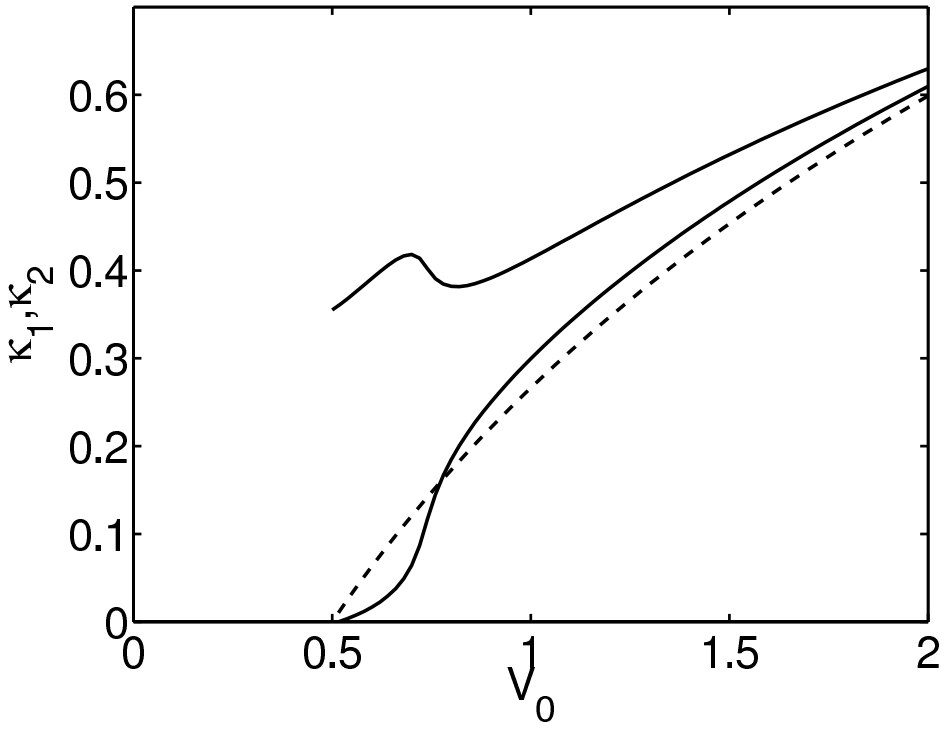

Figure 4.4: Variational parameters, κ_1 and κ_2, that minimize the total energy of three atoms in a well for different well depths V_0. The units of V_0 and the interaction strength g are $(\hbar/L)^2/m$ and $\hbar^2/mL$, respectively. In this calculation, g is chosen to be 1. Plots courtesy of Artëm Dudarev [48].

by 2π, a_s the s-wave scattering length, m the mass, $a_\perp$ the width of the transverse wave function, and L the width of the potential. In the case of a deep well (for example, $V_0 \sim 2$), the values of κ_1 and κ_2 are very close, indicating a condensate state. As the well depth decreases, the particle that occupies ϕ_2 becomes more and more likely to escape, therefore κ_2 finally goes to zero when the well cannot support three atoms anymore ($V_0 \sim 0.5$).

4.3.1 Large Atom Number Limit

If the number of particles considered is large or $Ng_{1D} \gg 1/L$, a relation between the maximum atom number N and the well depth V_0 could be written down analytically by using the Thomas-Fermi approximation. By minimizing the energy functional $E \equiv \langle \psi | H | \psi \rangle$, where $\psi = \phi_1(\vec{r}_1)\phi_1(\vec{r}_2)\cdots\phi_1(\vec{r}_{N-1})\phi_2(\vec{r}_N)$ and $H = h(x) + E_{int}$ with $h(x)$ being the single particle Hamiltonian and E_{int} the interaction energy, two coupled nonlinear equations are obtained

$$\left(h(x) + g(N-2)\left|\phi_1\right|^2 + 2g\left|\phi_2\right|^2\right)\phi_1 = \mu_1\phi_1 \,, \tag{4.2}$$

$$\left(h(x) + 2g(N-1)\left|\phi_1\right|^2\right)\phi_2 = \mu_2\phi_2 \,. \tag{4.3}$$

Neglecting the kinetic energy and the nonlinear term with ϕ_2 (i.e. when ϕ_2 is almost delocalized) in Eq. (4.2), we can obtain a Thomas-Fermi expression for ϕ_1. Then Eq. (4.3) becomes a single particle equation for ϕ_2 with an effective potential contributed from the other atoms. Since the atom will escape if the depth of the effective well becomes zero, the potential well can support N atoms when

$$V_0 > 2g(N-1)/L. \tag{4.4}$$

Note that the point where potential energy is equal to zero is chosen to be at the top of the well.

4.3.2 Small Atom Number Limit

In the limit of small atom number, we can diagonalize the many-body Hamiltonian directly. The Hamiltonian $\hat{H}$ contains two parts, the single particle term $\hat{H}_{sp}$ and the interaction term $\hat{H}_{int}$,

$$\hat{H} = \hat{H}_{sp} + \hat{H}_{int} \ , \tag{4.5}$$

We can express $\hat{H}_{sp}$ in the second quantization form as

$$\hat{H}_{sp} = \sum_j E_j \hat{n}_j \ , \tag{4.6}$$

where E_j is the energy of the jth single particle state which has N_j atoms, and $\hat{n}_j$ is the number operator. The N particle basis is chosen to be the states $\psi_j(x)$ in an infinite well ($D \gg L$, D being the height of the well) which has either an odd or even wavefunction, $\sin(kx)$ or $\cos(kx)$, inside the well and a wavefunction of the form $e^{\pm\kappa x}$ outside the well with $\kappa = \sqrt{k^2 - 2V_0}$ so that the wave function is continuous.

The interaction term $\hat{H}_{int}$ can be written as

$$\hat{H}_{int} = \frac{1}{2} \sum_{j_1,j_2,j_3,j4} \hat{a}^\dagger_{j_1} \hat{a}^\dagger_{j_2} \hat{a}_{j_3} \hat{a}_{j_4} \langle j_1 j_2 \left| U \right| j_3 j_4 \rangle \ , \tag{4.7}$$

where $\hat{a}^\dagger$, $\hat{a}$ are the creation, annihilation operators respectively, and

$$\langle j_1 j_2 \left| U \right| j_3 j_4 \rangle = \int dx \psi^*_{j_1} \psi^*_{j_2} \psi_{j_3} \psi_{j_4} \ . \tag{4.8}$$

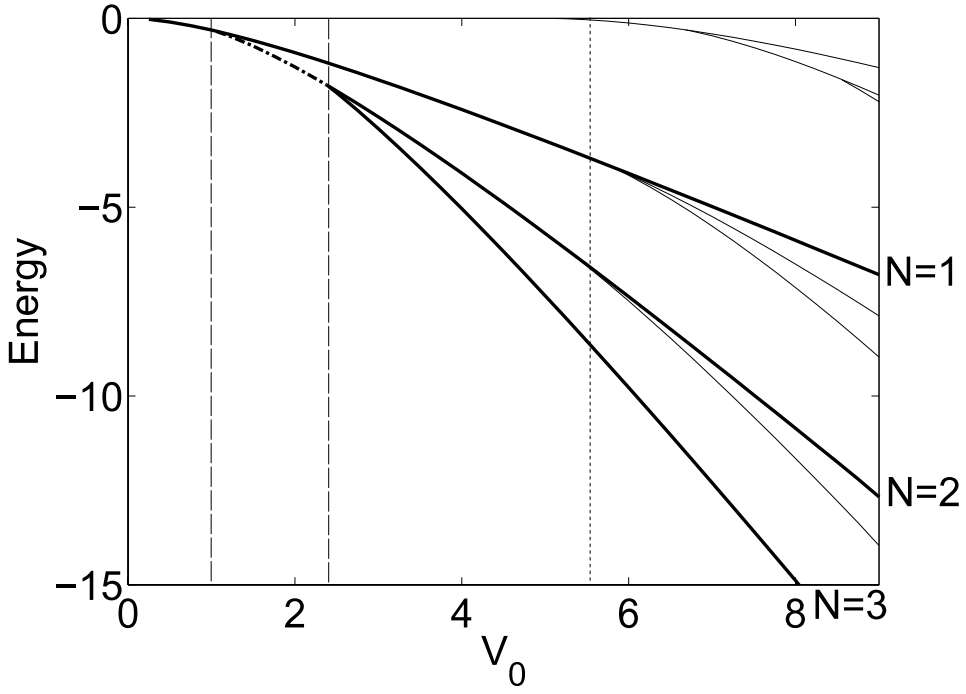

Figure 4.5: Bound states for 1, 2, and 3 atoms in a well found by diagonalizing the Hamiltonian in the limit of small atom number. The interaction strength used in this calculation is $g = 1$, in units of $\hbar^2/mL$. The thin curves are the bound excitations. The dashed-dotted curve between the two vertical dashed lines corresponds to a stable state for 1 or 2 atoms but not for 3 atoms. Well depths larger than the value indicated by the vertical dotted line will have bound excited states for 3 atoms. Plots courtesy of Artëm Dudarev [48].

Fig. 4.5 shows the bound states for 1, 2, and 3 atoms in a well found by diagonalizing the Hamiltonian in Eq. (4.5).

An alternative approach, the Diffusion Monte Carlo approach [51], has also been used by the authors of [48] to calculate the bound levels in the limit of small atom number. Although the finite evolution time and the finite size effect cause some errors in the calculation, the result is still in good agreement with that obtained by diagonalizing the Hamiltonian. Fig. 4.6 shows different regimes that have bound states of 1, 2, 3, 4, and $N \geq 5$ atoms found by the Diffusion Monte Carlo approach. As shown by the red dashed line, the transition from 4 atoms to 5 atoms is already close to what is obtained from the Thomas-Fermi approximation, as given in Eq (4.4).

4.3.3 Excitations

Two types of excitations would occur in our system: one that does not change the atom number in the well (type I) and one that changes the atom number (type II).

To demonstrate this in more detail, let's consider the bound excitations for a three-atom system. In Fig. 4.5, every thin curve between any two adjoining thick curves corresponds to a bound excited state, and has the same atom number as the ground state represented by the first thick curve below it. The first type of excitation (type I) thus corresponds to the transitions from one thick curve to any thin curve which are above it and below the next thick curve. Therefore, the total atom number remains the same in this case. The second type of excitation (type II) corresponds to the transitions from one thick curve to another thick curve and thus changes the total atom number.

In order to avoid these excitations, the process of reducing the well depth

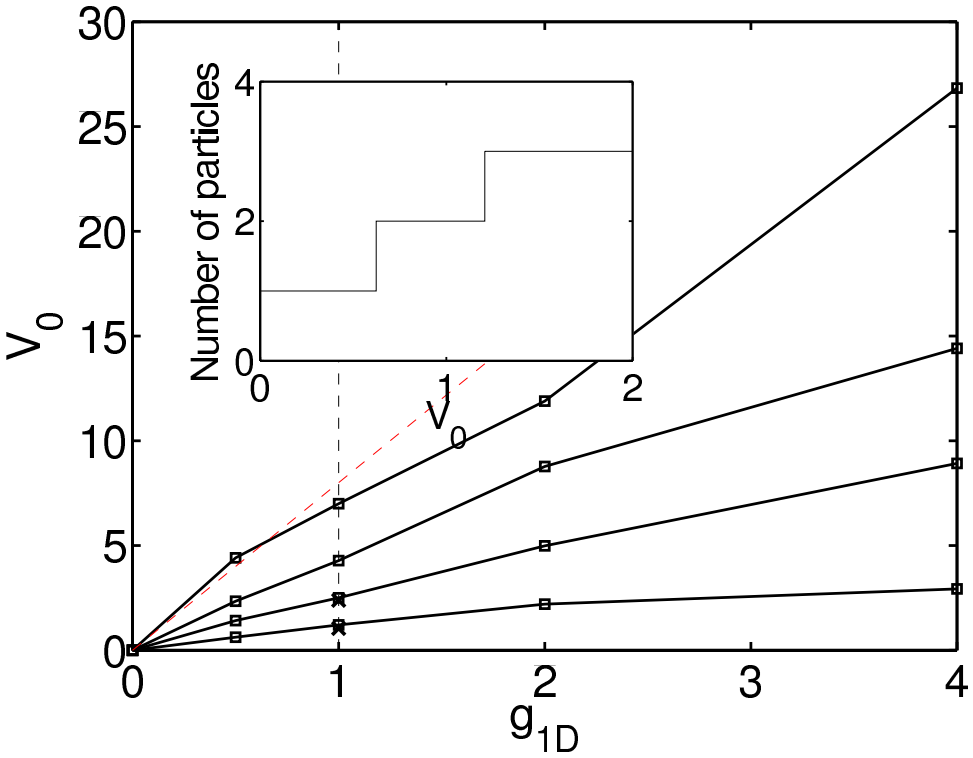

Figure 4.6: Different potential-parameter regimes that have bound states for 1, 2, 3, 4, and $N \geq 5$ atoms. The result is obtained by using the diffusion Monte Carlo approach as explained in [51]. The size of the square dots shows the estimated error caused by the finite evolution time and the finite size effect. The inset shows the allowed atom number for interaction strength $g = 1$ as indicated by the vertical dashed line. The red dashed line represents the transition from 4 to 5 atoms calculated by using Thomas-Fermi approximation. Plots courtesy of Artëm Dudarev [48].

has to be sufficiently slow such that neither type I nor type II will be excited. $t_{gap} = \hbar/E_{gap}$ thus gives us a good estimation of the time scale during which the system could be excited to the next bound state.

To calculate E_{gap}, let's assume the time dependence of the potential to be $V(t) = V_0 e^{-t/\tau}$, which is exactly the form used in our experiment, and the atom number $N \propto V(t)^{\alpha}$ with α on the order of 1. For the purpose of estimation, we will use the GP equation.

In the case of type I excitation, the excitation energy gap can be calculated from the the energy of Bogoliubov excitation of the longest wavelength $\omega_{ext} = E_{gap}/\hbar = \sqrt{\bar{\rho}U_0/m}\ \pi/\hbar L$ [2], where $\bar{\rho}$ is the 3D average density. The time scale is therefore $t_{gap} = \hbar^2 L/\sqrt{\bar{\rho}U_0/m}$.

In the case of type II excitation, E_{gap} is the energy difference between the N- and $(N-1)$-atom states when one atom just escapes from the well. For the process to be adiabatic, the change of the potential ΔV during $t_{gap} = \hbar/E_{gap}$ has to be smaller than the difference of well depths supporting $N+1$ and N atoms, $V_{0,N+1} - V_{0,N}$. We can then estimate the maximum rate of adiabatically reducing the well depth, $r = V_0^{'}$, from

$$\Delta V = r_{max} t_{gap} = r_{max}(\frac{\hbar}{E_{gap}}) \ll V_{0,N+1} - V_{0,N}\ . \tag{4.9}$$

For large atom number, as one atom leaves the well, the total energy of the remaining $N-1$ atom is $E_{N-1} = (N-1)(N-2)g/L - V_0(N-1)$. The excitation energy gap is then given by the difference between the energy of the $(N-1)$-atom state and the $(N-2)$-atom state, $E_{gap} = E_{N-1} - E_{N-2} \propto Ng/L$, if we keep only the first order terms (proportional to N). From Eq. (4.4), $V_{0,N+1} - V_{0,N}$ can be calculated to be $2g/L$. The maximum rate r_{max} is therefore proportional to $g^2 N$,

which indicates the difficulty of maintaining the adiabatic condition at small atom number. However, the factor of g^2 tells us that stronger confinement will be helpful to speed up the process.

4.4 Number Fluctuation in a Degenerate Bose Gas

The fluctuation of the number of particles in a classical ideal gas is given by $\Delta N = N^{1/2}$, where N is the mean atom number [52]. However, for a degenerate Bose gas, this is not necessarily true and has been the topic of intense theoretical debate.

In the case of an ideal Bose gas, number fluctuations have been studied in a homogeneous case (box trap) [53, 54, 55] and, more recently, in an inhomogeneous case (harmonic trap) [56, 57, 58, 59, 60, 61] by both microcanonical and canonical approaches.

For a weakly interacting Bose gas, number fluctuations were first studied in Ref. [62]. The effect of interaction was then further explored by considering the thermal excitation of phonons in the thermodynamic limit with number-nonconserving [63] and number-conserving [64] Bogoliubov methods, where the number fluctuations were found to be $\Delta N \propto N^{4/3}$. Most recently, an isolated system of finite atom number was considered for studying number fluctuations in a harmonic trap [65] and in a box [66]. The result obtained in Ref. [65] predicted number fluctuation proportional to $N^{22/15}$ while Ref. [66] predicted $\Delta N \propto N^{1/2}$. Since the minimum predicted number fluctuation is $N^{1/2}$, which is also the "shot noise limit," we use $N^{1/2}$ as a benchmark for the comparison of our experimental data.

4.5 Experiment

This section describes the experimental realization of a system which incorporates single-atom counting with a Bose-Einstein condensate (BEC) apparatus, and the first direct measurement of sub-Poissonian atom number statistics in a degenerate Bose gas. Several experimental details including the stabilization of the optical trap, characterization of technical noise, and the atom counting technique are also discussed.

4.5.1 BEC in an Ultra-stable Optical Box Trap

The idea of achieving sub-Poissonian number fluctuations is the following mechanism (Fig. 4.3): for a fully loaded trap, the potential depth U_0 in the shallowest direction will be equal to the chemical potential μ of the degenerate Bose gas (if one neglects tunnelling out of the trap). Since, in the Thomas-Fermi (TF) limit, the atom number N is proportional to $\mu^{5/2}$ for a harmonic trapping potential as, the atom number is related to the trap depth as $N \propto U_0^{5/2}$. It is thus clear that precise control of the trap depth (even when assuming tunneling and a realistic nonharmonic potential) can lead to precise control of the atom number. However, in BEC experiments reported thus far, typical shot-to-shot number fluctuations greatly exceed the Poissonian limit, presumably due to technical noise. Therefore, an ultra-stable optical trap which has a controllable trapping volume and depth is necessarily for us.

To study the sub-Poissonian number statistics, a cold atomic cloud of about 10^6 atoms is prepared in a QUIC magnetic trap by stopping the evaporation shortly before the onset of BEC. The atoms are then transfered back to the center of the glass cell by reducing the current in the two quadrupole coils. Once the atoms are moved back to the center, the magnetic trap is ramped down and the atoms

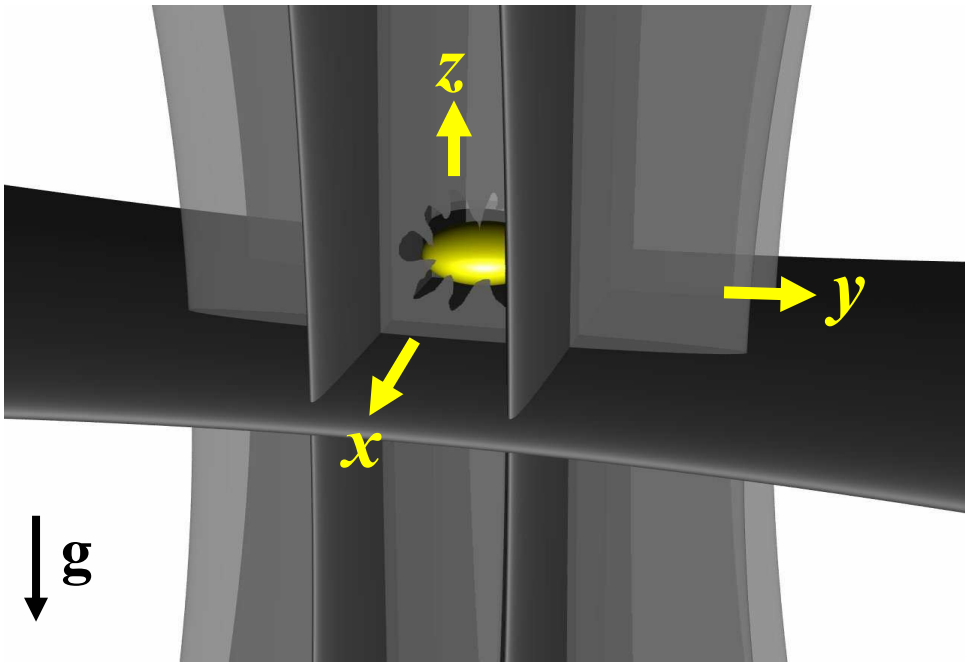

Figure 4.7: Pictorial of the optical trap. The trap is formed by five Gaussian sheets, with two pairs propagating vertically in y and z directions and one horizontal sheet in x to hold the atoms against gravity. All beams originate from a 10 W laser at $\lambda = 532\,\text{nm}$ and are tightly focused in one axis at the position of the condensate. Each sheet pair is derived from the first order deflections of multiple frequency acousto-optical modulators (AOMs), providing independent control of the position and power [67]. Gravity points in -z direction in this pictorial.

are transfered to a gravito-optical. Followed by the evaporation in this large-volume optical trap, a BEC of 2×10^5 Rb^{87} atoms is produced. The BEC is then compressed to a cigar shape by the same mean of obtaining one-dimensional BECs. However, the laser power used here is much less than that in the 1D BEC case, and the separation of the "end cap" beams is also smaller ($\sim 10\mu$m).

The final optical trap is formed by five Gaussian sheets, with two pairs propagating vertically and one horizontal sheet to hold the atoms against gravity, shown pictorially in Fig. 4.7. All beams originate from a 10 W laser at $\lambda = 532\,$nm and are tightly focused in one axis at the position of the condensate. Each sheet pair is derived from the first order deflections of multiple frequency acousto-optical modulators (AOMs), providing independent control of the position and power [67]. The sheet pairs and the horizontal sheet have a maximum power of $P_x^{\max} = 25\,$mW, $P_y^{\max} = 80\,$mW, $P_z^{\max} = 100\,$mW per sheet and a $1/e^2$ radius of $2.5\,\mu$m $\times$ $100\,\mu$m for the x and y axes and $3.4\,\mu$m $\times$ $200\,\mu$m for the z axis, respectively.

Fig. 4.8 shows the calculated potentials in the x, y, and z directions, given by the typical beam parameters in the experiment. The calculations are based on the following formula:

$$U(x,0,0) = U_G(x - \frac{L_x}{2}, 0, W_{1x}, W_{1y}, P_x) + U_G(x + \frac{L_x}{2}, 0, W_{1x}, W_{1y}, P_x), \quad (4.10)$$

$$U(0,y,0) = U_G(0, y - \frac{L_y}{2}, W_{1x}, W_{1y}, P_y) + U_G(0, y + \frac{L_y}{2}, W_{2x}, W_{2y}, P_y), \quad (4.11)$$

and

$$U(0,0,z) = U_G(0, z, W_{3y}, W_{3y}, P_z) + mgz, \quad (4.12)$$

with a constant offset not shown in the equation. In these equations, m is the mass

Table 4.1: Beam parameters of optical trap used to study sub-Poissonian statistics.

Sheet pair propagating in the yz plane		
P_x		power of single beam
W_{1x}	$2.5\mu m$	beam waist in x direction
W_{1y}	$100\mu m$	beam waist in y direction
L_x	$5\mu m$	separation of the sheet pair
Sheet pair propagating in the xz plane		
P_y		power of single beam
W_{2x}	$100\mu m$	beam waist in x direction
W_{2y}	$2.5\mu m$	beam waist in y direction
L_y	$11\mu m$	separation of the sheet pair
Single sheet propagating in the xy plane		
P_z		beam power
W_{3y}	$200\mu m$	beam waist in y direction
W_{3z}	$3.4\mu m$	beam waist in z direction

of ^{87}Rb atom, g is the acceleration of gravity, and the form of U_G is

$$U_G = -\frac{\hbar\Gamma^2}{8I_s}\left(\frac{1}{\omega_0-\omega}+\frac{1}{\omega_0+\omega}\right)\frac{2P}{\pi W_q W_p}e^{-\frac{2q^2}{W_q^2}}e^{-\frac{2p^2}{W_p^2}}, \tag{4.13}$$

where $\hbar$ is the Planck constant divided by 2π, Γ is the natural linewidth, and I_s is the saturation intensity. The definitions and the magnitudes of the rest of the parameters are listed in Table. 4.1.

In our experiment, the trap depth U_0 is ramped down adiabatically over a period of 1500 ms with an exponential shape. U_0, being the lowest evaporation barrier, determines the chemical potential and thus the atom number. Its final value is varied to obtain different atom numbers. For typical operating conditions, $U_0/k_B = 22\,\mathrm{nK}$ (for $P_x = 0.2\,\mathrm{mW}$) with the weakest trapping potential in the x direction where the decrease of the trap depth (or "evaporation") occurs. The calculated geometric mean trapping frequency is $\bar{\omega} = 2\pi\times 300\,\mathrm{Hz}$ ($\omega_x = 2\pi\times 200\,\mathrm{Hz}$,

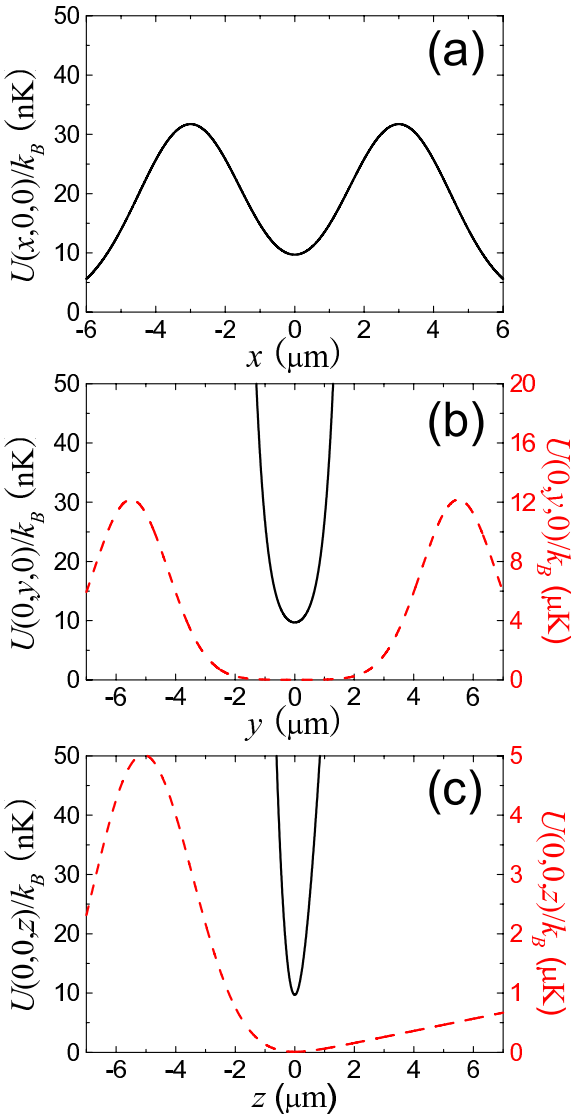

Figure 4.8: Potential plots of the optical trap. (a) This plot shows the potential energy U at $y = z = 0$. In the x direction, the atoms are confined by two Gaussian sheets with a separation of $l_x = 5\,\mu$m. (b) Confinement in the y direction is of similar shape to the x direction but deeper. (c) In the z direction, gravity and a Gaussian sheet form a gravito-optical trap. The dashed curves in (b) and (c) show the same potentials for the different scales given on the right axes. Each potential plot is calculated based on measured beam characteristics and are appropriate for the order of 100 atoms.

$\omega_y = 2\pi\times$ 200 Hz, $\omega_z = 2\pi\times$ 630 Hz). Since the atom number in the stability of U_0 has significant effect on the number fluctuation, a lot of effort is made on the beam pointing stability and stabilizing the beam intensities (including the short-term fluctuation and long-term drift).

To stabilize the beam intensity, we pick off the back reflection of each beam from one of the optics (for example, a lens) in the beam path and stabilize its intensity. The method of picking off the beam from the back reflection is found to be better than using a glass plate because the glass plates might have thermal effect which causes extra instability. The best choice of the optics is usually the one closest to the atoms if it is available. This choice can reduce the possibility of getting intensity fluctuation from the subsequent optics. The pick-off beam is then sent into a photodiode (THORLABS, FDS100; rise time: 20 ns, dark current: 20 nA, responsibility @ 532 nm: 0.3 A/W) whose output is feedback via a PID circuit [13] to the voltage input of a bi-phase attenuator (Mini-Circuits, ZAS-3; 1MHz-2GHz) which attenuates the RF power to the corresponding AOM (Fig. 4.9).

Since the beam pointing stability is directly related to the frequency stability of the RF sent to the corresponding AOM, we also stabilize the RF frequency. To stabilize the RF frequency, we implement a homebuilt, temperature-stabilized voltage controlled oscillator (VCO). Each VCO (Mini-Circuits, POS-150; 15-2000 MHz) is in good contact with a copper bar (Fig. 4.10). The bar has a hole drilled in the middle in which a thermistor (Panasonic, ERT-D2FHL103S; resistance @ 25^{o}C: 10 k$\Omega \pm 15\%$, responsibility @ 20-30^{o}C: 450 Ω/C) is installed. The readout of the thermistor is sent to an ultra-stable temperature controller (Wavelength Electronics, WTC3243; stability @ 25^{o}C: 0.008^{o}C/day) whose output is used to feedback to a thermal electric cooler (TEC, not shown in the photo) which is in contact with the

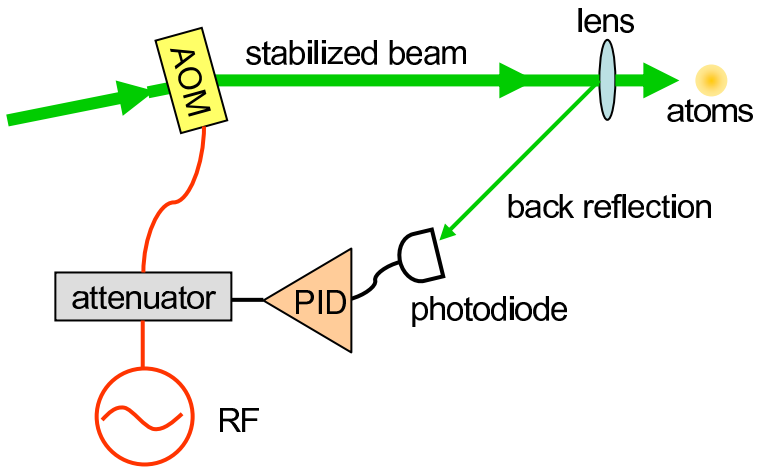

Figure 4.9: Intensity feedback loop for the ultra-stable optical box trap. The back reflection of the beam is picked off and used by a PID circuit to feedback the voltage input of the RF attenuator which controls the beam power.

copper bar. The copper bar, the thermistor, and the TEC are all covered by a layer of hot melt glue to insulate from the air, although the fluctuation of the room temperature is well below half degree Celsius.

Understanding every possible source of technical noise is also a very important issue, because any resulting atom number fluctuation can easily wash out the number statistics we want to observe. Hence, we measure the technical noise from all the possible sources and calculate the corresponding number fluctuations.

In the x direction (where the well depth is lowered) and the y direction (where the sheet holds the atoms against the gravity), the beam is stabilized by the PID lock circuit and the root-mean-square (rms) fluctuation of the laser intensity is measured to be $\Delta P_{x,rms} = \Delta P_{z,rms} \sim 1\%$. In the y direction, the beam is not stabilized, and the measured rms fluctuation of the laser intensity is about $\Delta P_{y,rms} \sim 5\%$.

The stability of the relative position for each beam is basically limited by the frequency stability of the VCOs, which is about 25 kHz. With the correspondence

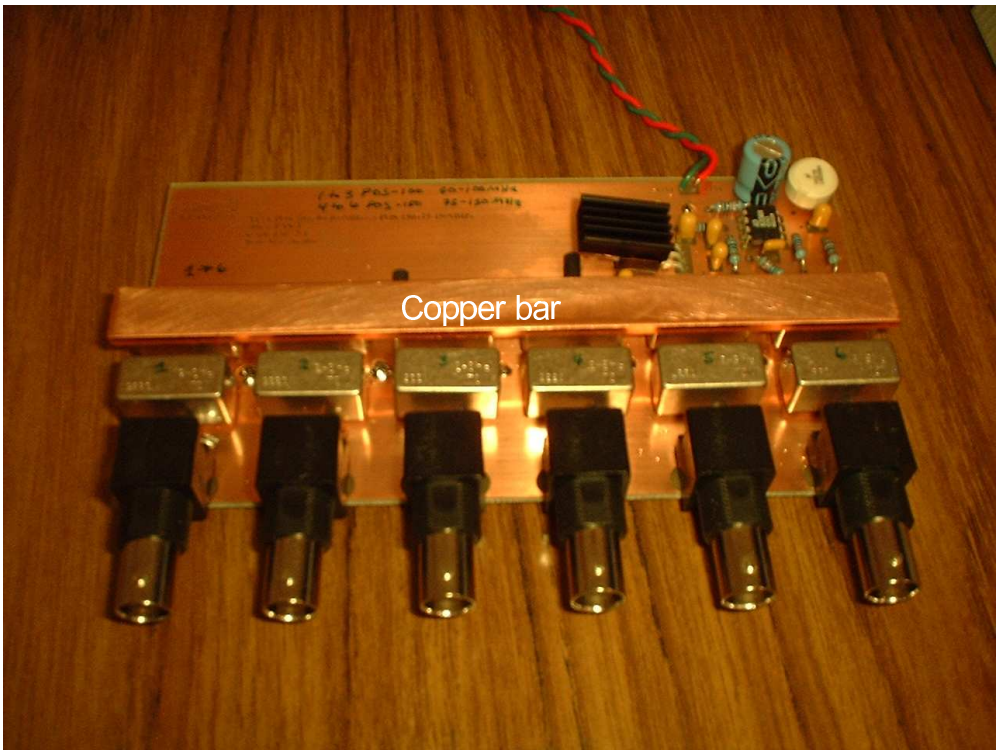

Figure 4.10: Temperature-stabilized voltage controlled oscillators (VCOs). Each VCO on the board (hardly seen in the photo) is in good contact with a copper bar. A thermistor is installed inside the bar and the readout is sent to an ultra-stable temperature controller which is used to feedback a thermal electric cooler (TEC) that is in touch with the copper bar (not shown in the photo). The copper bar, the thermistor, and the TEC will all be covered by a layer of hot melt glue to insulate from the air although the fluctuation of the room temperature is well below half degree Celsius.

between the frequency and the beam position as $1\mu m$/MHz, this gives an absolute fluctuation of $\Delta L_{x,rms} = \Delta L_{y,rms} \sim 0.025\mu m$ in every direction and a relative fluctuation of $\Delta L_{x,rms}/L_x \sim 0.5\%$ and $\Delta L_{y,rms}/L_y \sim 0.23\%$.

Based on the these measurements, we can estimate the probable number fluctuations caused by the technical noises. In order to do this calculation, one should use the method described in [48] to calculate the atom number and the chemical potential in a finite-height potential well, and also consider the quantum tunneling through the well. However, for simplicity, let's assume a three dimensional harmonic trap, apply the TF approximation, and neglect any possible tunneling in the well. Because there is no tunneling, the chemical potential will be equal to the well depth,

$$\mu = U_0, \tag{4.14}$$

and the atom number will be related to the chemical potential as [2]

$$N = \frac{8\pi}{15}\left(\frac{2\mu}{m\bar{\omega}^2}\right)^{3/2}\frac{\mu}{g}, \tag{4.15}$$

where m is the mass, $\bar{\omega} = (\omega_x\omega_y\omega_z)^{1/3}$ is the geometric mean of the trapping frequency, and $g = 4\pi\hbar^2 a_s/m$ is the coefficient of the interaction with the s-wave scattering length a_s. From Eq. (4.14), Eq. (4.15), and the measured technical noise, we can therefore estimate the corresponding number fluctuation for each parameters used in the experiment. The results are listed in Table. 4.2 for a typical case of $N = 136$. The overall atom number fluctuation caused by these technical noises is thus

$$\frac{\Delta N_{technical}}{N} = \sqrt{\sum_i \left(\frac{\Delta N_i}{N}\right)^2} = 4.3\%. \tag{4.16}$$

Table 4.2: Measured noise and the corresponding number fluctuation.

Parameters	rms Fluctuation	Corresponding $\Delta N_i/N$
P_x	1%	2%
P_y	5%	2.4%
P_z	1%	0.076%
L_x	0.5%	2.2%
L_y	0.23%	2%

4.5.2 Atom Counting

What we also learn from the estimated number fluctuation Eq. (4.16) is that there will be a limit for observing the sub-Poissonian number statistics. Because, when the number fluctuation caused by the technical noise is greater than the Poissonian number fluctuation, we will not be able to resolve it. Therefore, in order to observe statistics below the Poissonian fluctuation, we need

$$\Delta N_{technical} < \Delta N_{Poissonian}, \tag{4.17}$$

which means that we can observe sub-Poissonian number fluctuation only if

$$N < 450. \tag{4.18}$$

The two most popular methods of (destructively) measuring the atom number in the cold atom experiments are the absorption and fluorescence methods. For small atom numbers, the absorption imaging might be invisible due to the fluctuation of the probe beam intensity. The fluorescence imaging, on the other hand, has the advantage of being background-free, although its signal strength is much weaker than the absorption method. Because of these facts, two methods are employed

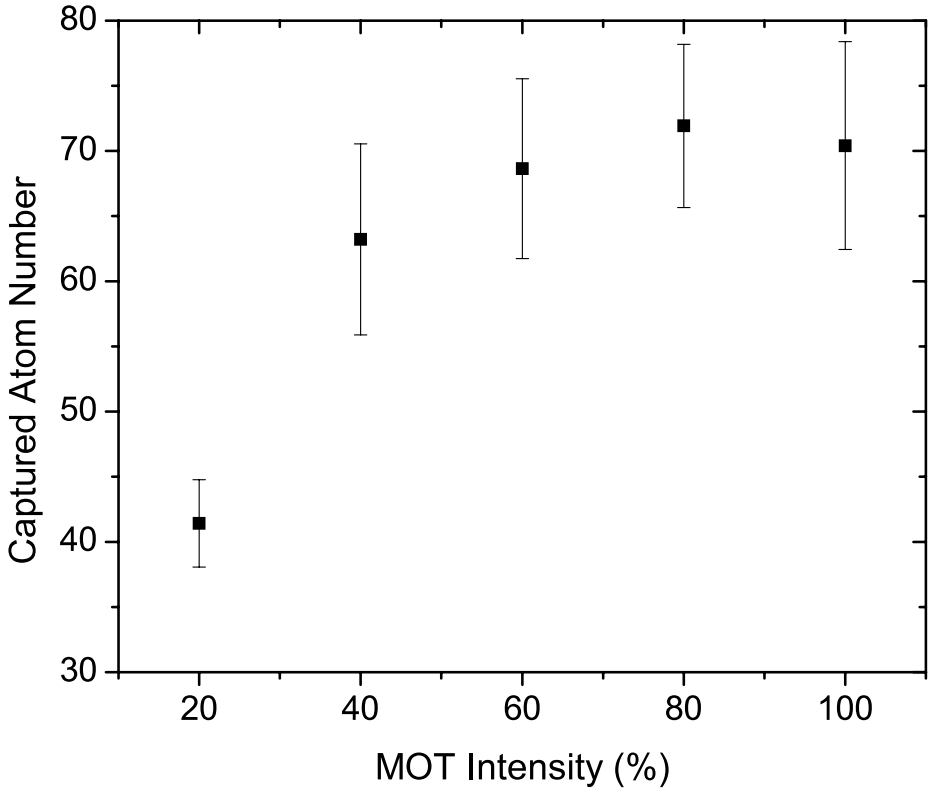

Figure 4.11: Capture efficiency for different MOT intensities. The MOT uses six beams with a diameter of 1 mm, an intensity of 65 mW/cm^2, a detuning of about 10 MHz, and a magnetic field gradient of 260 G/cm. Transfer from the optical trap to the MOT shows a saturation behavior with MOT beam intensity, indicating that all atoms are captured.

for measurements of atom numbers in our experiment. For numbers of order 10^3 or larger, absorption imaging is used yielding spatial and number information. At lower atom numbers however, fluorescence imaging is used because of the higher signal-to-noise ratio in this regime.

The fluorescence imaging used in our experiment is accomplished by transferring the atoms into a small magneto-optical trap (MOT) [68, 69]. The MOT uses six beams with a diameter of 1 mm, an intensity of 65 mW/cm^2, a detuning of about 10 MHz, and a magnetic field gradient of 260 G/cm. As shown in Fig. 4.11, transfer from the optical trap to the MOT shows a saturation behavior with MOT beam intensity, indicating that all atoms are captured. The resulting fluorescence signal is then detected by a charge-coupled-device (CCD) camera (Apogee, Alta U47+; air-cooled) for 100 ms. Since atomic density is low, there is little possibility for multiple scattering events during detection. Therefore, the measured fluorescence signal from the MOT is proportional to the number of atoms present.

In order to obtain high accuracy on the measured atom number, the fluorescence signal detected by the CCD camera is calibrated against an avalanche photodiode (APD) from Perkin Elmer (model SPCM-AQR-14). Under optimized MOT intensity and detuning, the APD, which is operated in the single-photon-counting mode, can easily resolve the fluorescence rate of a single atom (typically 10,000 s^{-1}). However, these MOT settings are always not ideal for capturing the atoms released from the optical box trap, which requires high capture efficiency. Therefore, to calibrate the atom number measured by the fluorescence imaging, we first experimentally determine the correspondence between the fluorescence counts and the measured atom number, $\alpha = N^{APD}_{counts}/N^{APD}_{counts}$, under the MOT setting where the fluorescence rate of a single atom is resolvable. To do this, we prepare a different

number of atoms by randomly capturing atoms from the background vapor. Then, we measure the atom number with the APD as shown in Fig. 4.12. From the slope of the fit, we can find α.

Next, let's link the atom numbers measured under different MOT settings. The measured atom number N_{atoms} is related to the integrated number of counts on the CCD chip N_{counts} by [15]

$$N_{atoms} = \frac{8\pi \left[1 + 4(\Delta/\Gamma)^2 + I_0/I_{sat}\right]}{\Gamma(I_0/I_{sat}) t_{exp}\, \eta_{count}\, d\Omega} N_{counts}, \tag{4.19}$$

where Δ is the MOT detuning, Γ is the natural linewidth, I_0 is the MOT intensity, I_{sat} is the saturation intensity, t_{exp} is the CCD exposure time, η_{count} is the quantum efficiency of the CCD camera (in counts/photon), and

$$d\Omega = \frac{\pi}{4} \left(\frac{f}{(f/\sharp) d_0} \right)^2 \tag{4.20}$$

is the solid angle of the collected light by CCD with f being the focal length of the imaging lens, d_0 is the distance between the MOT and the lens, and $f/\sharp$ is the f-number of the lens. The magnetic field and the situation of atoms being localized in the MOT lattice are ignored in Eq. (4.19). The atom number measured in the fluorescence imaging can thus be calibrated through the formula,

$$N_{atoms}^{APD} = \frac{1 + 4(\Delta^{fluo}/\Gamma)^2 + (I_0^{fluo}/I_{sat})}{1 + 4(\Delta^{APD}/\Gamma)^2 + (I_0^{APD}/I_{sat})} \frac{I_0^{APD}}{I_0^{fluo}} \alpha N_{atoms}^{fluo}, \tag{4.21}$$

where $\Delta^{fluo} = -7.5$ MHz, $\Delta^{APD} = -2.5$ MHz, $I_0^{fluo} = 64$ mW/cm^2, and $I_0^{APD} = 8$ mW/cm^2.

An alternative way to calibrate the atom number obtained from the fluo-

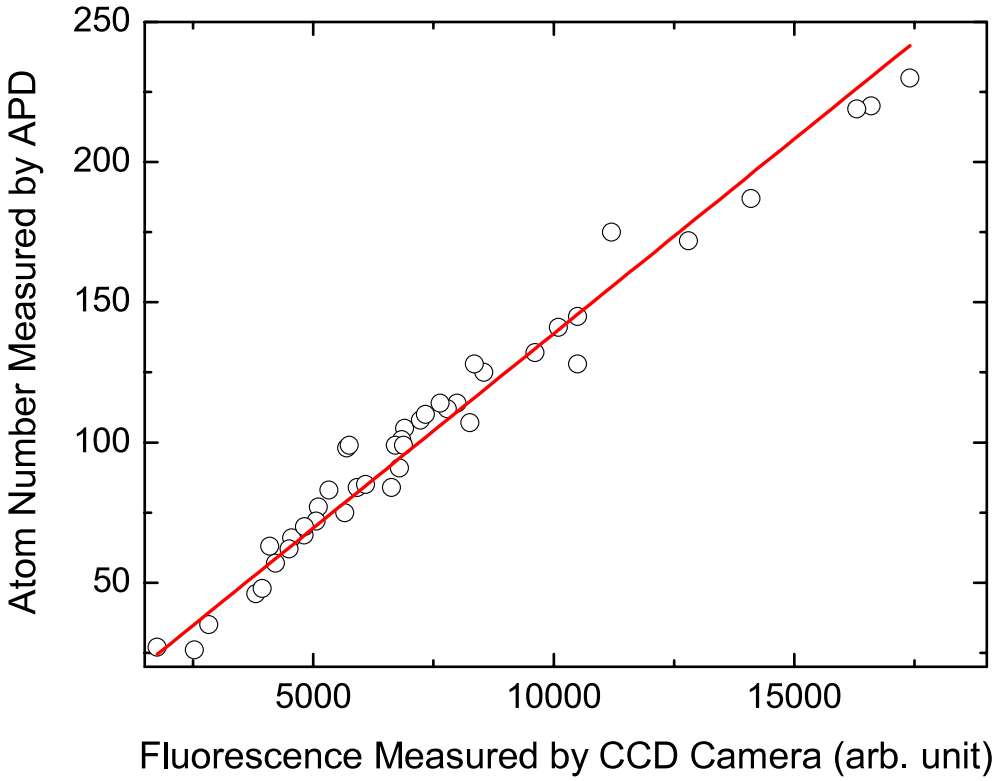

Figure 4.12: Calibration of atom number measured by fluorescence imaging. At the typical MOT intensity and detuning used in the experiment, the avanlanche photodiode (APD) is not able to resolve the fluorescence rate of a single atom. Therefore, the dependence of the atom numbers on the fluorescence count is first determined under the MOT setting where the fluorescence rate of a single atom is resolvable. This is accomplished by preparing a different number of atoms in the MOT from random capture of the background vapor and then measuring the atom number with both the CCD camera and the APD. From the slope of the fit, $\alpha = N^{APD}_{counts}/N^{APD}_{counts}$ can be obtained. The atom number measured in the fluorescence imaging N^{fluo}_{atoms} can then be calibrated by Eq. (4.21).

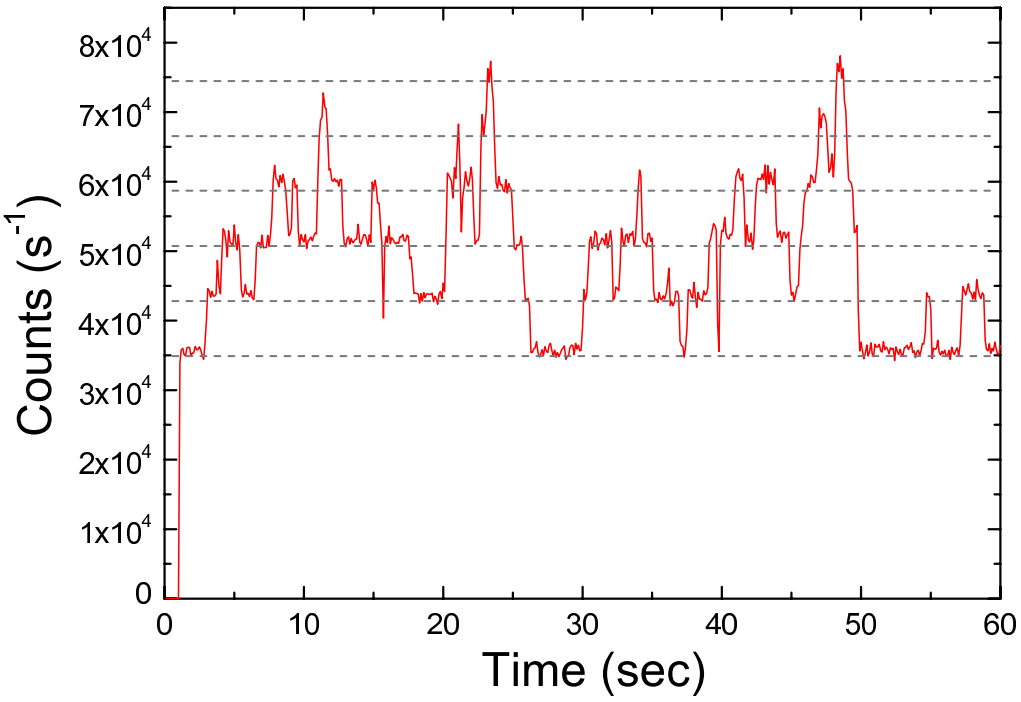

Figure 4.13: Step-wise signal of the avalanche photodiode (APD). The atom number from CCD fluorescence imaging is calibrated by an APD operating in photon counting mode. The fluorescence counting rate per atom is $9,000\,\mathrm{s}^{-1}$ with a background of $35,000\,\mathrm{s}^{-1}$. The signals shown are for random loading of the MOT from background vapor. The MOT uses six beams with a diameter of 1 mm, an intensity of 8 mW/cm^2, a detuning of about 5 MHz, and a magnetic field gradient of 260 G/cm. The horizontal dashed lines from bottom to top indicate the fluorescence levels of the background, one atom, two atoms, three atoms, four atoms, and five atoms. The time step of fluorescence binning is 100 ms.

rescence imaging is accomplished by first operating the MOT in a regime where discrete fluorescence levels of different small atom numbers are observable on an APD, as shown in Fig. 4.13, so that we know exactly how many atoms are being calibrated. The MOT, with a few atoms in it, is then suddenly switched to the typical operating settings described above and the new fluorescence level is obtained for the same atom number (Fig. 4.14). This yields an absolute accuracy in atom number better than $\pm 10\,\%$ (For absorption imaging, the absolute accuracy in atom number is estimated to be $\pm 25\,\%$.) The result is consistent with calculations of the ratio of scattering rates for the given settings (Eq. (4.21)). Atom numbers may also be estimated by using the TF approximation with $\mu = U_0$ and modeling the trap by a harmonic potential. This yields a $35\,\%$ deviation below the measured atom numbers, indicating rough accuracy of this model.

Due to inhomogeneity of the optical potential, after the potential barrier is lowered, some atoms remain outside of the trap. These atoms are removed before the final number detection by raising the potential barrier to its maximum intensity ($U_0^{\max}/k_B = 3\,\mu\mathrm{K}$) and using a supplementary optical sheet pair to sweep the residual atoms away from the well. A magnetic gradient of about 5 G/cm is also applied to remove atoms outside the range of the sweeping beams. A cartoon view of these processes is shown in Fig. 4.15.

4.5.3 Experimental Result

Since we know that it is only possible to observe sub-Poissonian number statistics for less than 500 atoms, it is important to verify the ability of our optical box trap for loading small atom number before we measure any atom number statistics. Therefore, we vary the well depth and measure the number of atoms trapped inside

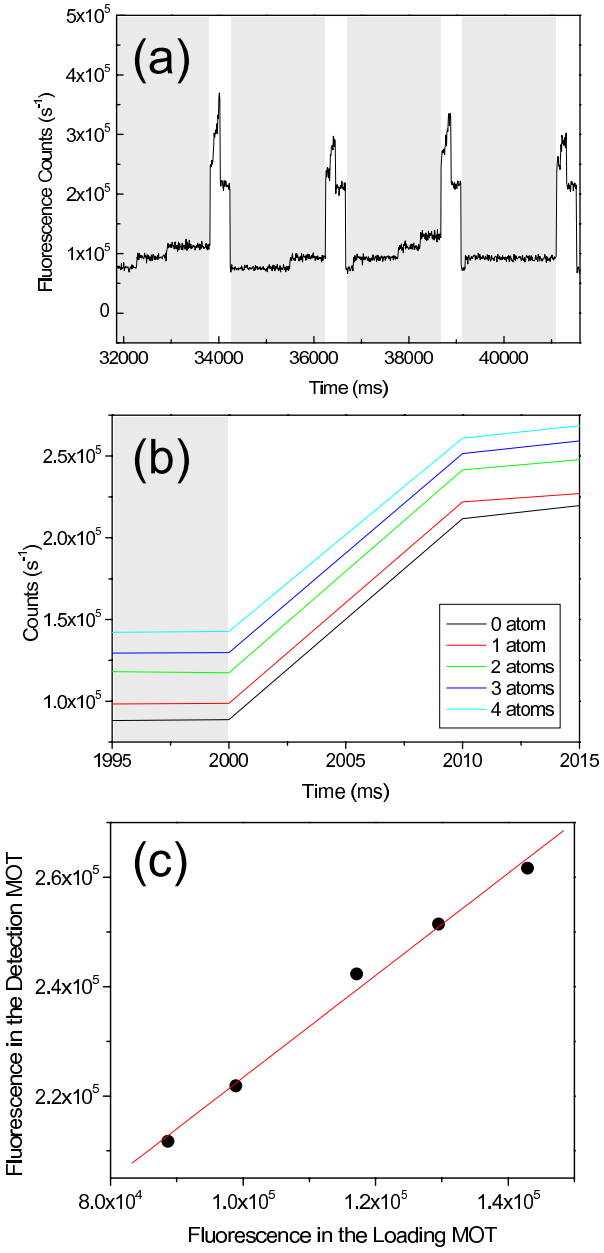

Figure 4.14: Calibration of atom number between two MOT settings. (a) Atoms are first prepared in a MOT where the fluorescence level of a single atom is resolvable (gray regions). The MOT is then suddenly switched to the setting used in the typical detection (white regions). (b) Change of fluorescence levels between the two MOT settings. (c) Calibration is obtained from the averaged data of (b).

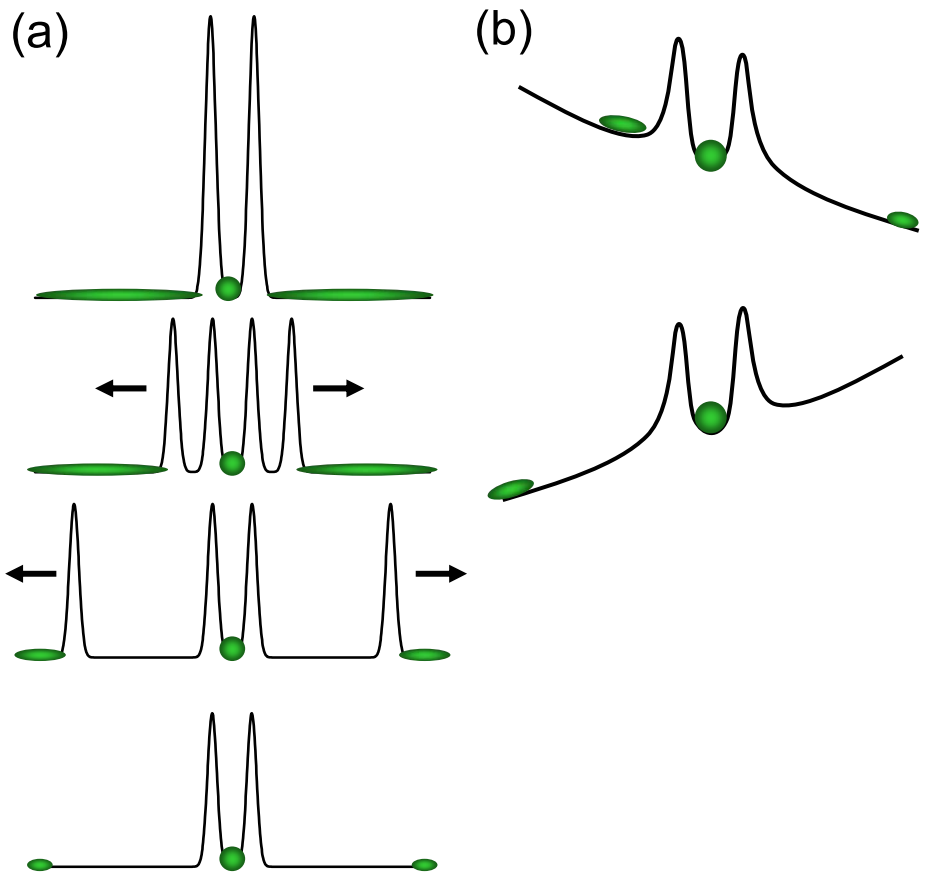

Figure 4.15: Cleaning processes prior to the detection. (a) The potential barrier is raised to protect the atoms inside the trap. The atoms remaining outside of the trap are removed by using a supplementary optical sheet pair to sweep the residual atoms away from the well. (b) A magnetic gradient of about 5 G/cm is also applied to remove atoms outside the range of the sweeping beams.

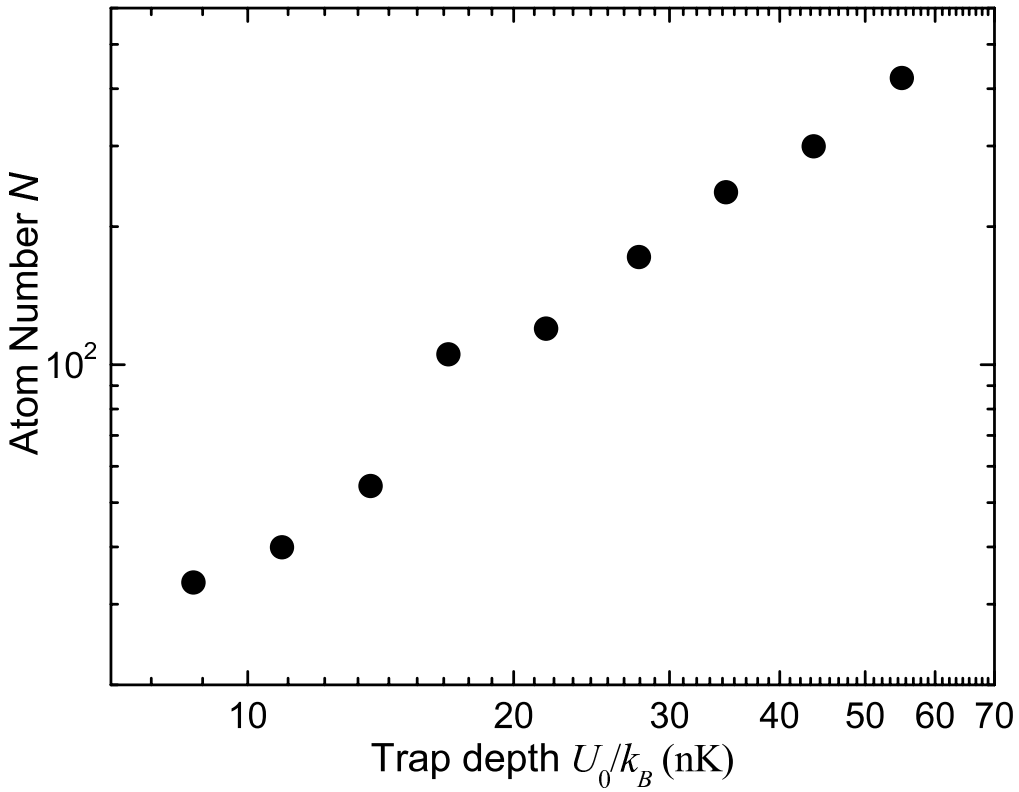

Figure 4.16: Dependence of atom number on the trap depth. The atom number N shows a nice dependence on the trap depth U_0 for 30 to 500 atoms, indicating the ability of our optical box trap to provide sub-Poissonian number statistics. The data could be used to determine the shape of the trap.

the optical box. As shown in Fig. 4.16, a nice correspondence exists between the atom number N and the trap depth U_0 for 30 to 500 atoms, indicating the ability of our optical box trap to acieve sub-Poissonian number statistics. Fig. 4.16 can also be used to determine the shape of our trap.

The atom number statistics is measured simply by repeating the atom number measurement many times. A typical number of runs is about one hundred. Fig. 4.17 shows the measured fluctuations normalized to the Poissonian case $\sigma_N/\sqrt{N}$ (solid circles) as a function of atom number N. Sub-Poissonian fluctuations are ob-

served for atom numbers below 500 as we expect, where the technical noise is no longer dominant. The measured fluctuation at $N = 60$ atoms is approximately 60 % of the corresponding Poissonian fluctuation. This series of 100 measurements is shown as a histogram plot in Fig. 4.18 where the raw data is also given. A Gaussian fit to the data distribution indicates a measured standard deviation of $\sigma_N/N = 7.9\,\%$ with a 99 % confidence interval of $[\,7.4\,\%, 8.5\,\%\,]$. This indicates a reliable measurement of deviation well below the Poissonian value of $N^{1/2}/N = (12.9 \pm 0.5)\,\%$, where the error is given by absolute accuracy in atom number.

A 99 % *confidence interval* is defined as [70]

$$[\,\sqrt{\frac{n-1}{\chi^2_{0.005}(n-1)}}\sigma_N, \sqrt{\frac{n-1}{\chi^2_{0.995}(n-1)}}\sigma_N\,], \tag{4.22}$$

where σ_N is the measurement standard deviation, n is the number of samples, and $\chi^2_{0.005}(n\text{-}1)$, $\chi^2_{0.995}(n\text{-}1)$ are the upper 0.5 %, 99.5 % points of the chi-square distribution, respectively, with $n-1$ degrees of freedom. A simple interpretation of the 99 % *confidence interval* is that, if you repeat the n measurements for i times and calculate such interval from each $\sigma_{N,i}$, then 99% of the intervals will contain the number fluctuation when you perform infinite measurements, that is, the "true" value of σ_N.

For larger atom numbers ($N > 500$), the measured fluctuation is very close to what is estimated from several possible technical noise sources as given in Eq. (4.18) and comparable to the Poissoian fluctuation; therefore, only Poissonian statistics is observed. For lower atom numbers ($N < 500$), the contribution from the technical noise is negligible and thus sub-Poissonian statistics is observed. Background capture during the detection is a major contribution to the measured fluctuation for $N < 500$. The background capture during the 100 ms image-taking process with no

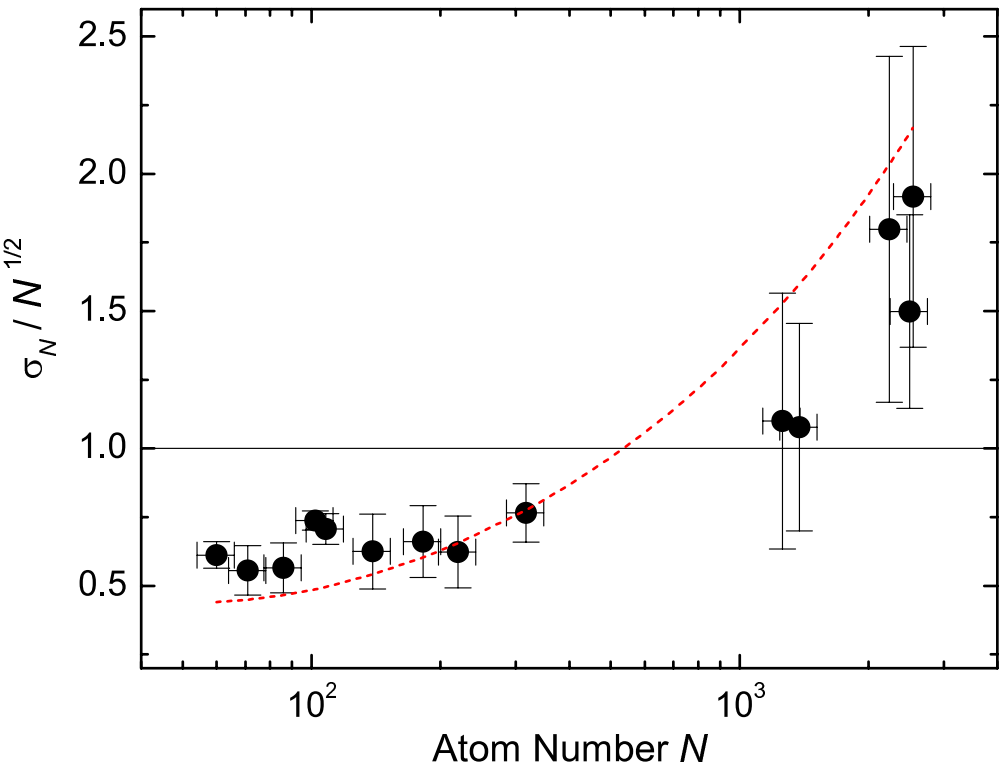

Figure 4.17: Observation of sub-Poissonian number statistics. The solid circles show the measured fluctuation normalized to the Poissonian case as a function of atom number. The vertical error bars are the 68 % confidence intervals for each measurement. The horizontal error bars represent the absolute accuracy in atom number. Sub-Poissonian number statistics is observed for atom numbers below 500 where the fluctuations due to technical noise are not larger than the Poissonian fluctuation. The dashed curve is the estimated fluctuation from technical noise and background capture.

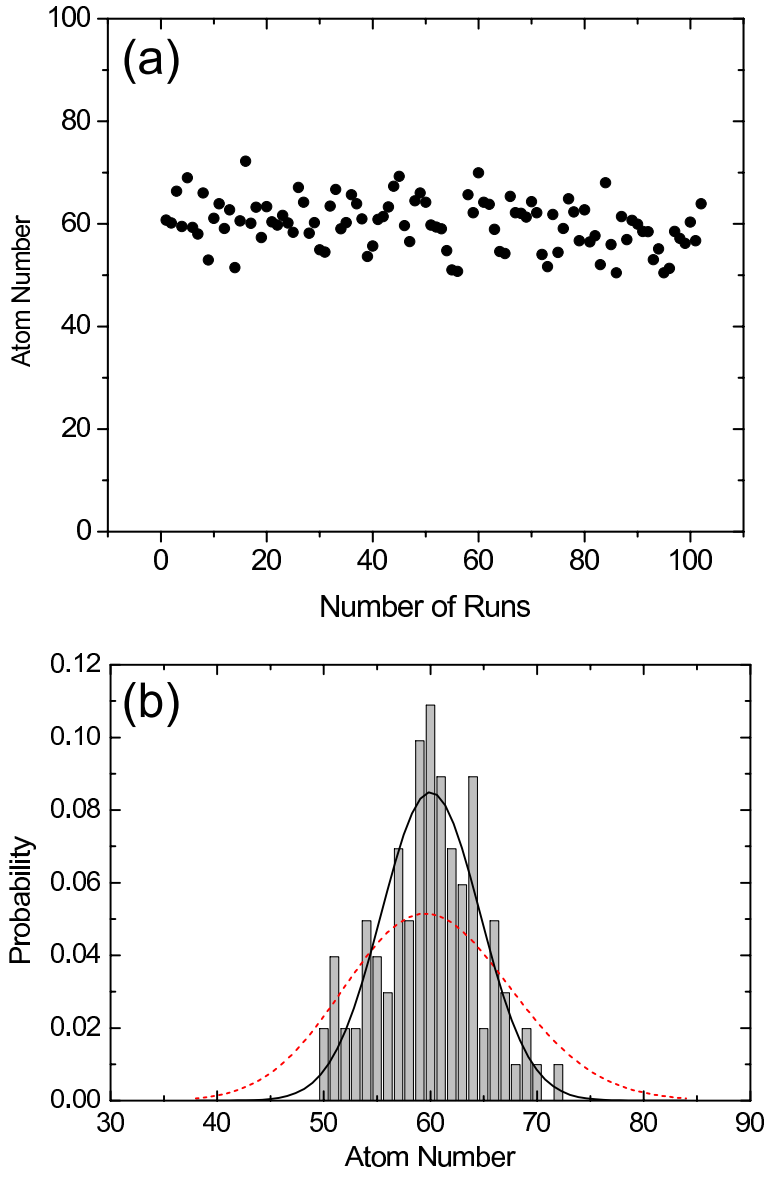

Figure 4.18: Number statistics for mean atom number $N = 60$. (a) Raw data of atom number statistics containg 100 sample points for 60 atoms. (b) Histogram of the measured number distribution shows sub-Poissonian statistics for mean atom number $N = 60$. The solid curve is the Gaussian fit to the distribution where the number fluctuation is extracted. The dashed curve is the Poissonian distribution with the same mean atom number.

atoms present is measured to have a mean of $N_{\rm bg} = 5$ atoms. This random process, which has Poissonian statistics, broadens the measured atom number distribution. A simple estimate of atom number fluctuation from both technical noise and background capture, assuming a constant background capture for different atom number N, results in

$$\sqrt{(\delta_{\rm tech})^2 + ((N_{\rm bg})^{1/2}/N)^2}, \tag{4.23}$$

shown as the dashed curve in Fig. 4.17. This result gives a similar increasing tendency as for the measured fluctuations. A more detailed calculation without TF approximation shows an increase in sensitivity to trap fluctuations at lower atom numbers [48].

We have also measured the dependence of atom statistics on the ramp time, $t_{\rm ramp}$, in order to probe the many-body dynamics. The results are displayed in Fig. 4.19 where the fluctuations (normalized to the Poissonian case) are plotted as a function of $t_{\rm ramp}$. We find that for time scales shorter than 250 ms, the atom statistics become super-Poissonian, while for longer times they are sub-Poissonian. This result provides the timescale for adiabatic following, a key feature of the process. An example of super-Poissonian statistics is shown in Fig. 4.20.

4.5.4 New Progress and Outlook

After the result of the observed sub-Poissonian fluctuation was published [71], the beam pointing stability was further improved intending to achieve sub-Poissonian number statistics for smaller atom numbers ($N < 60$). Two of the main improvements were the replacement of the homebuilt VCOs by the homebuilt, more stable direct digital synthesis (DDS) synthesizer [13], and the addition of a PID lock circuit to the beam path of the sheet pair (P_y) which was not stabilized before. The back-

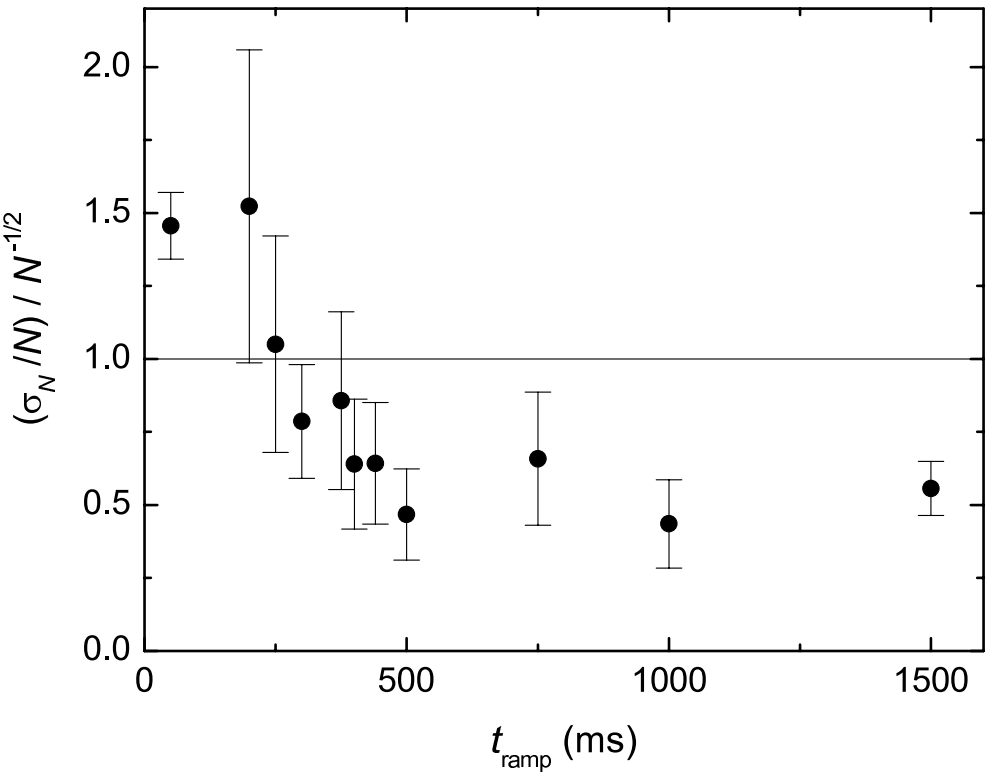

Figure 4.19: Dependence of atom number fluctuations on the adiabaticity. Atom number fluctuations (normalized to the Poissonian case) are measured as a function of ramp time t_{ramp}. Adiabaticity breaks down when the ramp time is shorter than 250 ms. The error bars show the 68 % confidence intervals for each measurement. The horizontal line shows the level of Poissonian fluctuation.

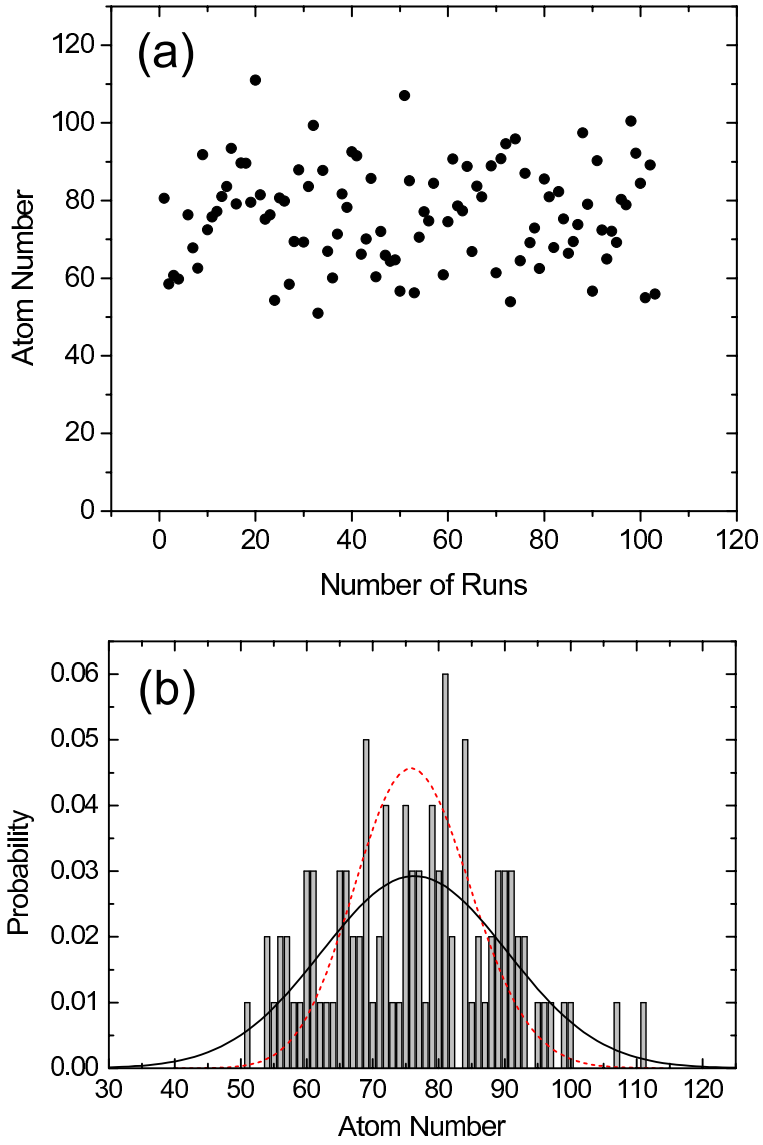

Figure 4.20: Observation of sub-Poissonian number statistics.(b) Histogram of 100 sample points shows sub-Poissonian statistics for mean atom number $N = 80$. The solid curve is the Gaussian fit to the distribution. The dashed curve is the Poissonian distribution with the same mean atom number.

ground capture during the detection was also minimized by adjusting the detuning and intensity of the MOT without losing the capture efficiency.

The effect of the improvements is immediately seen in the experiment. For mean atom number of 28, the measured number fluctuation is 12.2% with a 99% confidence interval of [10.3 %, 14.9%] (Fig. 4.21(b)); for mean atom number of 21, the measured number fluctuation is 12.4% with a 99% confidence interval of [11.0 %, 14.2%] (Fig. 4.21(a)). Therefore, both of the measured fluctuations are below the corresponding Poissonian values, which are 18.9% and 21.8%, respectively. However, we do not observe sub-Poissonian number statistics for atom numbers smaller than 20.

The remaining number fluctuations probably still result from the technical noise and the quantum tunneling through the potential barrier. The technical noise could be improved, for example, by stabilizing the intensity of each optical sheet independently in the sheet pair. To suppress the quantum tunneling, one could thicken the potential barrier by placing several optical sheets right next to each other.

The theoretical analysis of the dynamics in our system is still missing. This will require a time-dependent many-body theory without a mean-field approximation. Recent work on quantum kinetic theory [72, 73, 74] and the calculation in a finite-height trap [75] might be useful for exploring this topic. A similar theoretical work has been done in the analysis of relative number fluctuations between two BEC separated by a finite-height barrier that is ramped up in time [76], where sub-Poissonian fluctuations in the relative atom number is found to be possible under appropriate conditions.

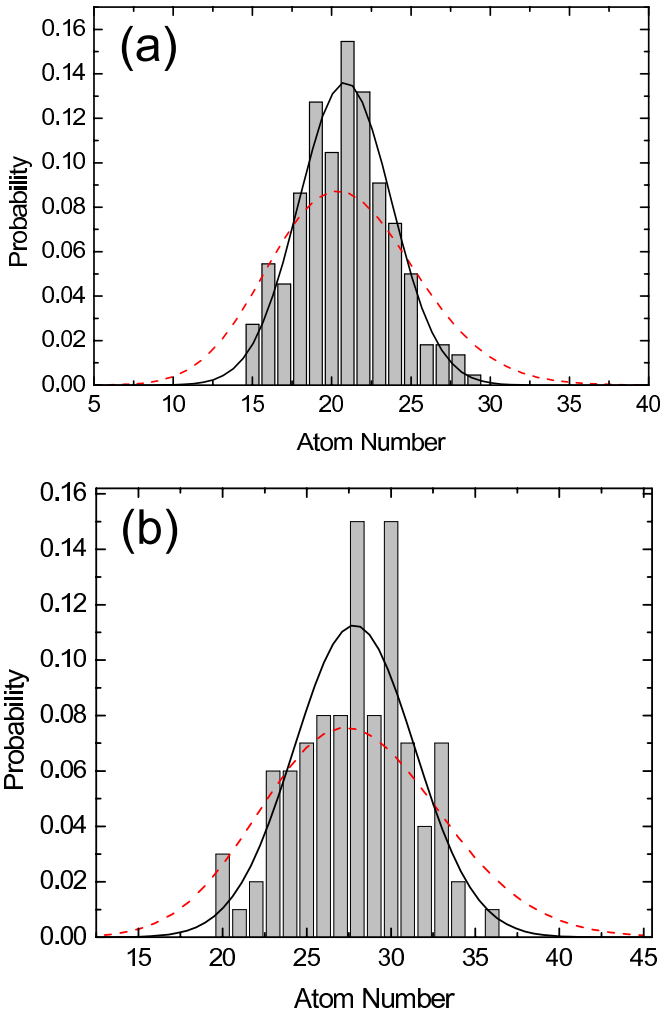

Figure 4.21: Number statistics for mean atom number (a) $N = 21$ and (b) $N = 28$. The solid curve is the Gaussian fit to the distribution. The dashed curve is the Poissonian distribution with the same mean atom number.

Bibliography

[1] K. Huang. *Statistical Mechanics*. John Wiley & Sons, New Jersey, 2003.

[2] C. J. Pethick and H. Smith. *Bose-Einstein Condensation in Dilute Gases*. Cambridge University Press, Cambridge, 2002.

[3] F. Dalfovo, S. Giorgini, L. P. Pitaevskii, and S. Stringari. Theory of bose-einstein condensation in trapped gases. *Rev. Mod. Phys.*, **71**:463, 1999.

[4] Y. Castin and R. Dum. Bose-einstein condensates in time dependent traps. *Phys. Rev. Lett.*, **77**:5315, 1996.

[5] H. J. Metcalf and P. van der Straten. *Laser Cooling and Trapping*. Springer-Verlag, New York, 1999.

[6] W. Ketterle, D.S. Durfee, and D.M. Stamper-Kurn. Making, probing and understanding Bose-Einstein condensates. *Bose-Einstein condensation in atomic gases*, *Proceedings of the International School of Physics "Enrico Fermi"*, *Course CXL*, edited by M. Inguscio, S. Stringari and C.E. Wieman (IOS Press, Amsterdam, 1999) pp. 67-176.

[7] I. Bloch T. Esslinger and T. W. Hänsch. Bose-einstein condensation in a quadrupole-ioffe-configuration trap. *Phys. Rev. A*, **58**:R2664, 1998.

[8] R. Grimm and M. Weidemüller. Optical dipole traps for neutral atoms. *Adv. At. Mol. Opt. Phys.*, **42**:95, 2000.

[9] J. H. Moore, C. C. Davis, and M. A. Coplan. *Building Scientific Apparatus.* Westview Press, Colorado, 2003.

[10] C. E. Weiman and L. Hollberg. Using diode lasers for atomic physics. *Rev. Sci. Instrum.*, **62**:1, 1991.

[11] K. B. MacAdam, A. Steinbach, and C. Wieman. A narrow-band tunable diode laser system with grating feedback, and a saturated absorption spectrometer for cs and rb. *Am. J. Phys.*, **60**:1098, 1992.

[12] W. Demtröder. *Laser Spectroscopy.* Springer, Berlin, 1998.

[13] T. P. Meyrath. Ph.D. thesis. University of Texas at Austin, 2005.

[14] B. G. Klappauf. Ph.D. thesis. University of Texas at Austin, 1998.

[15] D. A. Steck. Ph.D. thesis. University of Texas at Austin, 2001.

[16] J. A. Hanssen. Ph.D. thesis. University of Texas at Austin, 2004.

[17] D. Jaksch, C. Bruder, J. I. Cirac, C. W. Gardiner, and P. Zoller. Cold bosonic atoms in optical lattices. *Phys. Rev. Lett.*, **81**:3108, 1998.

[18] L. Tonks. The complete equation of state of one, two and three-dimensional gases of hard elastic spheres. *Phys. Rev.*, **50**:955, 1936.

[19] M. Girardeau. Relationship between systems of impenetrable bosons and fermions in one dimension. *J. Math. Phys.*, **1**:516, 1960.

[20] E. H. Lieb and W. Liniger. Exact analysis of an interacting bose gas. *Phys. Rev.*, **130**:1605, 1963.

[21] W. Alt. An objective lens for efficient fluorescence detection of single atoms. *Optik*, **113**:142, 2002.

[22] D. S. Petrov, G. V. Shlyapnikov, and J. T. M. Walraven. Regimes of quantum degeneracy in trapped 1d gases. *Phys. Rev. Lett.*, **85**:3745, 2000.

[23] D. S. Petrov, M. Holzmann3, and G. V. Shlyapnikov. Bose-einstein condensation in quasi-2d trapped gases. *Phys. Rev. Lett.*, **84**:2551, 2000.

[24] V. L. Berezinski. Destruction of long-range order in one-dimensional and two-dimensional systems prossessing a continous symmetry group. ii. quantum systems. *Sov. Phys. JETP*, **34**:610, 1972.

[25] J. M. Kosterlitz and D. J. Thouless. Ordering, metastability and phse-transitions in 2 dimensional system. *J. Phys. C*, **6**:1181, 1973.

[26] T.-L. Ho and M. Ma. Quasi 1 and $2d$ dilute bose gas in magnetic traps: Existence of off-diagonal order and anomalous quantum fluctuations. *J. Low Temp. Phys.*, **115**:61, 1999.

[27] S. Stringari. Dynamics of bose-einstein condensed gases in highly deformed traps. *Phys. Rev. A*, **58**:2385, 1998.

[28] T. Stöferle, H. Moritz, C. Schori, M. Köhl, and T. Esslinger. Transition from a strongly interacting 1d superfluid to a mott insulator. *Phys. Rev. Lett.*, **92**:130403, 2004.

[29] B. Laburthe Tolra, K. M. O'Hara, J. H. Huckans, W. D. Phillips, S. L. Rolston, and J. V. Porto. Observation of reduced three-body recombination in a correlated 1d degenerate bose gas. *Phys. Rev. Lett.*, **92**:190401, 2004.

[30] D. Rychtarik, B. Engeser, H.-C. Nägerl, and R. Grimm. Two-dimensional bose-einstein condensate in an optical surface trap. *Phys. Rev. Lett.*, **92**:173003, 2004.

[31] S. Stock, Z. Hadzibabica, B. Battelier, M. Cheneau, and J. Dalibard. Observation of phase defects in quasi-two-dimensional bose-einstein condensates. *Phys. Rev. Lett.*, **95**:190403, 2005.

[32] A. Görlitz, J. M. Vogels, A. E. Leanhardt, C. Raman, T. L. Gustavson, J. R. Abo-Shaeer, A. P. Chikkatur, S. Gupta, S. Inouye, T. Rosenband, and W. Ketterle. Realization of bose-einstein condensates in lower dimensions. *Phys. Rev. Lett.*, **87**:130402, 2001.

[33] Z. Hadzibabic1, P. Krüger, Marc Cheneau1, B. Battelier, and J. Dalibard. Berezinski-kosterlitz-thouless crossover in a trapped atomic gas. *Science*, **441**:1118, 2006.

[34] T. Kinoshita, T. Wenger, and D. S. Weiss. Observation of a one-dimensional tonks-girardeau gas. *Science*, **305**:1125, 2004.

[35] B. Paredes, A. Widera, V. Murg, O. Mandel, S. Fölling, I. Cirac, G. V. Shlyapnikov, T. W. Hänsch, and I. Bloch. Tonks-girardeau gas of ultracold atoms in an optical lattice. *Nature*, **429**:277, 2004.

[36] H. Moritz, T. Stöferle, M. Köhl, and T. Esslinger. Exciting collective oscillations in a trapped 1d gas. *Phys. Rev. Lett.*, **91**:250402, 2003.

[37] D. Jaksch, H.-J. Briegel, J. I. Cirac, C. W. Gardiner, and P. Zoller. Entanglement of atoms via cold controlled collisions. *Phys. Rev. Lett.*, **82**:1975, 1999.

[38] A. M. Dudarev, R. B. Diener, B. Wu, M. G. Raizen, and Q. Niu. Entanglement generation and multiparticle interferometry with neutral atoms. *Phys. Rev. Lett.*, **91**:010402, 2003.

[39] C. H. Bennett. Quantum information and computation. *Phys. Today*, **10**:24, 1995.

[40] P. Bermin Ed. *Atom Interferometry*. Academic Press, New York, 1997.

[41] P. Bouyer and M. A. Kasevich. Heisenberg-limited spectroscopy with degenerate bose-einstein gases. *Phys. Rev. A*, **56**:R1083, 1997.

[42] C. Orzel, A. K. Tuchman, M. L. Fenselau, M. Yasuda, and M. A. Kasevich. Squeezed states in a bose-einstein condensate. *Science*, **291**:2386, 2001.

[43] T. Schumm, S. Hofferberth, L. M. Andersson, S. Wildermuth, S. Groth, I. Bar-Joseph, J. Schmiedmayer, and P. Krüger. Matter-wave interferometry in a double well on an atom chip. *Nature Physics*, **1**:57, 2005.

[44] G.-B. Jo, Y. Shin, S. Will, T. A. Pasquini, M. Saba, W. Ketterle, D. E. Pritchard, M. Vengalattore, and M. Prentiss. Long Phase Coherence Time and Number Squeezing of two Bose-Einstein Condensates on an Atom Chip. cond-mat/0608585, 2006.

[45] M. Schellekens, R. Hoppeler, A. Perrin, J. Viana Gomes, D. Boiron, A. Aspect, and C. I. Westbrook. Hanbury brown twiss effect for ultracold quantum gases. *Science*, **310**:648, 2005.

[46] T. Kinoshita, T. Wenger, and D. S. Weiss. Local pair correlations in one-dimensional bose gases. *Phys. Rev. Lett.*, **95**:190406, 2005.

[47] W. Ketterle and H.-J. Miesner. Coherence properties of bose-einstein condensates and atom lasers. *Phys. Rev. A*, **56**:3291, 1997.

[48] A. M. Dudarev, M. G. Raizen, and Q. Niu. Quantum Many-Body Culling. quant-ph/0607072, 2006.

[49] L. S. Cederbaum and A. I. Streltsov. Best mean-field for condensates. *Phys. Lett. A*, **318**:564, 2003.

[50] D. Masiello, S. B. McKagan, and W. P. Reinhardt. Multiconfigurational hartree-fock theory for identical bosons in a double well. *Phys. Rev. A*, **72**:063624, 2005.

[51] G. E. Astrakharchik. Ph.D. thesis. Universita di Trento, 2004.

[52] L. D. Landau and E. M. Lifshitz. *Statistical Physics*. Butterworth-Heinemann, Oxford, third edition, 1998.

[53] E. H. Hauge. Fluctuations in the ground state occupation number of the ideal bose gas. *Physica Nor.*, **4**:19, 1969.

[54] I. Fujiwara, D. ter Haar, and H. Wergeland. Fluctuations in the population of the ground state of bose systems. *J. Stat. Phys.*, **2**:329, 1970.

[55] R. M. Ziff, G. E. Uhlenbeck, and M. Kac. The ideal bose-einstein gas, revisited. *Phys. Rep.*, **32**:169, 1977.

[56] H. D. Politzer. Condensate fluctuations of a trapped, ideal bose gas. *Phys. Rev. A*, **54**:5048, 1996.

[57] M. Gajda and K. Rzążewski. Fluctuations of bose-einstein condensate. *Phys. Rev. Lett.*, **78**:2686, 1997.

[58] P. Navez, D. Bitouk, M. Gajda, Z. Idziaszek, and K. Rzążewski. Fourth statistical ensemble for the bose-einstein condensate. *Phys. Rev. Lett.*, **79**:1789, 1997.

[59] M. Wilkens and C. Weiss. Particle number fluctuations in an ideal bose gas. *J. Mod. Opt.*, **44**:1801, 1997.

[60] S. Grossmann and M. Holthaus. Fluctuations of the particle number in a trapped bose-einstein condensate. *Phys. Rev. Lett.*, **79**:3557, 1997.

[61] N. L. Balazs and T. Bergeman. Statistical mechanics of ideal bose atoms in a harmonic trap. *Phys. Rev. A*, **58**:2359, 1998.

[62] E. Buffet and J. V. Pulè. Fluctuation properties of the imperfect bose gas. *J. Math. Phys.*, **24**:1608, 1983.

[63] S. Giorgini, L. P. Pitaevskii, and S. Stringari. Anomalous fluctuations of the condensate in interacting bose gases. *Phy. Rev. Lett.*, **80**:5040, 1998.

[64] V. V. Kocharovsky, Vl. V. Kocharovsky, and M. O. Scully. Condensate statistics in interacting and ideal dilute bose gases. *Phy. Rev. Lett.*, **84**:2306, 2000.

[65] S. Liu, H. Xiong, G. Huang, and Z. Xu. Anomalous particle-number fluctuations in a three-dimensional interacting bose-einstein condensate. *Phys. Rev. A*, **68**:065601, 2003.

[66] Z. Idziaszek, M. Gajda, P. Navez, M. Wilkens, and K. Rzążewski. Fluctuations of the weakly interacting bose-einstein condensate. *Phys. Rev. Lett.*, **82**:4376, 1999.

[67] T. P. Meyrath, F. Schreck, J. L. Hanssen, C.-S. Chuu, and M. G. Raizen. Bose-einstein condensate in a box. *Phys. Rev. A*, **71**:041604(R), 2005.

[68] Z. Hu and H. J. Kimble. Observation of a single atom in a magneto-optical trap. *Opt. Lett.*, **19**:1888, 1994.

[69] S. Kuhr, W. Alt, D. Schrader, M. Müller, V. Gomer, and D. Meschede. Deterministic delivery of a single atom. *Science*, **293**:278, 2001.

[70] R. V. Hogg and E. A. Tanis. *Probability and Statistical Inference*. Prentice Hall, New Jersey, 1997.

[71] C.-S. Chuu, F. Schreck, T. P. Meyrath, J. L. Hanssen, G. N. Price, and M. G. Raizen. Direct observation of sub-poissonian number statistics in a degenerate bose gas. *Phys. Rev. Lett.*, **95**:260403, 2005.

[72] C. W. Gardiner, P. Zoller, R. J. Ballagh, and M. J. Davis. Kinetics of bose-einstein condensation in a trap. *Phys. Rev. Lett.*, **79**:1793, 1997.

[73] C. W. Gardiner, M. D. Lee, R. J. Ballagh, M. J. Davis, and P. Zoller. Quantum kinetic theory of condensate growth: Comparison of experiment and theory. *Phys. Rev. Lett.*, **81**:5266, 1998.

[74] M. D. Lee and C. W. Gardiner. Quantum kinetic theory. vi. the growth of a bose-einstein condensate. *Phys. Rev. A*, **62**:033606, 2000.

[75] L. D. Carr, M. J. Holland, and B. A. Malomed. Macroscopic quantum tunneling of bose-einstein condensates in a finite potential well. *J. Phys. B*, **38**:3217, 2005.

[76] J. Javanainen and M. Yu. Ivanov. Splitting a trap containing a bose-einstein condensate: Atom number fluctuations. *Phys. Rev. A*, **60**:2351, 1999.